PERFORMANCE ANALYSIS OF RADIAL COMPRESSORS WITH THE OPEN-SOURCE COMPUTATIONAL FLUID DYNAMICS SUITE SU2

A Thesis

by

Mustafa Kürşat Uzuner

Submitted to the
Graduate School of Sciences and Engineering
In Partial Fulfillment of the Requirements for
the Degree of

Master of Sicence

in the
Department of Mechanical Engineering

Özyeğin University
June 2023

PERFORMANCE ANALYSIS OF RADIAL COMPRESSORS WITH THE OPEN-SOURCE COMPUTATIONAL FLUID DYNAMICS SUITE SU2

Approved by:

Assistant Professor Dr. Altuğ Melik Başol, Advisor
Department of Mechanical Engineering
Özyeğin University

Associate Professor Dr. Özgür Ertunç
Department of Mechanical Engineering
Özyeğin University

Associate Professor Dr. Güllü Kızıltaş Şendur
Mechatronics Program
Sabancı University

Date Approved: 25 May 2023

Çok sevgili anneme ...

To my very dear mother ...

ABSTRACT

Turbomachinery related computational fluid dynamics works are mostly done with commercial software such as ANSYS, Numeca, etc. In the open-source CFD field, there are not many software packages that prioritize or implement turbomachinery specific features in them. However, the open-source CFD software SU2 is an exception in that regard. It has turbomachinery specific features implemented in it out of the box. In this work, the capabilities of SU2 are investigated for turbomachinery CFD analysis and design, specifically on radial compressors.

First step, the fluid flow governing equations are derived. Turbulence modeling and the turbulence models used are briefly explained. The physical modelling and numerical implementation of SU2 are described. The methodology developed for the flow simulations and optimization process are explained.

Validation of SU2 is done by using two compressible turbulent flow cases. These cases are turbulent boundary layer and transonic airfoil RAE2822. Both cases see frequent usage in validation studies. These two are relevant for a turbomachinery case as well. For the turbulent boundary layer flow, it is very important for the solver to resolve the boundary layer very accurately. As for the transonic airfoil RAE2822, it is important to see if SU2 can accurately determine the shock location.

For the simulations, two radial compressor geometries are used with vaned and vaneless diffusers. Several operating points are used for both geometries. The results obtained with SU2 are comapred to Fidelity Flow results and experimental data provided by MAN Energy Solutions Schweiz AG and ANSYS-CFX. Results from SU2 showed promising results for both geometries. A comparison of available turbulence models in SU2 is also included.

SU2 has integrated optimization tools of its own. These out of the box optimization capabilities of SU2 are investigated for its applicability to turbomachinery cases. For this investigation, the vane of the vaned diffuser geometry is used. The diffuser geometry is simplified to a 2D geometry and optimization study is done with this geometry. Optimization study is conducted for only a single operating point, selected from the performance map of the radial compressor with the vaned diffuser. Optimized blade is compared to the baseline design and how much of an improvement made is explained.

In the end, the capabilities of SU2 regarding turbomachinery analysis and design are examined. It can be said that as an outcome of this work, even though SU2 has both advantages and disadvantages, it definitely shows good potential in turbomachinery analysis for an open-source CFD tool.

ÖZETÇE

Turbomakineler ile ilgili akış analiz çalışmaları için çoğunlukla kullanılan Hesaplamalı Akışkanlar Dinamiği (HAD) yazılımları ANSYS, Numeca, vb. gibi ücretli yazılımlardan oluşmaktadır. Açık kaynak HAD yazılımları arasında, turbomakine akış analizlerinde kullanılan ve turbomakine analizlerine özel ayarları bulunan bir yazılım bulmak oldukça zordur. Ancak, açık kaynak HAD yazılımları arasında bulunan SU2 diğer örneklerine kıyasla bir istisna halindedir. SU2 içerisinde turbomakine akış analizlerinde kullanılan özel ayarları hali hazırda barındırmaktadır. Bu çalışmada, açık kaynak HAD yazılımı olan SU2'nin turbomakine tasarımı ve akış analizinde kabiliyetleri, özellikle radyal kompresör çerçevesinde irdelenmiştir.

Çalışmanın ilk aşamasında, akış analizinde kullanılan denklemler tanıtılmış ve türetilmiştir. Akış analizlerinin bir parçası olan türbülansın modellenmesi ve kullanılan farklı türbülans modelleri kısaca açıklanmıştır. SU2 içerisinde bu denklemlerin fiziksel olarak nasıl modellendikleri ve numerik olarak nasıl uygulandıklarından bahsedilmiştir. Akış analizlerinde ve optimizasyon sürecinde kullanılan metodoloji açıklanmıştır.

SU2'nin validasyonu için iki sıkıştırılabilir türbülanslı akış rejiminde çalışan vaka kullanılmıştır. Bunlar benzer uygulamalarda da sıkça kullanılan türbülanslı düz plaka ve transonik kanat profili RAE2822'dir. Türbülanslı düz plaka vakasının önemi, SU2'nin sınır tabakayı doğru bir şekilde çözüp çözemeyeceğinin gözlemlenebilmesidir. Transonik kanat profili RAE2822 vakasının önemi de, SU2'nin kanat profili üzerinde oluşan şok konumunu doğru bir şekilde tahmin edip edemeyeceğinin gözlemlenebilmesidir.

Çalışmada yapılan turbomakine akış analizlerinde iki radyal kompresör geometrisi, difüzör bölümünde kanatçık bulunan ve bulunmayan, kullanılmıştır. Kullanılan iki geometri için de birçok çalışma noktası simüle edilmiştir. SU2 ile elde

edilen sonuçlar, MAN Energy Solutions Schweiz AG tarafından sağlanan, deneysel veriler ve Fidelity Flow yazılımından elde edilen sonuçlar ile karşılaştırılmıştır. Karşılaştırmaların sonucunda SU2'nin oldukça iyi doğrulukta sonuçlar elde ettiği gösterilmiştir. Bunlarında yanında, SU2 içerisinde bulunan iki farklı türbülans modelinin de birbiriyle karşılaştırılması yapılmıştır.

SU2 hali hazırda içerisinde optimizasyon araçlarıyla beraber gelmektedir. Bu araçların turbomakine vakalarında ne kadar kullanılabildiği test edilmiştir. Bunun için, difüzöründe kanatçık bulunan radyal kompresör geometrisi seçilmiştir ve difüzördeki kanatçık optimize edilmeye çalışılmıştır. Difüzördeki kanatçık, vakanın daha basitleştirilmesi için 2D olarak modellenmiştir. Optimizasyon çalışması sadece bir çalışma noktası için gerçekleştirilmiştir. Bu çalışma noktası daha önce elde edilmiş performans eğrisinden seçilmiştir. Sonunda, optimize edilmiş kanatçık ile başlangıç olarak alınan tasarım karşılaştırılmış ve elde edilen iyileştirme gösterilmiştir.

Sonuç olarak, SU2'nin turbomakine akış analizi ve tasarımında ne gibi kabiliyetlere sahip olduğu bu çalışmada irdelenmiştir. Bu çalışmanın sonucu olarak, SU2'nin hem iyi hem de kötü yanları olmasına rağmen, sahip olduğu potansiyel sayesinde turbomakine akış analizlerinde kullanılmak için uygun bir alternatif açık kaynak HAD yazılımı olduğu söylenebilmektedir.

ACKNOWLEDGEMENTS

There have been a lot of people that I met through this thesis or my study at Özyeğin University. I want to start by mentioning my advisor, Asst. Prof. Dr. Altuğ Melik Başol. Mr. Başol have been very supportive and helpful at every problem and hurdle I have experienced during my thesis, courses, projects, and even just very basic school related issues. I can safely say that I have made a great decision by accepting Mr. Başol's offer. My experience at Özyeğin University become worth remembering mostly thanks to him.

I have also met great people that were and are pursuing their Masters or PhD degrees, which I became close friends with. Ersin Yıldız, Berkay Halvaşi, Tolga Altınoluk, Abdülhakim Enes Öksüz and Gönenç Can Altun are the people that I have spent most of my free time at and off the university, and collected pleasant memories. I thank them for their friendship and wish them great prosperity at their endeavors.

I also want to thank to my project counsellors Bob Mischo, Sebastiano Mauri and Philipp Jenny. I have truly enjoyed working with them and little bit sad it came to and end. Wish you all a healthy and fruitful life. Even though we were not able to meet face to face, my coworker, the person that will progress this work further from the point I leave it, Lorenzo Kyza Fabris. I wish you great success and happiness throughout your studies as well.

Lastly, I want to thank my mother, who has been supporting me, no matter what, from my earliest recollection. Without her, none of my achievements would have happened or meant anything. Even though it is hard to express my gratitude for you with just words, endless thanks to you, mother.

I hope my work will help other fellow open-source CFD enthusiasts, and become steppingstone for others on reaching better and more useful outputs.

TABLE OF CONTENTS

LIST OF TABLES

LIST OF FIGURES

CHAPTER I

INTRODUCTION

Computational fluid dynamics (CFD) is a very common working discipline that incorporates both scientific and practical solutions to complex problems. From simulating flow around an aircraft to simulating blood flow in a certain part of the human body, CFD sees use in a very wide range. Turbomachinery is one of these complex areas where the use of CFD is very significant. Turbomachinery cases can be various sizes depending on their intended usage. For example, Francis turbine is one of the famous examples for hydraulic turbines which are used for generating electricity. We see dental turbines that are used by dentists, a very small turbine working with compressed air. These dental turbines can have a very wide RPM range, depending on their usage. There are also cases for various sizes of fans that are used for cooling electronics, computers, etc. Together with their sizes, the working conditions are also in a very wide range as well. This makes developing an all-purpose test rig for a type of turbomachinery very hard. CFD becomes a very important tool at this point. Using computers, it is possible to simulate any kind of turbomachinery in any condition with a lesser cost compared to experimenting. With its very promising potential, CFD can answer the questions or give ideas about the answer that would have been unfeasible otherwise. However, using computational tools also has their limitations as well. The most significant downside of CFD is its accuracy. Even though it is possible to simulate any condition with CFD, the accuracy of simulations become more challenging to sustain as the simulation conditions become more complex. Turbomachinery cases are very complex by default. Therefore, doing CFD of a turbomachine requires much more effort compared to a simple external flow case that operates inside the incompressible region. Turbomachinery cases are highly turbulent inflow cases

with various regimes being present in flow at the same time.

Considering the complexity of simulating a turbomachinery case using CFD, the sources that can supply this opportunity become very valuable. There are several commercial and open-source tools that are being used both in academy and industry. It is possible to do a fairly simple external flow case both with commercial and open-source tools. However, when it comes to turbomachinery, the options are limited. Most of the software that can solve a turbomachinery case accurately are commercial software, namely, ANSYS-CFX, NUMECA, StarCCM+, etc.

The most prominent open-source CFD tool nowadays is OpenFOAM. It is a very powerful and easily modifiable CFD tool that can solve most of the aerodynamic cases accurately. Because of its promising potential, OpenFOAM is selected for the preliminary trials for turbomachinery simulations. For that, turbulent and compressible validation cases such as flat plate and transonic airfoil RAE2822 are investigated. Baseline OpenFOAM and its derivative version foam-extend are used and compared to each other. The derivative version foam-extend performed slightly better compared to the baseline OpenFOAM. However, even though foam-extend contained some compressible flow specific solvers such as steadyCompressibleFoam, for the trial turbomachinery cases the results were not satisfactory. Even though OpenFOAM is very promising, in terms of turbomachinery, its capabilities become limited. It is not developed considering cases similar to turbomachinery and has no turbomachinery specific qualities. This means that to solve a turbomachinery case with CFD, a commercial tool is almost the only option.

That being said, there is another open-source tool that needs to be considered as well, and it is Stanford Unstructured[2] (SU2). SU2 is an open-source CFD software like OpenFOAM. It is developed by Stanford University. What makes SU2 a very promising open-source CFD software for someone working with turbomachinery is that it has turbomachinery specific qualities. This makes so that there is a legitimate open-source option beside commercial tools for turbomachinery CFD. However, SU2 also must prove that it can accurately solve compressible, turbulent,

and rotating flows for it to be considered an alternative tool for turbomachinery CFD.

SU2 is built to do high fidelity PDE analysis with using structured and unstructured meshes. The main module for doing flow simulations is called SU2_CFD. With this module it is possible to solve Euler, Navier-Stokes, RANS and Adjoint equation. SU2 is first released in January of 2012, and it is being developed mainly by Aerospace Design Lab (ADL) of the Department of Aeronautics and Astronautics at Stanford Universitys [2]. Since it is an open-source project, there are also many other developers and contributors in its community from different parts of the world, and it keeps acquiring more users while growing day by day.

Different variations of Reynolds Averaged Navier-Stokes (RANS) equations, namely, compressible, incompressible, Arbitrary Lagrangian-Eulerian (ALE), etc. are included in SU2. By default, laminar Navier-Stokes and Euler equations are also present in it as subsets of RANS equations. These are achieved by simply turning off turbulence modelling and fully removing viscosity [2]. It is possible to run Direct Numerical Simulation (DNS) with SU2 as well by only using Navier-Stokes equations and not selecting a turbulence model. However, since mostly the mean properties of the flow are in the interest, using RANS equations with a suitable turbulence model is very popular. Turbulence models included in SU2 are two of the most known models, Spalart-Allmaras and Shear Stress Transport turbulence models [2]. There are also several different versions of these two models but only the original ones are investigated in this project.

As it is established that SU2 is a more promising open-source flow simulation candidate for turbomachinery simulations among other open-source flow simulation packages, SU2 is selected to be used for the work that is conducted during this thesis. Version 7.0.6 of SU2 is used for the simulations in this work with some user implemented changes to the code. Centrifugal compressor cases with and without vaned diffusers are investigated to test and evaluate the capabilities of SU2 with regards to its turbomachinery specific abilities. Additionally, since SU2 also

has its own optimization package as well, optimization of vane of a centrifugal compressor is carried out. With this, the use of SU2 in a centrifugal compressor product development is tested starting with simulating for various operating points and optimizing the geometry to obtain a geometry that shows relatively better performance.

The work done for this thesis was in collaboration with MAN Energy Solutions Schweiz AG. Centrifugal compressor geometries and operating points together with Fidelity Flow results and the experimental data are provided by them.

CHAPTER II

PREVIOUS WORKS

SU2 is an open-source CFD software that has people developing it all around the world. In terms of turbomachinery related feature developments, Delft University of Technology (TU Delft) stands out. There are researchers who work on SU2 mostly related to turbomachinery analysis, optimization, and design. Thanks to that, there are several master theses about turbomachinery and SU2 from TU Delft.

A very similar master thesis on assessment of SU2 for radial compressor performance evaluation is conducted [3]. It is the first validation and verification work conducted on radial compressors using SU2. In this example, a turbocharger and Supercritical CO2 compressor analysis are done with SU2, and SU2 is compared against ANSYS-CFX and experimental data. A comparison of Spalart-Allmaras (SA) and Shear Stress Transport (SST) turbulence models is also done in SU2. The downsides of SU2 are also mentioned in this study. The dependence on mesh quality is found out to be very significant for the stability of the simulations. Moreover, the lack of wall functions made the dependence on the mesh more critical for SU2. Compared to CFX, SU2 showed adequate performance. However, as it can be predicted, CFX outperformed SU2 in run time and accuracy. The difference between this example and the current work is that the investigation of the presence of a vane in the diffuser. Also, no optimization study on the compressors used is conducted in this example.

There are several other master theses that investigate axial turbomachinery for the implementation of mixing-plane interface and turbomachinery optimization. For a multi-stage axial turbine, the implementation and tests of mixing-plane interface with the non-reflective boundary conditions using 3D cases are done in

SU2 for unstructured grids [4]. The implementation is compared to experimental data and a well-known flow solver, which it resulted in an adequate agreement. However, this implementation is not verified for radial or mixed flow turbines and compressors in this example. The comparison of Harmonic Balance and steady analysis methods are conducted for different axial turbomachinery stages with different working fluids together with an optimization study, all in 2D [5]. The difference for these solvers depended on some parameters. The difference between these solvers decreased when reduced frequency is lowered and increased when Mach effects started to become more prominent. The development of an open-source framework for optimizing axial and radial turbines is performed with SU2 and ParaBlade combined [6]. The sensitivities calculated by adjoint method used in optimization study are compared to finite difference methods. It showed great improvement in computational cost. Moreover, incorporating a CAD based parametrization into the optimization process enabled better handling for the geometric constraints. It is also mentioned that end wall effects may influence the adjoint sensitivities in this example. Body-force modeling (BFM) for full-annulus simulations of an axial turbine for the development of boundary layer ingestion (BLI) engine using SU2 is conducted together with the implementation of this BFM method into SU2 [7]. This BFM method cost very little compared to physical modelling. However, this came with its downsides as well. Even though the trends obtained in the end were similar, the accuracy of BFM method was not at the same level with the physical modelling. A 3D turbomachinery blade modeler is developed to close the gap between mean-line analysis and 3D CFD, and coupled with SU2 for the analysis [8]. This example showed that SU2 can be implemented in a detailed shape optimization process.

There are also other theses outside of TU Delft that investigate optimization and analysis with compressible flows using SU2. For the simulation of aircraft's exhaust flow, turbulent round jet simulations are done using SU2 [9]. Considering the complexity of flow conditions for the turbulent round jet simulations, SU2

showed adequately accurate results compared to experimental data and it agreed well with the results obtained by NASA. A 2D adjoint optimization to increase the thrust of a supersonic converging diverging nozzle is done using SU2 [10]. The optimization study is conducted by using two different objective functions, Mach number and mass flow rate. It is stated that using Mach number as the objective function to increase the exit velocity would decrease the throat area, which decreases the mass flow rate and works against the target objective of increasing the thrust. Using mass flow rate for the objective function increases the throat area unlike the behavior when Mach number was used as the objective function. Even though increasing the throat area lowers the exit Mach number, it achieves a higher thrust as it was the target objective. Using both of these objective functions together resulted even higher thrust increase compared to only using mass flow rate as the objective function but the exit pressure decreased significantly. The best optimization case is obtained by using Mach number and mass flow rate as the objective functions together and assigning total pressure as the constraint function to keep exit pressure from decreasing.

There are other theses that use subsonic cases for optimization and analysis with SU2. Adjoint optimization and analysis of a subsonic submerged intake is done with SU2 [11]. Other open-source software like Salome, GMSH and ParaView are utilized as well. SU2 is validated against experimental data first using two intake models. The included optimization tools in SU2 are used for the optimization study. Single point and multi point optimizations are performed on different intake models. While improving the pressure recovery of these intakes it is stated that the use of submerged intakes as lift producing elements is quite efficient. Aerodynamic shape optimization of a 3D wing of a turboprop trainer that uses SU2 to obtain flow solution is performed [12]. For the optimization method an external tool is used which used response surface methodology. SU2 is utilized in determining the lift coefficient values at different Mach numbers and angles of attack. The objective and constraint functions for the optimization study are

selected for the aircrafts mission profile.

SU2 can be found to be used in various other applications as well. One of those examples is one where SU2 is used for studying the ice accretion on wind turbine blades under different icing conditions [13]. To determine ice accretion the blade element momentum method is incorporated together with an extended Messinger model. Validation is done by using experimental and numerical data found in the literature. Three flow solvers with different fidelities are used and compared together. These flow solver are; X-Foil coupled with a boundary layer model, SU2 and an in-house DDES solver. SU2 also can be found in an aero-structural optimization of a wing with Individual Discipline Feasible (IDF) architecture [14]. IDF is used for decoupling aerodynamic and structural disciplines. For the aerodynamic part SU2 is used and for the structural part FEMWET is used. SU2 is also changed to take structural deformation information as inputs, and then it would compute sensitivities for the objective function for that deformation. On an Airbus A320 type aircraft, by increasing wing span, decreasing wing sweep, and improving lift distribution together with airfoil shape, a significant reduction in fuel weight is achieved. SU2 is also used in fluid structure interaction (FSI) problems as well [15]. In this example SU2 is extended for FSI problems. On top of its current solvers, a finite element solver, which can work on geometric and material non-linearities in static and dynamic settings is developed. This structural solver is then coupled with the fluid flow solver of SU2 with a partitioned approach. The validation of this implementation is done by a test case of rigid square with a flexible cantilever. Simulations are conducted under small Reynolds numbers. The results showed good agreement when compared to literature. SU2 can also be found in a overset grid problem [16]. The *Overset Parallel Engine for AeRodynamic Applications* (OPERA), developed by the Institute of High Performance Computing, Singapoer, is coupled with SU2. The simulations are done on a three-dimensional sphere. The results showed good accuracy and great potential for further development.

Other examples that include different rotating machinery can also be found. Su2 is used for predicting the performance of rotorcraft main rotor blades in hover and forward flight conditions [17]. Both steady and time accurate models are examined for hover simulations. For forward flight simulations, the code was changed to include main rotor blade kinematics. Different test cases are simulated for hover and forward flight. For hover, Caradonna-Tung test case was used, and for the forward flight AH-1G helicopter was used. Pressure distributions and aeroacustics' data are compared to measurements from the test cases. Good agreement between SU2 and measurements is found. In another example SU2 is used to determine the compressibility effect on dynamic stall using rotorcraft main rotor blades [18]. Dynamic stall is more prominent at the boundaries of the flight envelope in high-speed forward flights or rapid maneuvers for a typical rotorcraft. The rotor airfoil VR-12 is used for the simulations at static and dynamic stall conditions. The simulation results are compared to experimental data. At relatively small Mach numbers such as 0.2, the driving phenomena for both static and dynamic stalls is the flow separation due to adverse pressure gradient. At low Mach numbers the compressibility effect is negligible. However, at Mach number 0.4, due to the formation of local supersonic pocket at the leading edge, the flow separation is driven by the shock. At the Mach number 0.3, both phenomena of adverse pressure gradient and shock effect are apparent. Overall, good agreement between SU2 results and the experimental data is found.

SU2 finds use in Organic Rankine Cycle (ORC) applications as well. SU2 is investigated in the case of analysis of ORC turbines [19]. The ability to solve Non-Ideal Compressible Fluid Dynamics (NICFD) is implemented by including thermodynamic libraries to cover the non-ideal thermodynamic behavior of non-ideal fluid flows. The results are compared to reference NICFD test cases and ANSYS-CFX. Results showed that SU2 is capable of solving NICFD fluid flows. SU2 is also used for experimental investigation of NICFD flow that specifically

cover ORC applications [20]. The performance of SU2 in handling complex thermodynamic models of organic fluids is tested and compared to experiments. A converging diverging nozzle, which exemplify ORC supersonic stators, a diamond shaped airfoil at zero angle of attack, and a backward step, which exemplify trailing edge of turbine blades, are used for the comparison between SU2 and experimental data. The non-ideal conditions in these experiments and simulations had similar compressibility factors, $Z = P\nu/(RT)$, calculated using corresponding equations of state for the MDM fluid, ranging between $Z = 0.8$ and $Z = 0.9$. The results obtained by SU2 agreed well with the experimental results, showing the validity of the thermodynamic models and flow solver implementations. Another example that investigated the dynamic response of line-cavity systems under ideal and non-ideal compressible flow conditions for ORC power systems is done with SU2 [21]. These systems are investigated to understand the behavior of fast-response pressure probes that are used in turbomachinery applications for gas and ORC power systems. The results give a guideline for the design of these fast-response pressure gages. Another example that uses SU2 investigates the fish tail shocks appearing at the trailing edge of high-pressure turbine vanes, which are be found in ORC turbines [22]. ORC power systems are likely to experience this kind of shock pattern particularly at the first stage turbine stator blades due to high outlet Mach numbers. Since the fluids in these ORC power systems are molecularly complex, non-ideal effects on the shock pattern needs to be considered. These non-ideal effects show its impact on thermodynamic conditions. The shock pattern is compared between an ideal and non-ideal case. The non-ideal effects are obtained by using MDM as the working fluid.

There are several articles that use SU2 for turbomachinery fluid flow analysis

and optimization as well. An unsteady multi-stage axial turbomachinery optimization with harmonic balance method is done using SU2 [23]. Harmonic balance method is a productive method for CFD applications characterized by quasi-periodic flows. It is much faster compared to direct unsteady simulations. Combining harmonic balance with adjoint optimization costs computationally much lower to unsteady adjoint optimization. The results showed good agreement in the gradients calculated with harmonic balance adjoint and second order finite differences. Another example can be found that uses SU2 for multistage axial and radial turbomachinery analysis and design optimization with discrete adjoint method [24]. The mixing-plane interface is implemented in this example. Solutions are validated using experimental results. The machinery used in this example are; one and a half axial turbine stage, a transonic radial turbine with a downstream diffuser, and a supersonic mini ORC radial turbine. Adjoint optimization is done on one and a half stage axial turbine, optimizing all three blade rows in the same time. Another example that investigates Free-Form Deformation (FFD) and CAD-based shape parametrization methods in turbomachinery optimization using adjoint approach in SU2 [25]. The way that the optimization target surface, which is usually the blade in a turbomachinery case, is parametrized affects the robustness of the optimization process. FFD based parametrization brings great design flexibility while being very tedious when ensuring geometrical constraints. CAD-based parametrization brings great control over the blade geometric shape while it is limited to a narrower design space compared to FFD method. This study used the same 2D turbine cascade case to optimize using different parametrization methods and compared the results with each other. The results showed similar optimum performances. However, the blade shapes reached for different parametrization methods was different from each other, This means that the optimization problem has multiple optima points, and the selected parametrization tool can affect the optimum shape.

It is possible to find an example work done with SU2 related to any fluid

dynamics related area. Some of these are briefly explained here. Since the main topic of this thesis is about turbomachinery, the turbomachinery related works done with SU2 are examined more. Most of these works investigated both axial and radial turbine analysis and optimization for various working fluids. Investigation of radial compressors are rare compared to turbines. This work hopefully will fill this gap for radial compressors with the analysis of vaned and vaneless diffuser configurations together with a simplified 2D adjoint optimization of a vane blade profile.

CHAPTER III

GOVERNING EQUATIONS FOR COMPRESSIBLE FLOWS

In fluid dynamics there can be very different working conditions. For example, the problem may include an external flow case with very high speeds which interacts with shock waves, or it can be a problem where the speed of the flow is relatively smaller but the flow may have to go through narrow passages. Even though one can keep counting different flow condition scenarios, they will all be governed by the same physics. Considering the regime of the flow or involvement of other phenomena, it is possible to see additional physics included, but the base will still be the same. This also true for turbomachinery cases as well. If a compressor case is to be used as an turbomachinery example, flow has to go through a rotating machinery inside a passage and change its path continuously while passing different stages of the compressor. Additionally, in the meantime, flow also gets compressed. However, the same base conservation laws will still be relevant.

In turbomachinery fluid dynamics the main interest is compressible, viscous flows. Viscous flow is a flow in which the impacts of viscosity, thermal conduction, and mass diffusion are important [26]. However, since the interest here is on the fluid dynamics, when there is no gas with gradients in its chemical species, mass diffusion can be neglected. With this, a viscious flow becomes where only viscosity and thermal conduction are in the interest.

Viscosity has a retarding effect on the relative motion of the flow over a surface [26]. Due to friction between the fluid near the surface and the surface, the surface will experience a tugging force in the flow direction tangential to the surface. This tugging force per area is called as the shear stress,τ. Also, in the opposite direction, an equal force will act on the fluid near the surface and lower the velocity of the

flow. Due to the influence of friction, flow velocity right at the surface will be zero, which is called the no-slip condition.

In addition to causing shear stress, friction also determines how the flow will behave over a body [26]. When flow encounters a surface, it will start to feel the effect of friction, which will increase as the flow moves along the body. Because of the previously explained no-slip condition, flow near the surface will have less and less velocity in the surface normal direction as the flow moves along the surface. This lesser velocity region that keeps growing as the flow moves along the body is also called the boundary layer. While the velocity decreases at these locations, pressure will increase creating a pressure gradient. Due to this pressure gradient, after some point, the flow near the surface will reverse its direction. When this reverse flow occurs, the flow will separate from the surface and create a wake region downstream of the surface. Flow separation causes the pressure distribution on the surface to considerably change. The flow will see the actual surface up to the separation point but after that point, which is downstream of the separation, flow will see an effective body because of this separated region.

The net effect of friction is an integrated force in the flow direction, which is also called drag [26]. Viscosity causes two types of drag, which are skin friction drag, D_f, and pressure drag, D_p. Skin friction drag is the integral of the shear stress component in the drag direction. Pressure drag is the integral of the pressure distribution on the body in the drag direction.

Other than friction, viscosity also affects the thermal conduction [26]. Because of the friction it was explained that the velocity of the flow over the surface decreases, meaning that the kinetic energy of the flow decreases. This lost energy is turned into internal energy and causes the temperature to increase. This is called viscous dissipation in the fluid. The change in the temperature due to viscosity will also heat transfer since temperature difference becomes apparent. The name of this mechanism is called aerodynamic heating, and with the increased velocity it increases as well.

Viscosity and thermal conduction in a fluid are because of the transport of momentum and energy with random molecular motions [26]. In a fluid, every molecules have momentum and energy that they carry. Viscosity and thermal conduction are macroscopic effects. The transport of molecular momentum causes the viscosity, and the transport of molecular energy causes the thermal conduction, which are called transport phenomena.

Shear stress exerted on a surface is proportional to the velocity gradient in the surface normal direction, and the constant of this proportionality is called viscosity coefficient,μ[26]. Similarly, the time rate of heat conducted per unit area on a surface is proportional to the temperature gradient in the surface normal direction, and the constant of this proportionality is called thermal conductivity,k. μ and k are physical properties of the fluid, and functions of temperature for most of the cases.

For turbulent flows, transport of momentum and energy can also happen with random motion of large turbulent eddies as well [26]. Turbulent transport creates effective values of viscosity and thermal conductivity called as eddy viscosity, ϵ, and eddy thermal conductivity, κ. These turbulent transport coefficients ϵ and κ overwhelmingly depend on flow field characteristics like velocity gradients. These are not just molecular properties of the fluid as was the case with μ and k.

3.1 Fluid Flow and Heat Transfer Governing Equations

Mathematical statements of the conservation laws of physics are reflected on to the governing equations of the fluid flow. These mathematical statements are as given below [1].

- Fluid mass is conserved.
- The total of the forces on a fluid particle is equal to the rate of change of momentum. This is also Newton's second law.
- The total of the rate of heat incluison to and the rate of work done on a

fluid particle is equivalent to the rate of change of energy. This is also first law of thermodynamics.

The behavior of the fluid is defined considering the macroscopic properties such as velocity, pressure, temperature, density, and their time and space derivatives [1]. The molecular structure of matter and molecular motions are disregarded. The macroscopic properties can be assumed as averages over appropriately large numbers of molecules. Therefore, a fluid particle can be explained as the smallest fluid element where its macroscopic properties are not changed by individual molecules.

The fluid element that will be used for the conservation laws is shown below.

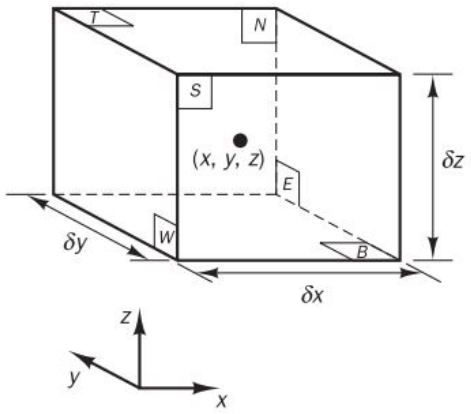

Figure 1: Fluid Element Schematic [1]

Center of the fluid element shown in Figure 1 is indicated with *(x,y,z)*. This fluid element is infinitesimally small with sides δx, δy and δz. Fluid flow equations are derived by considering the changes in mass, momentum, and energy of the fluid element because of the fluid flow through its boundaries and action of sources inside the element.

Pressure, temperature, density and velocity vector are functions of space and time [1]. For ease of use, this dependence on space and time will not be explicitly shown in notations. Since the fluid element in the interest is infinitesimally small, it is possible to accurately express the fluid properties at the faces with the first

two terms of a Taylor series expansion. With this, it is possible to write pressures at the faces W and E as shown below [1].

$$P_W = P - \frac{\partial P}{\partial x}\frac{1}{2}\delta x \tag{1}$$

$$P_E = P + \frac{\partial P}{\partial x}\frac{1}{2}\delta x \tag{2}$$

3.1.1 Mass Conservation

Mass conservation equation is derived by using the mass balance for the fluid element. Mass balance can be expressed in words as, net rate of flow of mass into the fluid is equal to the rate of increase of mass in fluid element [1]. Rate of increase of mass in fluid element is as shown below.

$$\frac{\partial}{\partial t}(\rho\delta x\delta y\delta z) = \frac{\partial \rho}{\partial t}\delta x\delta y\delta z \tag{3}$$

Right hand side of the Equation 3 is obtained by using the mass flow rate through the faces of the fluid element. In order to calculate mass flow rate; density, area and normal component of the velocity at the interested face are needed. Mass flow rates at each face of the fluid element are shown in Figure 2.

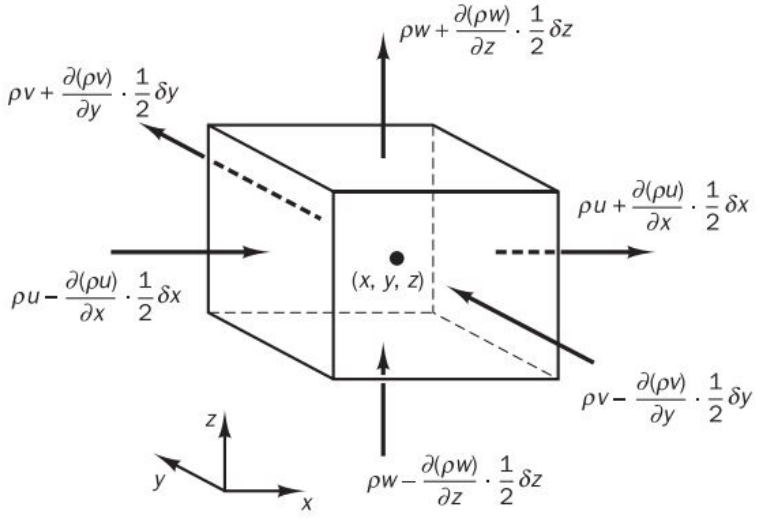

Figure 2: Mass Flow Rates Through Faces of a Fluid Element[1]

All of the mass flow rates shown in Figure 2 are put together by taking the mass flow rates into the fluid element as positive and mass flow rates out of the

fluid as negative. This corresponds to the net rate of flow of mass into the fluid element and is shown in Equation 4.

$$\begin{aligned}
&\left(\rho u - \frac{\partial(\rho u)}{\partial x}\frac{1}{2}\delta x\right)\delta y\delta z - \left(\rho u + \frac{\partial(\rho u)}{\partial x}\frac{1}{2}\delta x\right)\delta y\delta z \\
&+ \left(\rho v - \frac{\partial(\rho v)}{\partial y}\frac{1}{2}\delta y\right)\delta x\delta z - \left(\rho v + \frac{\partial(\rho v)}{\partial y}\frac{1}{2}\delta y\right)\delta x\delta z \\
&+ \left(\rho w - \frac{\partial(\rho w)}{\partial z}\frac{1}{2}\delta z\right)\delta x\delta y - \left(\rho w + \frac{\partial(\rho w)}{\partial z}\frac{1}{2}\delta z\right)\delta x\delta y
\end{aligned} \tag{4}$$

When Equation 3 and Equation 4 are put together and divided by the volume of the fluid element Equation 5 is acquired.

$$\begin{aligned}
&\frac{\partial\rho}{\partial t} + \frac{\partial(\rho u)}{\partial x} + \frac{\partial(\rho v)}{\partial y} + \frac{\partial(\rho w)}{\partial z} = 0 \\
&\frac{\partial\rho}{\partial t} + div(\rho\mathbf{V}) = 0
\end{aligned} \tag{5}$$

Equation 5 is the the mass conservation equation for an unsteady, compressible fluid flow [1]. If the interested condition is steady, the term related with time from Equation 5 is simply dropped. The resultant equation is Equation 6.

$$\frac{\partial(\rho u)}{\partial x} + \frac{\partial(\rho v)}{\partial y} + \frac{\partial(\rho w)}{\partial z} = 0 \tag{6}$$

3.1.2 The Connection Between Rates of Change for a Fluid Element and a Fluid Particle

While deriving momentum and energy conservation equations the conservation laws mentioned earlier are taken as the base of the derivation. The laws these equations are based on make statements about changes in the properties of a fluid particle [1]. This is called Lagrangian approach. Properties of this fluid particle are a function of the position and time. Assume that the value of a property is represented with ϕ, and the total derivative of this property with respect to time following a fluid particle is given in Equation 7.

$$\begin{aligned}
&\frac{D\phi}{Dt} = \frac{\partial\phi}{\partial t} + u\frac{\partial\phi}{\partial x} + v\frac{\partial\phi}{\partial y} + w\frac{\partial\phi}{\partial z} \\
&\frac{D\phi}{Dt} = \frac{\partial\phi}{\partial t} + \mathbf{V}\cdot grad(\phi)
\end{aligned} \tag{7}$$

The total derivative represents rate of change of property ϕ per unit mass [1]. Since we are interested in defining these equations using a fluid element, a relation between the total derivative, which follows the fluid particle, and equations derived for the fluid element has to be established. The equations related to the fluid element are for rates of change per unit volume. Using total derivative and density, the rate of change of ϕ per unit volume can be calculated as shown in Equation 8 [1].

$$\rho\frac{D\phi}{Dt} = \rho\left(\frac{\partial\phi}{\partial t} + \mathbf{V}\cdot grad(\phi)\right) \tag{8}$$

The mass conservation equation has the mass per unit volume, which is density, for the conserved quantity. The total of the rate of change of density in time and the convective term in the mass conservation equation for the fluid element is as shown in Equation 5. If this total is to be generalized for and conserved property ϕ, the Equation 9 will be reached [1].

$$\frac{\partial(\rho\phi)}{\partial t} + div(\rho\phi\mathbf{V}) \tag{9}$$

The relationship between the summation given in Equation 9 and the total derivative of ϕ is given in Equation 10 [1].

$$\begin{aligned}\frac{\partial(\rho\phi)}{\partial t} + div(\rho\phi\mathbf{V}) &= \rho\left[\frac{\partial\phi}{\partial t} + \mathbf{V}\cdot grad(\phi)\right] + \phi\left[\frac{\partial\rho}{\partial t} + div(\rho\mathbf{V})\right] \\ &= \rho\frac{D\phi}{Dt}\end{aligned} \tag{10}$$

With these relations established, the statement Equation 10 makes for any conserved fluid property is as follows; the sum of rate of increase of ϕ of a fluid element and net rate of flow of ϕ out of a fluid element are equal to the rate of increase of ϕ for a fluid particle [1].

3.1.3 Momentum Conservation

Momentum conservation is derived from Newton's second law as given below.

$$\mathbf{F} = m\mathbf{a} = \frac{\partial}{\partial t}(m\mathbf{V}) \tag{11}$$

The equation 11 states that the force is equal to the time rate of change of momentum. The forces acting on a fluid particle are divided into two categories; surface and body forces. Surface forces consist of pressure and viscous forces. Body forces consist of centrifugal, Coriolis, gravity, and electromagnetic forces. Usually surface force contributions to the momentum equation are added as separate terms while body force contributions are put into the momentum equation as a source term.

The shear stresses acting on a fluid element are shown in Figure 3.

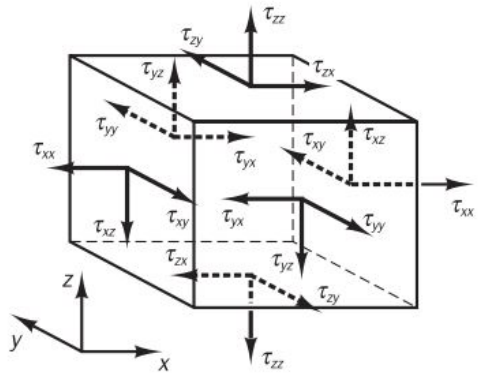

Figure 3: Shear Stresses Acting a Fluid Element [1]

The stresses shown in Figure 3 are viscous stresses, τ. The suffix given with τ are to give information about direction of the stress. First suffix indicates the surface normal, and second suffix indicates the direction that the stress component acts. There are also surface normal stresses, which is pressure.

To illustrate, the stresses in the x-direction on the fluid element are shown in Figure 4. If the forces on the faces E and W, as indicated in Figure 1, calculated from the stresses shown in Figure 4 are summed, Equation 12 will be the result.

$$\begin{aligned}
&\left[P - \frac{\partial P}{\partial x}\frac{1}{2}\delta x - \left(\tau_{xx} - \frac{\partial \tau_{xx}}{\partial x}\frac{1}{2}\delta x\right)\right]\delta y\delta z \\
&+ \left[-\left(P - \frac{\partial P}{\partial x}\frac{1}{2}\delta x\right) + \left(\tau_{xx} + \frac{\partial \tau_{xx}}{\partial x}\frac{1}{2}\delta x\right)\right]\delta y\delta z \\
&= \left(-\frac{\partial P}{\partial x} + \frac{\tau_{xx}}{\partial x}\right)\delta x\delta y\delta z
\end{aligned} \tag{12}$$

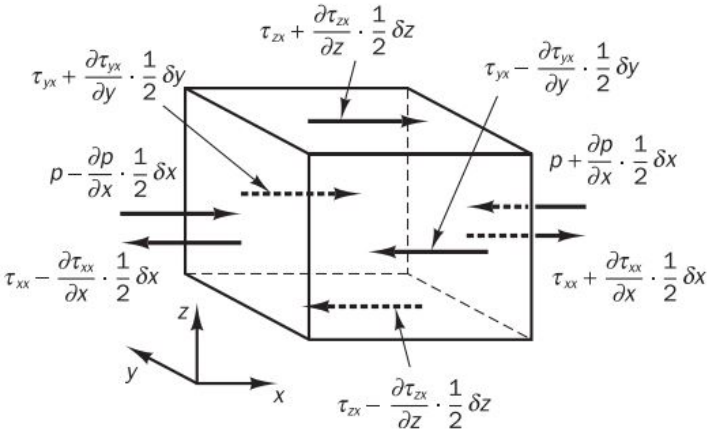

Figure 4: Stresses Acting a Fluid Element in x-Direction [1]

In a similar fashion, the summation of the forces on the faces N and S and the summation of the forces on the faces T and B will result in Equation 13 and Equation 14, respectively.

$$\frac{\tau_{yx}}{\partial y} \delta x \delta y \delta z \tag{13}$$

$$\frac{\tau_{zx}}{\partial z} \delta x \delta y \delta z \tag{14}$$

The total of Equations 12, 13 and 14 give the force acting on the fluid element in the x-direction as shown in Equation 15.

$$\left(-\frac{\partial P}{\partial x} + \frac{\tau_{xx}}{\partial x} + \frac{\tau_{yx}}{\partial y} + \frac{\tau_{zx}}{\partial z} \right) \delta x \delta y \delta z \tag{15}$$

If Equation 15 is to be divided with the volume of the fluid element, we obtain the force per unit volume acting on the fluid element in x-direction as given in Equation 16.

$$\left(-\frac{\partial P}{\partial x} + \frac{\tau_{xx}}{\partial x} + \frac{\tau_{yx}}{\partial y} + \frac{\tau_{zx}}{\partial z} \right) \tag{16}$$

The effect of body forces are included by adding a source term, S_{M_x}, which is x-momentum per unit volume per unit time due to body forces [1].

By incorporating Newton's second law, the component in the x-direction of the momentum equation can be derived. In other words, the rate of change of

x-momentum of the fluid particle is equal to the total force acting on the fluid element in the x-direction, which is shown in Equation 17 [1].

$$\rho\frac{Du}{Dt} = \frac{\partial(-P+\tau_{xx})}{\partial x} + \frac{\partial\tau_{yx}}{\partial y} + \frac{\partial\tau_{zx}}{\partial z} + S_{M_x} \tag{17}$$

Using the same manner while deriving Equation 17, the momentum equation components in y-direction and z-direction can be derived to be Equation 18 and Equation 19, respectively.

$$\rho\frac{Dv}{Dt} = \frac{\partial\tau_{xy}}{\partial x} + \frac{\partial(-P+\tau_{yy})}{\partial y} + \frac{\partial\tau_{zy}}{\partial z} + S_{M_y} \tag{18}$$

$$\rho\frac{Dw}{Dt} = \frac{\partial\tau_{xz}}{\partial x} + \frac{\partial\tau_{yz}}{\partial y} + \frac{\partial(-P+\tau_{zz})}{\partial z} + S_{M_z} \tag{19}$$

3.1.4 Energy Conservation

Energy conservation equation is defined using the 1^{st} law of thermodynamics, which states that the total of net rate of heat added to the fluid particle and net rate of work done on the fluid particle is equal to rate of increase of energy of the fluid particle [1].

3.1.4.1 Net Rate of Work Done on the Fluid Particle

Surface forces on the fluid element does work on the fluid particle. These works done can be calculated by taking the product of the force and velocity component in the direction of the force. When the forces calculated form the stresses shown in Figure 3 are used to calculate the work done on the fluid particle in the x-direction, Equation 20 can be found.

$$\begin{aligned}
&\left[\left(Pu - \frac{\partial(Pu)}{\partial x}\frac{1}{2}\delta x\right) - \left(\tau_{xx}u - \frac{\partial(\tau_{xx}u)}{\partial x}\frac{1}{2}\delta x\right)\right]\delta y\delta z \\
&- \left[\left(Pu + \frac{\partial(Pu)}{\partial x}\frac{1}{2}\delta x\right) + \left(\tau_{xx}u + \frac{\partial(\tau_{xx}u)}{\partial x}\frac{1}{2}\delta x\right)\right]\delta y\delta z \\
&+ \left[-\left(\tau_{yx}u - \frac{\partial(\tau_{yx}u)}{\partial y}\frac{1}{2}\delta y\right) + \left(\tau_{yx}u + \frac{\partial(\tau_{yx}u)}{\partial y}\frac{1}{2}\delta y\right)\right]\delta x\delta z \\
&+ \left[-\left(\tau_{zx}u - \frac{\partial(\tau_{zx}u)}{\partial z}\frac{1}{2}\delta z\right) + \left(\tau_{zx}u + \frac{\partial(\tau_{zx}u)}{\partial z}\frac{1}{2}\delta z\right)\right]\delta x\delta y \\
&= \left[\frac{\partial(u(-P+\tau_{xx}))}{\partial x} + \frac{\partial(u\tau_{yx})}{\partial y} + \frac{\partial(u\tau_{zx})}{\partial z}\right]\delta x\delta y\delta z
\end{aligned} \tag{20}$$

Works done by the forces acting on the fluid particle in the y and z directions are calculated in the same manner as Equation 20, and are as given in Equation 21 and Equation 22, respectively.

$$\left[\frac{\partial(v(\tau_{xy}))}{\partial x} + \frac{\partial(v(-P+\tau_{yy}))}{\partial y} + \frac{\partial(v\tau_{zy})}{\partial z}\right]\delta x\delta y\delta z \tag{21}$$

$$\left[\frac{\partial(w(\tau_{xz}))}{\partial x} + \frac{\partial(w\tau_{yz})}{\partial y} + \frac{\partial(w(-P+\tau_{zz}))}{\partial z}\right]\delta x\delta y\delta z \tag{22}$$

The summation of the works given in Equations 20, 21 and 22 divided with the volume of the fluid element give the net rate of work done on the fluid particle by the surface forces, which is given in Equation 23.

$$\begin{aligned} &- div(P\mathbf{V}) + \left[\frac{\partial(u\tau_{xx})}{\partial x} + \frac{\partial(u\tau_{yx})}{\partial y} + \frac{\partial(u\tau_{zx})}{\partial z}\right] \\ &+ \left[\frac{\partial(v\tau_{xy})}{\partial x} + \frac{\partial(v\tau_{yy})}{\partial y} + \frac{\partial(v\tau_{zy})}{\partial z}\right] \\ &+ \left[\frac{\partial(w\tau_{xz})}{\partial x} + \frac{\partial(w\tau_{yz})}{\partial y} + \frac{\partial(w\tau_{zz})}{\partial z}\right] \end{aligned} \tag{23}$$

3.1.4.2 Net Rate of Heat Added to the Fluid Particle

As shown in Figure 5, heat flux is a vector. In x, y and z directions, the net rate

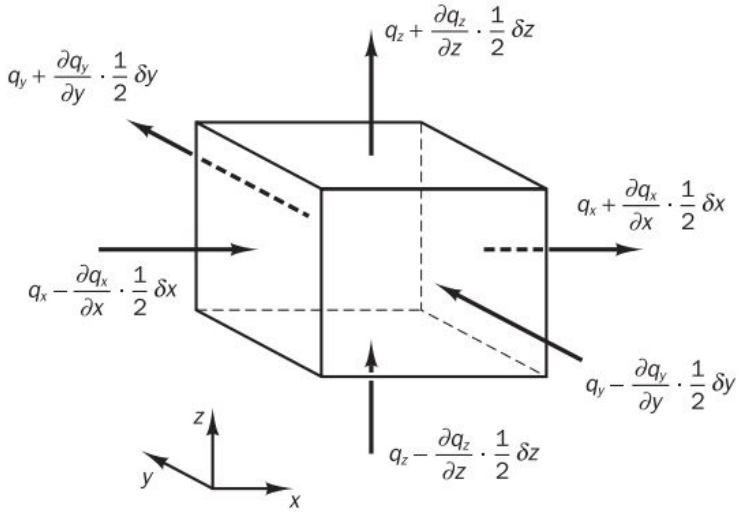

Figure 5: Heat Flux Through a Fluid Element [1]

of heat transfer to the fluid particle have to be written. In the x-direction, it is obtained by taking the difference between the heat input through the face W and

the rate of heat loss through surface the face E, which is given in Equation 24 [1].

$$\left[\left(q_x - \frac{\partial q_x}{\partial x}\frac{1}{2}\delta x\right) - \left(q_x + \frac{\partial q_x}{\partial x}\frac{1}{2}\delta x\right)\right]\delta y\delta z = -\frac{\partial q_x}{\partial x}\delta x\delta y\delta z \tag{24}$$

In the same manner, the net rate of heat transfer to the fluid particle in y and z directions are given in Equations 25 and 26, respectively.

$$-\frac{\partial q_y}{\partial y}\delta x\delta y\delta z \tag{25}$$

$$-\frac{\partial q_z}{\partial z}\delta x\delta y\delta z \tag{26}$$

Sum of the Equations 24, 25 and 26 divided with the volume of the fluid element gives the net rate of heat transfer to the fluid particle and is shown in Equation 27.

$$-\frac{\partial q_x}{\partial x} - \frac{\partial q_y}{\partial y} - \frac{\partial q_z}{\partial z} = -div(\mathbf{q}) \tag{27}$$

By using Fourier's law of heat conduction, a relation between the heat flux and local temperature gradient can be written [1].

$$q_x = -k\frac{\partial T}{\partial x} \quad q_y = -k\frac{\partial T}{\partial y} \quad q_z = -k\frac{\partial T}{\partial z}$$

$$\mathbf{q} = -k\, grad(T) \tag{28}$$

Combining this relation with Equation 27 will give Equation 29.

$$-div(\mathbf{q}) = div(k\, grad(T)) \tag{29}$$

3.1.4.3 Complete Energy Equation

The specific energy, E, for the fluid is the summation of internal (thermal) energy, i, kinetic energy, $\frac{1}{2}(u^2+v^2+w^2)$, and gravitational potential energy [1]. As it was the case for the momentum equation, gravitational potential energy changes are represented in a source term, S_E, per unit volume per unit time.

$$E = i + \frac{1}{2}(u^2+v^2+w^2) \tag{30}$$

Complete energy equation is obtained by equating the total of the net rate of work done on the fluid particle, the net rate of heat addition to the fluid particle,

and rate of increase of energy due to sources to the rate of change of energy of the fluid particle [1]. This is shown in Equation 31.

$$\begin{aligned}\rho\frac{DE}{Dt} =& - div(P\mathbf{V}) + \left[\frac{\partial(u\tau_{xx})}{\partial x} + \frac{\partial(u\tau_{yx})}{\partial y} + \frac{\partial(u\tau_{zx})}{\partial z}\right] \\ &+ \left[\frac{\partial(v\tau_{xy})}{\partial x} + \frac{\partial(v\tau_{yy})}{\partial y} + \frac{\partial(v\tau_{zy})}{\partial z}\right] \\ &+ \left[\frac{\partial(w\tau_{xz})}{\partial x} + \frac{\partial(w\tau_{yz})}{\partial y} + \frac{\partial(w\tau_{zz})}{\partial z}\right] \\ &+ div(k\, grad(T)) + S_E\end{aligned} \tag{31}$$

The mechanical energy related components from the Equation 31 are subtracted to have an equation only for the internal energy or temperature. The mechanical energy related part can be found out by multiplying each component of the momentum equation with its corresponding velocity component [1]. The summation of these multiplications will give the mechanical energy part of the Equation 31.

$$\begin{aligned}\rho\frac{D(u^2+v^2+w^2)}{Dt} =& - \mathbf{V} grad(P) + u\left(\frac{\partial\tau_{xx}}{\partial x} + \frac{\partial\tau_{yx}}{\partial y} + \frac{\partial\tau_{zx}}{\partial z}\right) \\ &+ v\left(\frac{\partial\tau_{xy}}{\partial x} + \frac{\partial\tau_{yy}}{\partial y} + \frac{\partial\tau_{zy}}{\partial z}\right) \\ &+ w\left(\frac{\partial\tau_{xz}}{\partial x} + \frac{\partial\tau_{yz}}{\partial y} + \frac{\partial\tau_{zz}}{\partial z}\right) + \mathbf{V}\cdot\mathbf{S}_M\end{aligned} \tag{32}$$

If Equation 32 is subtracted from Equation 31, only the part related to internal energy will be left as shown in Equation 33.

$$\begin{aligned}\rho\frac{Di}{Dt} =& - div(P\mathbf{V}) + div(k\, grad(T)) + \tau_{xx}\frac{\partial u}{\partial x} + \tau_{yx}\frac{\partial u}{\partial y} + \tau_{zx}\frac{\partial u}{\partial z} \\ &+ \tau_{xy}\frac{\partial v}{\partial x} + \tau_{yy}\frac{\partial v}{\partial y} + \tau_{zy}\frac{\partial v}{\partial z} + \tau_{xz}\frac{\partial w}{\partial x} + \tau_{yz}\frac{\partial w}{\partial y} + \tau_{zz}\frac{\partial w}{\partial z} + S_i\end{aligned} \tag{33}$$

$$S_i = S_E - \mathbf{V}\cdot\mathbf{S}_M \tag{34}$$

The energy equation given in Equation 31 can be re-arranged for the compressible flows by using the enthalpy. Definitions needed for this re-arrangement are given in Equations 35 and 36.

$$h = i + \frac{P}{\rho} \tag{35}$$

$$h_0 = h + \frac{1}{2}(u^2+v^2+w^2) = E + \frac{P}{\rho} \tag{36}$$

When Equation 36 is put into Equation 31, the alternative version of the energy equation is achieved as shown in Equation 37 [1].

$$\begin{aligned}\frac{\partial(\rho h_0)}{t} + div(\rho h_0 \mathbf{V}) =& div(k\, grad(T)) + \frac{\partial P}{\partial t} + \frac{(\partial u\tau_{xx})}{\partial x} + \frac{(\partial u\tau_{yx})}{\partial y} + \frac{(\partial u\tau_{zx})}{\partial z} \\ &+ \frac{(\partial v\tau_{xy})}{\partial x} + \frac{(\partial v\tau_{yy})}{\partial y} + \frac{(\partial v\tau_{zy})}{\partial z} \\ &+ \frac{(\partial w\tau_{xz})}{\partial x} + \frac{(\partial w\tau_{yz})}{\partial y} + \frac{(\partial w\tau_{zz})}{\partial z} + S_h\end{aligned} \tag{37}$$

3.1.5 State Equations

For the unknown variables density, pressure and temperature, assumption of thermodynamic equilibrium is used [1]. The fluid is able to adjust itself thermodynamically very fast when fluid conditions change, which can be considered instantaneous. Therefore, it is safe to say that the fluid always stays in thermodynamic equilibrium.

It is possible to define the state of substance using only two state variables with the help of thermodynamic equilibrium [1]. State equations are used for these relations. In terms of this work, perfect gas state equations are used as given in Equations 38 and 39.

$$P = \rho RT \tag{38}$$

$$i = c_v T \tag{39}$$

3.1.6 Navier-Stokes Equations

Governing equations derived so far contain viscous stresses, which are unknown. These viscous stresses can be expressed as functions of the local deformation rate or strain rate [1]. The local deformation rate consists of the linear deformation and the volumetric deformation in three dimensional flows.

It is assumed that all gasses and many liquids are isotropic [1]. The rate of linear deformation of a fluid element is composed of nine components in three dimensions with six of them being independent for isotropic flows. These are shown with, s_{ij}, which shares the same suffix system with the viscous stresses.

Three of the linear elongating deformation components are given in Equation 40.

$$s_{xx} = \frac{\partial u}{\partial x} \quad s_{yy} = \frac{\partial v}{\partial y} \quad s_{zz} = \frac{\partial w}{\partial z} \tag{40}$$

Six of shearing linear deformation components are given in Equations 41, 42 and 43.

$$s_{xy} = s_{yx} = \frac{1}{2}\left(\frac{\partial u}{\partial y} + \frac{\partial v}{\partial x}\right) \tag{41}$$

$$s_{xz} = s_{zx} = \frac{1}{2}\left(\frac{\partial u}{\partial z} + \frac{\partial w}{\partial x}\right) \tag{42}$$

$$s_{yz} = s_{zy} = \frac{1}{2}\left(\frac{\partial v}{\partial z} + \frac{\partial w}{\partial y}\right) \tag{43}$$

The volumetric deformation is as given in Equation 44.

$$\frac{\partial u}{\partial x} + \frac{\partial v}{\partial y} + \frac{\partial w}{\partial z} = div(\mathbf{V}) \tag{44}$$

For Newtonian fluids, the viscous stresses are proportional to the rates of deformation [1]. In terms of compressible flows, Newton's law of viscosity in three-dimensional form is used, which uses two constants of proportionality. The first constant is first viscosity, which is also known as dynamic viscosity, μ, and it is used to establish a relation between stresses and linear deformations. The second constant is second viscosity, λ, and it is used to establish a relation between stresses and the volumetric deformation. The viscous stresses modeled with these deformation rates are shown in Equations 45-50.

$$\tau_{xx} = 2\mu\frac{\partial u}{\partial x} + \lambda\, div(\mathbf{V}) \tag{45}$$

$$\tau_{yy} = 2\mu\frac{\partial v}{\partial y} + \lambda\, div(\mathbf{V}) \tag{46}$$

$$\tau_{zz} = 2\mu\frac{\partial w}{\partial z} + \lambda\, div(\mathbf{V}) \tag{47}$$

$$\tau_{xy} = \tau_{yx} = \mu\left(\frac{\partial u}{\partial y} + \frac{\partial v}{\partial x}\right) \tag{48}$$

$$\tau_{xz} = \tau_{zx} = \mu\left(\frac{\partial u}{\partial z} + \frac{\partial w}{\partial x}\right) \tag{49}$$

$$\tau_{yz} = \tau_{zy} = \mu\left(\frac{\partial v}{\partial z} + \frac{\partial w}{\partial y}\right) \tag{50}$$

The second viscosity, λ, has small effect in practice, and for gasses an approximation defined by Schlichting can be used as given in Equation 51[1].

$$\lambda = \frac{2}{3}\mu \tag{51}$$

By putting these viscous stress relations given in Equations 45-50 into the governing equations, Navier-Stokes equations are obtained. First, the momentum equation in x-direction will be used for the implementation.

$$\begin{aligned}\rho\frac{Du}{Dt} = &-\frac{\partial P}{\partial x} + \frac{\partial}{\partial x}\left[2\mu\frac{\partial u}{\partial x} + \lambda\, div(\mathbf{V})\right] \\ &+ \frac{\partial}{\partial y}\left[\mu\left(\frac{\partial u}{\partial y} + \frac{\partial v}{\partial x}\right)\right] \\ &+ \frac{\partial}{\partial z}\left[\mu\left(\frac{\partial u}{\partial z} + \frac{\partial w}{\partial x}\right)\right]\end{aligned} \tag{52}$$

The viscous stress terms are arranged again to make the equations more compact as shown in Equation 53.

$$\begin{aligned}&\frac{\partial}{\partial x}\left(\mu\frac{\partial u}{\partial x}\right) + \frac{\partial}{\partial y}\left(\mu\frac{\partial u}{\partial y}\right) + \frac{\partial}{\partial z}\left(\mu\frac{\partial u}{\partial z}\right) \\ &+ \frac{\partial}{\partial x}\left(\mu\frac{\partial u}{\partial x}\right) + \frac{\partial}{\partial y}\left(\mu\frac{\partial v}{\partial x}\right) + \frac{\partial}{\partial z}\left(\mu\frac{\partial w}{\partial x}\right) \\ &+ \frac{\partial}{\partial x}\left(\lambda\, div(\mathbf{V})\right) \\ &= div(\mu\, grad(u)) + [s_{M_x}]\end{aligned} \tag{53}$$

The smaller contributions shown as $[s_{M_x}]$ will be included in the momentum source S_{M_x}. With this, the momentum equation in x-direction becomes Equation 54.

$$\rho\frac{Du}{Dt} = -\frac{\partial P}{\partial x} + div(\mu\, grad(u)) + S_{M_x} \tag{54}$$

In the same manner, y and z momentum equations are turned into Equations 55 and 56, respectively.

$$\rho\frac{Dv}{Dt} = -\frac{\partial P}{\partial y} + div(\mu\, grad(v)) + S_{M_y} \tag{55}$$

$$\rho\frac{Dw}{Dt} = -\frac{\partial P}{\partial z} + div(\mu\, grad(w)) + S_{M_z} \tag{56}$$

For the energy equation, with the use of Newtonian model for viscous stresses, Equation 57 can be obtained [1].

$$\rho\frac{Di}{Dt} = -P\,div(\mathbf{V}) + div(k\,grad(T)) + f_{Disp} + S_i \tag{57}$$

f_{Disp} is the dissipation function as given in Equation 58.

$$\begin{aligned} f_{Disp} =& 2\mu\left[\left(\frac{\partial u}{\partial x}\right)^2 + \left(\frac{\partial u}{\partial x}\right)^2 + \left(\frac{\partial u}{\partial x}\right)^2\right] \\ &+ \mu\left[\left(\frac{\partial u}{\partial y} + \frac{\partial v}{\partial x}\right)^2 + \left(\frac{\partial u}{\partial z} + \frac{\partial w}{\partial x}\right)^2 + \left(\frac{\partial v}{\partial z} + \frac{\partial w}{\partial y}\right)^2\right] \\ &+ \lambda\,(div(\mathbf{V}))^2 \end{aligned} \tag{58}$$

3.2 Turbulence

Most of the fluid flow seen around the nature are turbulent. Even though turbulent flow has no actual definition, it has six characteristic features, which are explained below.

- Irregularity: Turbulent flows are random and chaotic. There are wide range of eddy sizes, various scales, in a turbulent flow [27]. Eddy is a fluid phenomenon seen in turbulent flows, which can be described as swirling of a fluid that creates a reverse current in the flow.

- Diffusivity: Diffusivity inside turbulent flows are higher compared to non-turbulent ones [27]. This is why boundary layer thickness becomes smaller at the same location as the flow turns to a turbulent one. Due to increased diffusivity, the flow with higher momentum is pulled into the boundary layer, which increases the momentum inside the boundary layer.

- Large Reynolds Numbers: Reynolds number is a non-dimensional number used for characterizing the flow. Turbulent flows have high Reynolds numbers.

- Three Dimensional: Turbulent flows are three dimensional, but if the equations are averaged with respect to time, it is possible to deal with turbulence

in two dimensions [27].

- Dissipation: The energy of small eddies are turned into internal energy [27]. Middle sized eddies get energy from large eddies. Large eddies get their energy from the mean flow. The process of this energy devolution from largest to smallest eddies is called *cascade process*.

- Continuum: The small eddies in a turbulent flow are bigger compared to the molecular scale. Therefore, it is okay to assume flow as a continuum [27].

3.2.1 Reynolds Averaged Navier Stokes Equations

The effect of turbulence on a 2D control volume is shown in Figure 6. As it

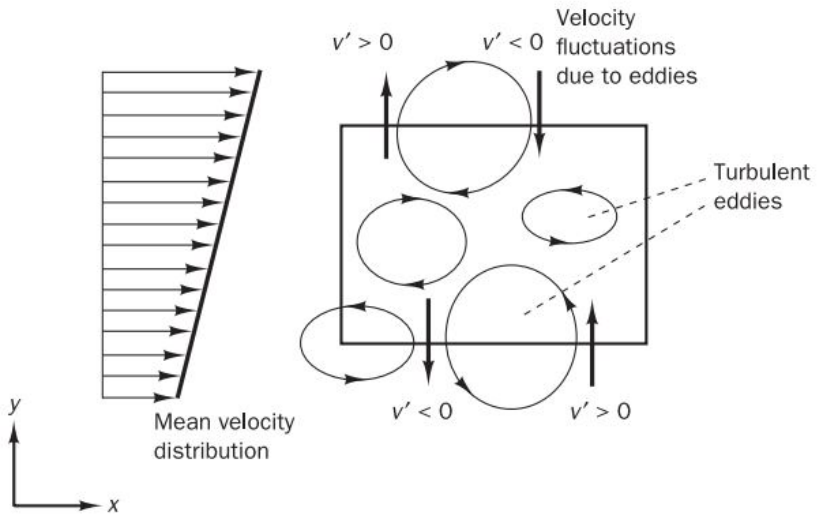

Figure 6: Turbulent Shear Flow on a 2D Control Volume [1]

can be seen, due to turbulent eddies, there is a very strong mixing [1]. Eddies close to the control volume boundaries create random currents, transporting fluid through the boundaries. These currents carry momentum and energy into and out of the control volume. These turbulent eddies cause momentum exchange due to convective transport. This causes slower layers of the fluid to accelerate and faster layers of the fluid to decelerate. Due to this transport, fluid layers will feel additional turbulent shear stresses. These turbulent shear stresses are also known as Reynolds stresses.

It is possible to solve for this turbulent behavior without adding anything to the Navier-Stokes equations [28]. These are called Direct Numerical Simulations (DNS), and are computationally very expensive. In order to achieve a computationally cheaper option, turbulent flows are separated into time-averaged parts, $\bar{U}$, and fluctuating part, u, which makes up the actual flow property, $U = \bar{U} + u$ [27]. The equations result from this approach are called Reynolds Averaged Navier Stokes (RANS) equations. The RANS equations for compressible flows are as shown in Equations 59-63.

$$\frac{\partial \bar{\rho}}{\partial t} + div(\bar{\rho}\tilde{\mathbf{U}}) = 0 \tag{59}$$

$$\frac{\partial \bar{\rho}\tilde{U}}{\partial t} + div(\bar{\rho}\tilde{U}\tilde{\mathbf{U}}) = -\frac{\partial \bar{P}}{\partial x} + div(\mu\, grad(\tilde{U})) + \left[-\frac{\partial\left(\overline{\bar{\rho}u'^2}\right)}{\partial x} - \frac{\partial\left(\overline{\bar{\rho}u'v'}\right)}{\partial y} - \frac{\partial\left(\overline{\bar{\rho}u'w'}\right)}{\partial z}\right] + S_{M_x} \tag{60}$$

$$\frac{\partial \bar{\rho}\tilde{V}}{\partial t} + div(\bar{\rho}\tilde{V}\tilde{\mathbf{U}}) = -\frac{\partial \bar{P}}{\partial y} + div(\mu\, grad(\tilde{V})) + \left[-\frac{\partial\left(\overline{\bar{\rho}u'v'}\right)}{\partial x} - \frac{\partial\left(\overline{\bar{\rho}v'^2}\right)}{\partial y} - \frac{\partial\left(\overline{\bar{\rho}v'w'}\right)}{\partial z}\right] + S_{M_y} \tag{61}$$

$$\frac{\partial \bar{\rho}\tilde{W}}{\partial t} + div(\bar{\rho}\tilde{W}\tilde{\mathbf{U}}) = -\frac{\partial \bar{P}}{\partial z} + div(\mu\, grad(\tilde{W})) + \left[-\frac{\partial\left(\overline{\bar{\rho}u'w'}\right)}{\partial x} - \frac{\partial\left(\overline{\bar{\rho}v'w'}\right)}{\partial y} - \frac{\partial\left(\overline{\bar{\rho}w'^2}\right)}{\partial z}\right] + S_{M_z} \tag{62}$$

$$\frac{\partial \bar{\rho}\tilde{\Phi}}{\partial t} + div(\bar{\rho}\tilde{\Phi}\tilde{\mathbf{U}}) = div(\Gamma_\Phi\, grad(\tilde{\Phi})) + \left[-\frac{\partial\left(\overline{\bar{\rho}u'\phi'}\right)}{\partial x} - \frac{\partial\left(\overline{\bar{\rho}v'\phi}\right)}{\partial y} - \frac{\partial\left(\overline{\bar{\rho}w'\phi'}\right)}{\partial z}\right] + S_\Phi \tag{63}$$

The overbar is for time averaging and the tilde is for density-weighting or Favre-averaging [1]. In Equation 63, the Φ is for an arbitrary scalar quantity, like temperature, and Γ_Φ is the diffusion coefficient for that quantity.

The terms that correspond to Reynolds stresses in Equations 60, 61 and 62 are given in Equations 64 and 65, which give normal stresses and shear stresses,

respectively [1].

$$\tau_{xx} = \overline{\rho u'^2} \quad \tau_{yy} = \overline{\rho v'^2} \quad \tau_{zz} = \overline{\rho w'^2} \tag{64}$$

$$\tau_{xy} = \tau_{yx} = \overline{\rho u'v'} \quad \tau_{xz} = \tau_{zx} = \overline{\rho u'w'} \quad \tau_{yz} = \tau_{zy} = \overline{\rho v'w'} \tag{65}$$

3.2.2 Turbulence Modelling

As it was mentioned before, separating the flow properties into mean and fluctuating parts was a relatively cheaper solution devised to include the effect of turbulence into the fluid flow simulation. This separation is done to reduce the computational resources needed to resolve all eddy sizes. In order to achieve this, the flow quantities are averaged out since most of the time the mean values of these quantities are the main interest of the solution [27].

When RANS equations are examined, the additional term Reynolds stress tensor, which reflect the relation between oscillating velocities, is added in the original Navier-Stokes equations [27]. Turbulence models come in to close the equation set with this extra term added.

There are several different turbulent models. Main categorization of these models are as explained below.

- Algebraic Models: To compute the turbulent viscosity an algebraic equation is used with these models. The assumption incorporated in these models is called *Boussinesq Assumption*. Reynolds stress tensor is correlated to the velocity gradient and the turbulent viscosity with using this assumption [27].

- One Equation Models: A transport equation is worked for a turbulent quantity, which is mostly the turbulent kinetic energy, k, [27]. For the second turbulent quantity the same way is followed as in the algebraic models. The turbulent viscosity is obtained with the use of *Boussinesq Assumption*.

- Two Equation Models: Other name for these models is eddy viscosity models [27]. To characterize transport of two scalars, two transport equations

are derived. An example for these two turbulent scalars are turbulent kinetic energy, k, and its dissipation, ϵ. With an assumption that correlates Reynolds stress tensor to the velocity gradients and eddy viscosity, Reynolds stress tensor is calculated.

- Reynolds Stress Models: With these models, a transport equation is defined for the Reynolds stress tensor [27]. Another equation is also added to find the length scale of the turbulence. This is mostly achieved by using an equation for the dissipation.

It was mentioned that some of the turbulence models use an assumption called *Boussinesq Assumption*. This is an assumption used in eddy viscosity turbulence models that correlates Reynolds stresses to the velocity gradients with turbulent viscosity. This correlation is done by replacing the Reynolds stress tensor in the time-averaged Navier-Stokes equations with the multiplication of turbulent viscosity and the velocity gradients.

One of the most popular turbulence models under one equation models is Spalart-Allmaras (SA) [29]. SA is first suggested in 1992. Prior models before SA handled the boundary layer as a single, tightly coupled module. However, this approach was incorrect in the presence of detachment and multiple shear layers. Also, non-local models were expensive and awkward whey they are used with unstructured grids. Another issue was to accurately predict the shock-boundary layer interactions. SA was developed with these downsides of other turbulence models in mind. It is still a very accurate turbulence model that is still being used.

For two equations turbulence models, there are two models that have high popularity to this date, $k-\epsilon$ and $k-\omega$ turbulence models. Both of these models have advantages and disadvantages. The biggest failure of two equation models is not being able to predict the onset and amount of separation in adverse pressure gradient [30]. $k-\epsilon$ model over predicts the shear stress in adverse pressure gradient flows [31]. This is related to $k-\epsilon$ turbulence model having too low dissipation, and

as a result of that, too big length scale in adverse pressure gradient flows. $k-\omega$ turbulence model, which was first proposed by Wilcox [32], is somewhat ahead of $k-\epsilon$ with its better performance in the sublayer of the boundary layer [30]. Also, unlike $k-\epsilon$, $k-\omega$ does not require damping functions, and it is possible to use basic Dirichlet boundary conditions with it. However, even though $k-\omega$ turbulence model shows great performance in some situations, it fails to correctly predict the asymptotic behavior of the turbulence as it nears a wall. Due to eddy viscosity being much smaller to molecular viscosity close to the surface, asymptotic behavior of the mean profile is not dependent on the asymptotic form of the turbulence. Thus, even though the $k-\omega$ turbulence model is not consistent asymptotically near a wall, it is possible to predict the mean flow profile and the wall skin friction correctly.

Another point where $k-\omega$ is worse compared to $k-\epsilon$ turbulence model is with the k and ϵ distribution representation [30]. Due to its damping functions, $k-\epsilon$ is more in agreement with DNS data in that regard. However, damping functions have very little effect on predicting velocity profiles and skin friction at high Reynolds number flows. The main and most often time the only information the mean flow solver takes from the turbulence model is the eddy viscosity.

In the logarithmic region of the boundary layer, $k-\omega$ is better compared to $k-\epsilon$ in equilibrium adverse pressure gradient flows and in compressible flows [30]. However, due to the small effect of logarithmic region has on the results for strong adverse pressure gradients, $k-\omega$ suffers in predicting the pressure induced seperation. When predicting strong adverse pressure gradient flows, the eddy viscosity in the wake region is much more important compared to logarithmic region performance. For the wake region, $k-\omega$ shows a strong dependence on the freestream value of ω, which is a specific rate of dissipation [33], while $k-\epsilon$ does not show the same dependency [30].

Both $k-\omega$ and $k-\epsilon$ turbulence models show great performance in some cases and fail in some. After determining strong and weak sides of both of these models,

another model that combines the strong sides of these models is developed, which is called Shear Stress Transport (SST) [30][34]. SST is an eddy viscosity model with the combination of $k-\omega$ and $k-\epsilon$, and includes the effect of the transport of the principal turbulent shear stress, which is a feature of Reynolds stress turbulence models [27][30].

By combining $k-\omega$ and $k-\epsilon$ models, model with the better performance can be selected at different regions of the flow. To be able to do this, the standard high Reynolds number version of $k-\epsilon$ model is transformed to a $k-\omega$ formulation first [30]. After that, the transformed $k-\epsilon$ formulation will be multiplied by a blending function $(1-F_1)$ and added to standard $k-\omega$ model, which is multiplied by F_1. The blending function F_1 is to be equal to one in the sublayer and logarithmic regions of the boundary layer, and it will gradually go to zero as wake region is neared.

With this blending function, it is aimed for the model to use original Wilcox $k-\omega$ model in the near wall region and use standard $k-\epsilon$ model in the outer wake region and in free shear layers. Moreover, by altering the definition of eddy viscosity to also consider the transport of principal turbulent shear stress, the SST model gains a considerable performance increase over both the standard $k-\epsilon$ and $k-\omega$ models. Even though it is possible to find improved versions of $k-\omega$[35] and $k-\epsilon$ [36] for special cases, SST holds its popularity due to its wider range of applicability.

CHAPTER IV

BASIC OVERVIEW OF NUMERICAL SCHEMES IN SU2

4.1 Physical Modelling

SU2 is designed to work with PDEs defined in a domain $\Omega \subset R^3$ [37]. The system of equations for the physical modelling of a certain problem can be put into the structure shown in Equation 66.

$$\frac{\partial \mathbf{U}}{\partial t} + \nabla \cdot \mathbf{F}^c + \nabla \cdot (\mu^{vk} \mathbf{F}^{vk}) = \mathbf{Q} \qquad \text{in } \Omega \tag{66}$$

The definitions of the terms shown in Equation 66 are given in Table 1 [37].

Table 1: Definitions of the Terms for General Framework of SU2

$\mathbf{U}$	Vector of state variables
$\mathbf{F}^c(\mathbf{U})$	Convective fluxes
$\mathbf{F}^{vk}(\mathbf{U})$	Viscious fluxes
$\mathbf{Q}(\mathbf{U})$	Generic source term

Different variations of RANS equations are implemented in SU2 [2]. For the compressible formulation, the vector of state variables is shown in Equation 67.

$$\mathbf{U} = (\rho, \rho v_1, \rho v_2, \rho v_3, \rho E)^T \tag{67}$$

In Equation 67; ρ is the density, E is the total energy per unit mass, and $\boldsymbol{v} = (v_1, v_2, v_3)$ is the flow velocity in Cartesian coordinate system [2].

The viscous and convective fluxes for the compressible formulation are as given in Equations 68 and 69 [2].

$$F_i^c = (\rho v_i, \rho v_i v_1 + P\delta_{i1}, \rho v_i v_2 + P\delta_{i2}, \rho v_i v_3 + P\delta_{i3}, \rho v_i H) \tag{68}$$

$$F_i^{vk} = (0, \tau_{i1}, \tau_{i2}, \tau_{i3}, v_j \tau_{ij} + \mu_{tot}^* c_p \partial_i T) \qquad i = 1, 2, 3 \tag{69}$$

In Equations 68 and 69, P is the static pressure, H is the fluid enthalpy, δ_{ij} is the Kronecker delta function, $\tau_{ij} = \mu_{tot}\left(\partial_j v_i + \partial_i v_j - \frac{2}{3}\delta_{ij}\nabla \cdot \boldsymbol{v}\right)$, c_p is the specific heat at constant pressure, T is the temperature and R is the gas constant where $c_p = \frac{\gamma R}{\gamma - 1}$ with γ being a constant [2].

To close the equation system, the dynamic viscosity, μ_{dyn} is taken to be satisfying Sutherland's law, and the turbulent viscosity is calculated with a turbulence model [2].

$$\mu_{tot} = \mu_{dyn} + \mu_{tur} \tag{70}$$

$$\mu^*_{tot} = \frac{\mu_{dyn}}{Pr_d}\frac{\mu_{tur}}{Pr_t} \tag{71}$$

Pr_d and Pr_t in Equations 70 and 71 are dynamic and turbulent Prandtl numbers, respectively [2].

For modelling turbulence, SU2 has SA, SST, and several variations of these two models available. For a detailed investigation of how these models are implemented into SU2, the reference [2] can be examined.

SU2 allows to work with a rotating frame of reference, which is very essential for steady turbomachinery simulations. Rotating frame is where the system of fluid flow equations are transformed into a reference frame. This frame rotates with the interested body [2]. This is especially useful for obtaining steady solutions of rotating bodies, such as turbomachinery, under a constant rotational speed. Transformation to the reference frame of the fluid flow equations are done by adding additional terms to the convective fluxes and source terms. The viscous terms do not need altering.

SU2 is also capable of doing shape optimization via adjoint methodology [2]. In the scope of this work, discrete adjoint methodology that is included in SU2 is investigated for the shape optimization. Adjoint shape optimization method is a gradient based optimization technique. The sensitivity derivatives of the interested surface for the optimization are calculated using given objective and constraint functions with respect to the design variables. These objective and constraint functions and design variables are defined or selected by the user. In

terms of discrete approach, the governing equations are discretized first and then adjoint equations are derived.

4.2 Numerical Implementation

SU2 uses an edge-based data structure to solve both flow and adjoint problems numerically with unstructured meshes [37]. Governing equations are discretized separately in time and space, which allows the use of different integration schemes for space and time.

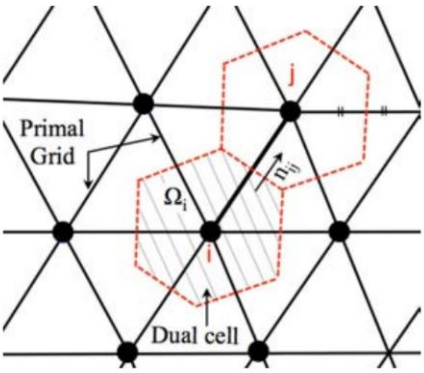

Figure 7: Prime Mesh and Control Volume Representation on a Dual Mesh [2]

4.2.1 Spatial Integration

Finite volume method with a standard edge-based structure on a dual grid control volumes built with a median-dual vertex-based scheme is used for the discretization of the PDEs [37]. In order to obtain median-dual control volumes, centroids, face, and edge midpoints of every cell sharing the distinct node are connected.

The convective and viscous fluxes are calculated at the middle point of an edge. After, the numerical solver goes through every edge in the primal mesh to calculate and integrate these fluxes at all nodes in the numerical grid for obtaining the residuals of all state variables [37]. It is possible to discretize the convective fluxes with centered or upwing schemes. Some of these schemes are Jameson-Schmidt-Turkel (JST) [38], Roe [39], AUSM [40], and HLLC [41]. Roe is a flux-splitting scheme that evaluates the convective fluxes using seperately reconstructed

quantities from surrounding node values on both faces of the control volume [2]. Moreover, Upwind schemes can become second-order accurate in space with higher order reconstruction using Monotonic Upstream Schemes for Convection Laws (MUSCL) [42] together with gradient limiters such as Venkatakrishnan [43] and van Albada Edge [44].

Viscous fluxes are calculated using flow quantities and their first derivatives at the faces of the control volume[2]. Flow variable gradients can be obtained with Green-Gauss[45] or weighted least squares methods at all grid nodes. The flow variables are calculated at the cell faces by taking average of flow variable gradients at nodes.

Source terms are calculated with piecewise constant reconstruction for every finite volume cell [2]. Source terms are important for the formulation of turbulence and transition models.

4.2.2 Time Integration

SU2 contains both implicit and explicit methods for time integration. For the implicit one SU2 incorporates a basic Euler scheme. For the explicit schemes there are Euler and Runge-Kutta methods.

For implicit cases SU2 uses a local time-stepping technique to reach a steady solution faster [2]. With local time stepping, it is possible to advance each cell using different local time steps. CFL Number is used in the determination of these local time steps. For the final part of the time integration, SU2 contains different linear solvers. Currently SU2 has Flexible Generalized Minimal Residual Method (FGMRES) [46][47] and Bi-conjugate Gradient Stabilized Method (BCGSTAB) [48]. These are Krylov subspace methods [37]. For the preconditioner of the Krylov linear solver, there are Lower-Upper Symmetric Gauss Seidel (LU-SGS) [49], Incomplete Lower-Upper Factorization (ILU), Linelet and Jacobi. These preconditioners are used to transform the original system for making it more convenient for the numerical solution.

CHAPTER V

CODE VALIDATION STUDIES

For the validation of SU2, two cases are selected from NASA's verification and validation cases, turbulent flat plate[1] and RAE2822 transonic airfoil[2]. Turbulent flat plate is used to show how well SU2 can handle the turbulent boundary layer flow. The transonic airfoil RAE2822 is used to show how well SU2 can predict the shock location in a transonic flow regime.

5.1 Turbulent Flat Plate

The turbulent flat plate study boundary and operating conditions are as shown in Table 2. The Re_L given in Table 2 is calculated at $1m$ downstream from the start of the flat plate.

Table 2: Turbulent Flat Plate Boundary and Operating Conditions

M_∞	0.2
Re_L	5e6
T_∞	294.44 [K]
P_∞	101352.9 [Pa]
$P_{t_{inlet}}$	118309.8 [Pa]
$T_{t_{inlet}}$	302.4 [K]
P_{outlet}	115056 [Pa]

The mesh used for the turbulent flat plate validation case is a 2D structured mesh, and it is taken from SU2's tutorial[3]. It has 13056 cells and $y+$ values below 1. The domain structure is shown in Figure 8. The mesh is shown in Figure 9.

RANS equations are selected together with the SST turbulence model. Total temperature and pressure are defined at the inlet, and static pressure is defined at

[1] https://turbmodels.larc.nasa.gov/flatplate.html
[2] https://www.grc.nasa.gov/www/wind/valid/raetaf/raetaf.html
[3] https://su2code.github.io/tutorials/Turbulent_Flat_Plate/

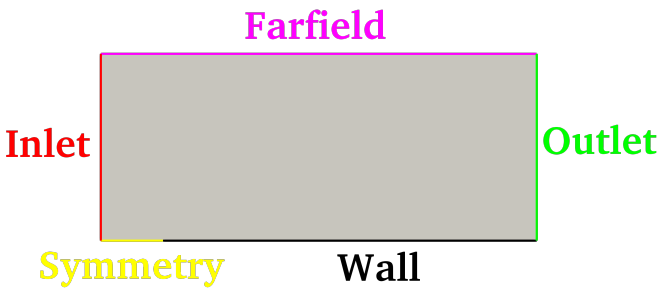

Figure 8: Flat Plate Domain Structure

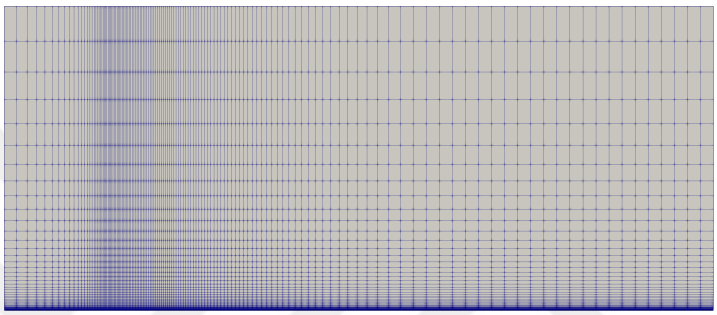

Figure 9: Flat Plate Mesh

the outlet. Top part of the domain is assigned to be outlet as well, defining static pressure. A small portion at the bottom of the domain near the inlet boundary is defined as slip wall to avoid errors by placing a no-slip wall right after the inlet boundary. After the slip wall, the flat plate is defined as no-slip wall. 1^{st} and 2^{nd} Order Roe schemes are used for the turbulent flat plate case with a CFL number of 100.

The y^+ and u^+ values at $1m$ downstream from the start of the flat plate are compared to theoretical results. This is shown in Figure 10. It can be said that SU2 is able to accurately handle a flow with turbulent boundary layer with both 1^{st} and 2^{nd} Order Roe schemes.

The convergence of the flat plate simulation is shown in Figure 12. It can be assumed that the simulation is converged after 50 iterations with its current settings.

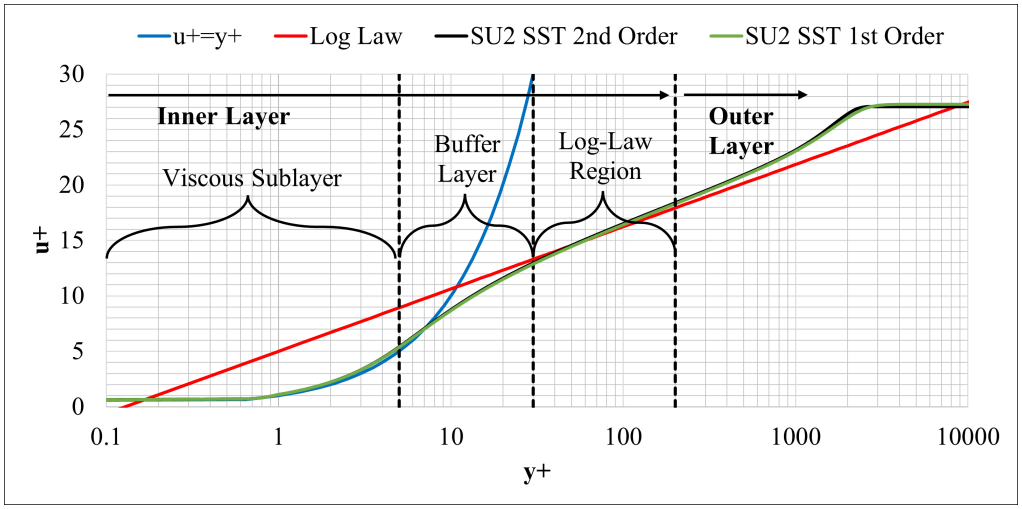

Figure 10: Flat Plate u^+ vs y^+ at $x = 1m$

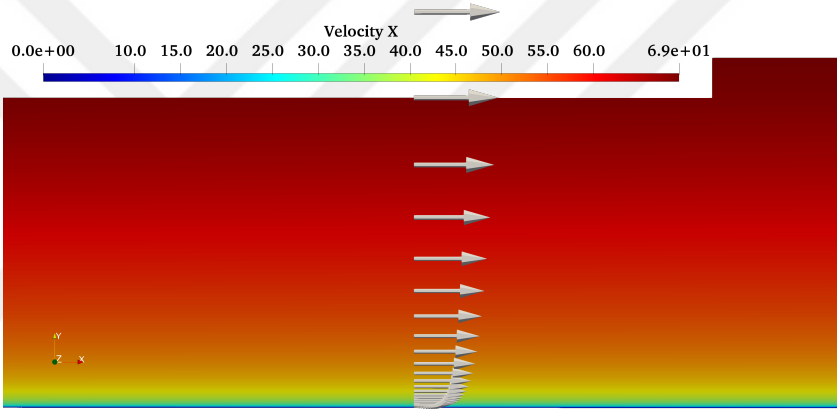

Figure 11: Flat Plate Velocity Contour at $x = 1m$ Inside the Boundary Layer

5.2 Transonic Airfoil: RAE2822

The transonic airfoil RAE2822 study boundary conditions are given in Table 3.

The mesh used for the transonic airfoil RAE2822 validation case is a 2D structured mesh formed with ICEM-CFD. A C-Grid type mesh is used around the airfoil and far field boundaries are put at a sufficient distance away from the airfoil. It has 27177 cells and $y+$ values below 5. The domain structure and mesh are shown in Figure 13 and Figure 14, respectively. The $y+$ values on the airfoil are shown in Figure 15.

RANS equations are selected together with the SST turbulence model. Outer

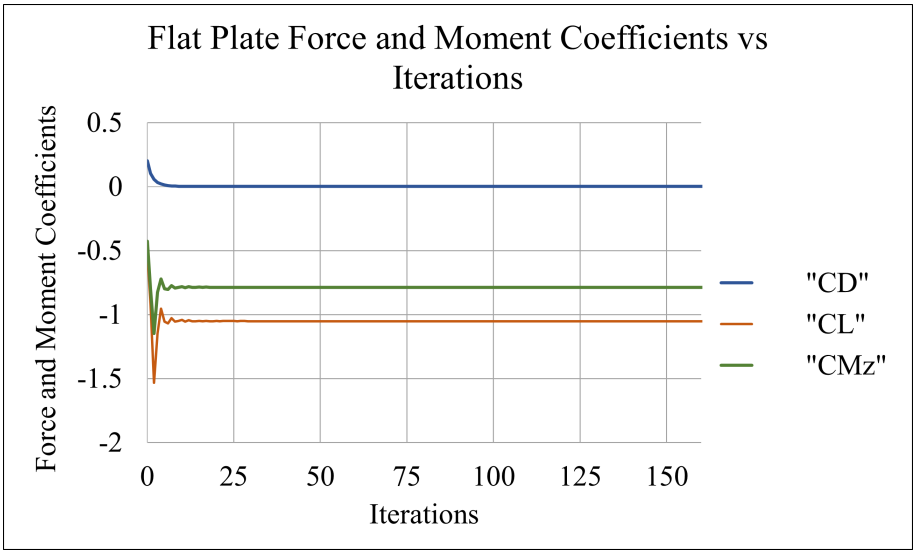

Figure 12: Flat Plate Force and Moment Coefficients vs Iterations

Table 3: Transonic Airfoil RAE2822 Boundary Conditions

M_∞	0.725
α	2.55 [°]
T_∞	255.556 [K]
Re_∞	6.5e6
L_{ref}	0.3048 [m]

most boundaries shown in Figure 13 are defined as far field boundary. Mach number, pressure, temperature and Reynolds number are given at this farfield boundary. The airfoil is defined as no-slip wall. 2^{nd} Order Roe with the Venkatakrishnan limiter and 1^{st} Order Upwind schemes are used for flow and turbulence, respectively. Euler implicit time discretization is selected and a CFL Number of 1000 is used. Since this case has shock formation over the airfoil, using a 2^{nd} order scheme is necessary in order to resolve the location of the shock accurately.

The pressure coefficient, C_p, distribution over the airfoil surface is compared with experimental data. As shown in Figure 16, SU2 is able to determine the location of the shock very accurately. This also confirms that if there is shock formation in the interested case, a 2^{nd} order numerical scheme should be selected. The Mach contour around the airfoil is shown in Figure 17.

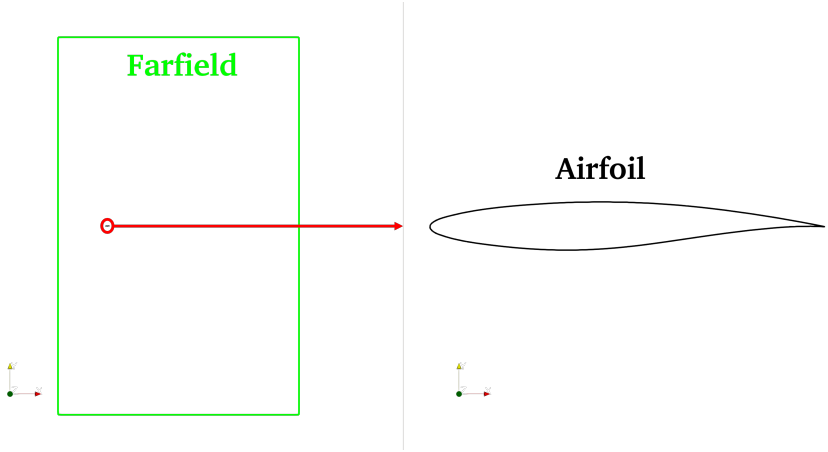

Figure 13: RAE2822 Domain Structure - Farfield (Green) and Airfoil (Black) Surfaces

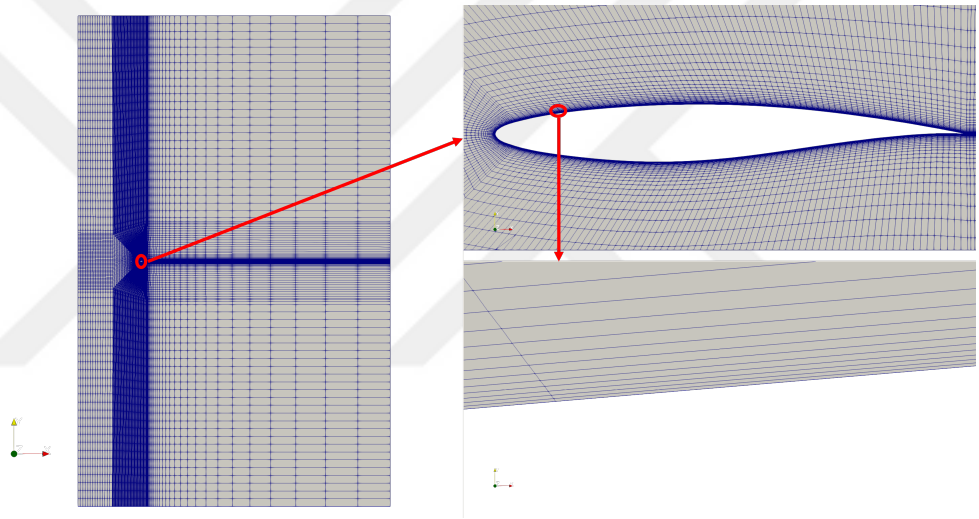

Figure 14: RAE2822 Mesh

The convergence of the flat plate simulation is shown in Figure 18. It can be assumed that the simulation is converged after 200 iterations with its current settings.

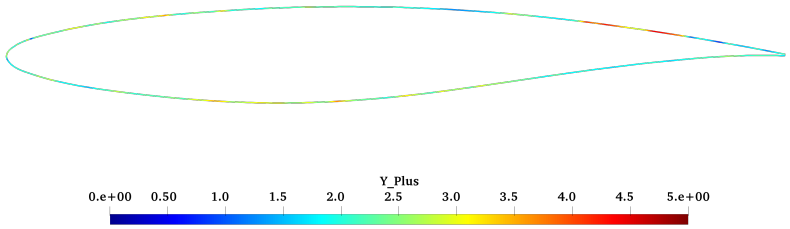

Figure 15: RAE2822 y^+ Values on Airfoil

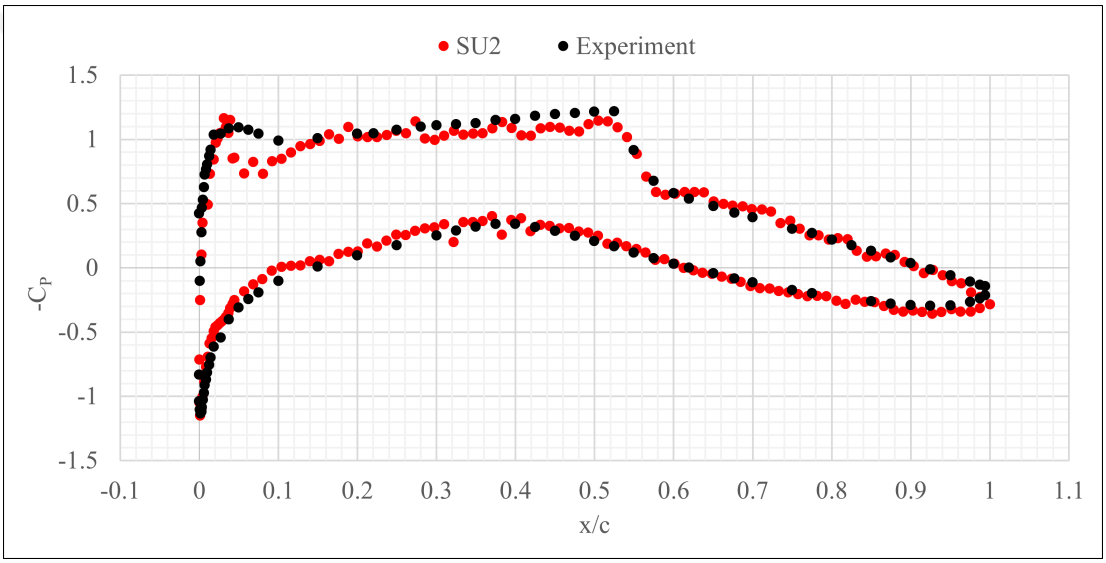

Figure 16: RAE2822 Pressure Coefficient SU2 vs Experimental Data

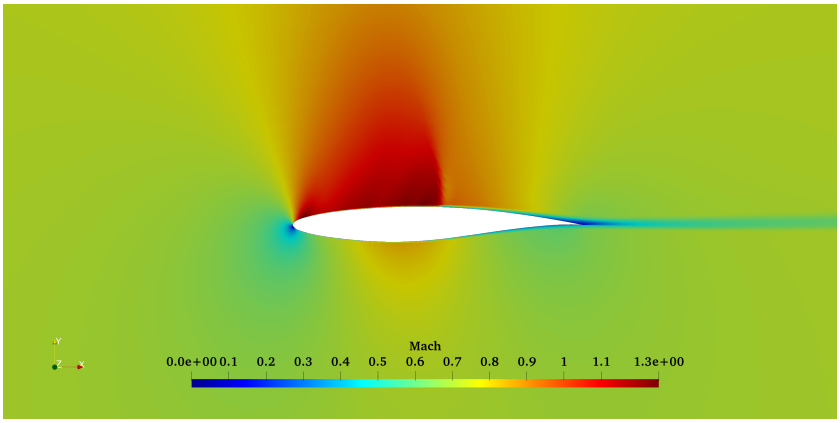

Figure 17: RAE2822 Mach Contour Around the Airfoil

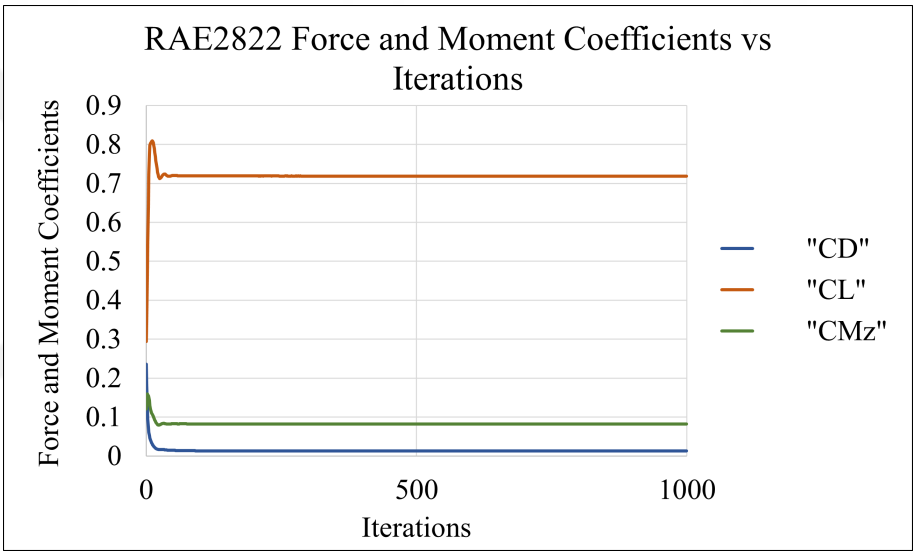

Figure 18: RAE2822 Force and Moment Coefficients vs Iterations

CHAPTER VI

NUMERICAL METHODOLOGY FOR RADIAL COMPRESSOR FLOW ANALYSIS

The capabilities of the solvers in SU2 are tested using two single stage radial compressors, one with a vaneless and the other with a vaned diffuser. Flow paths of these geometries are shown in Figure 19. The compressor stages used for the simulations are tested proprietary designs of MAN Energy Solutions Schweiz AG. All reference data used for the comparison are provided by them, which include results obtained with the commercial CFD software Fidelity Flow and experimental data.

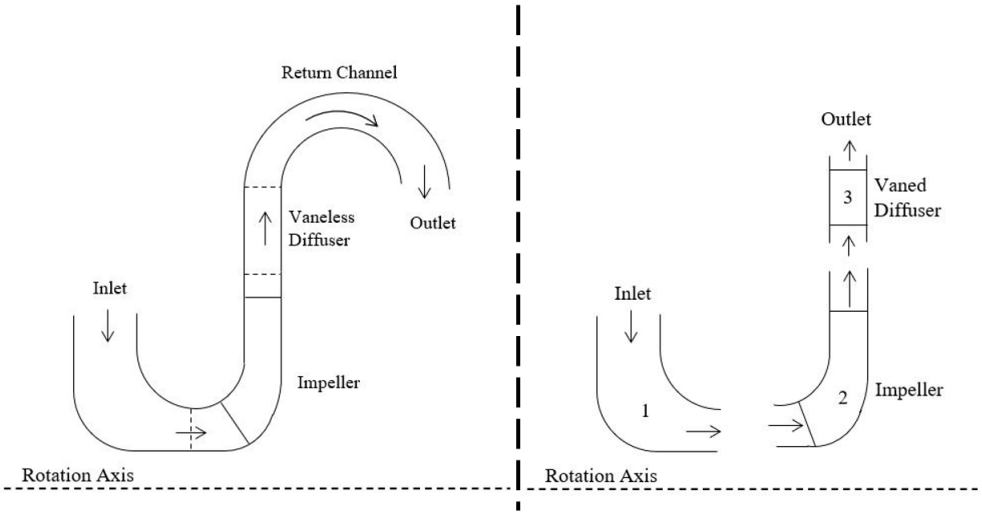

Figure 19: Schematics of Case#1 (Left) and Case#2 (Right)

6.1 Mesh Dependency

Both vaneless and vaned compressor geometries shared the same impeller and inlet designs. The only different part of them were the presence of vane in the diffuser. Therefore, mesh dependency study is conducted by only using the vaned diffuser compressor geometry. The same mesh independent settings were applied

to vaneless diffuser compressor geometry afterwards. Meshes were generated using a commercial grid generator.

Three different meshes are compared for mesh dependency study. Total number of cells for each mesh are given in Table 4.

Table 4: Total Cell Numbers for Each Mesh Used in Mesh Dependency

Mesh#1	Mesh#2	Mesh#3
3.7e5	1.6e6	3.9e6

Mesh dependency study is done by comparing the total enthalpy difference between inlet and outlet faces, Δh_{tot}, and flow coefficient, ϕ, by taking the experimental data as the reference point. The change of these properties as mesh cell number increases are shown in Figure 20 and Figure 21.

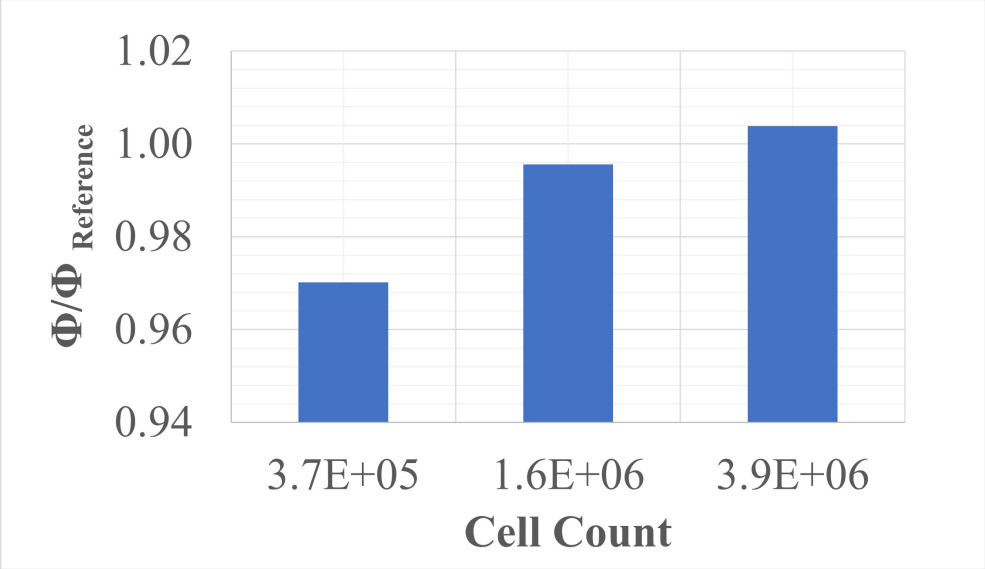

Figure 20: Change of ϕ with Cell Number

Percent changes for Δh_{tot} are 4.32% going from Mesh#1 to Mesh#2, and 0.43% going from Mesh#2 to Mesh#3. Percent changes for *phi* are 2.54% going from Mesh#1 to Mesh#2, and 0.83% going from Mesh#2 to Mesh#3. As it can be seen from Figures 20 and 21 as well, the difference between Mesh#2 and Mesh#3 are under 1%. Thus, it is concluded that Mesh#2 is mesh independent, and it can be used for the flow simulations. The selected mesh has $y+$ values below 5 for the

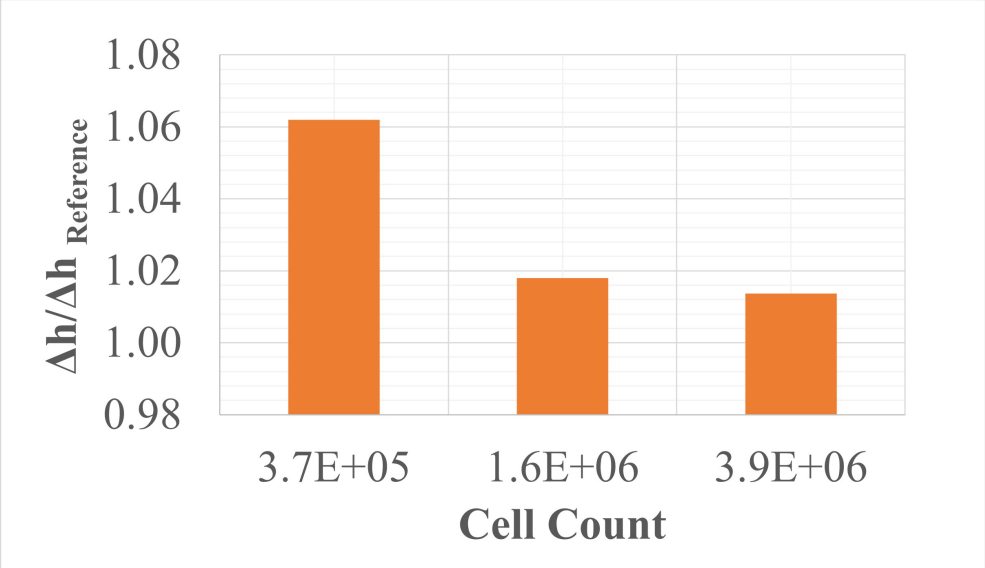

Figure 21: Change of Δh_{tot} with Cell Number

most parts and has $y+$ values below 10 near the trailing edge. Even though no wall function is used, SU2 handled these areas succesfuly. Close ups of impeller blade leading and trailing edges for the selected mesh are shown in Figures 22 and 23.

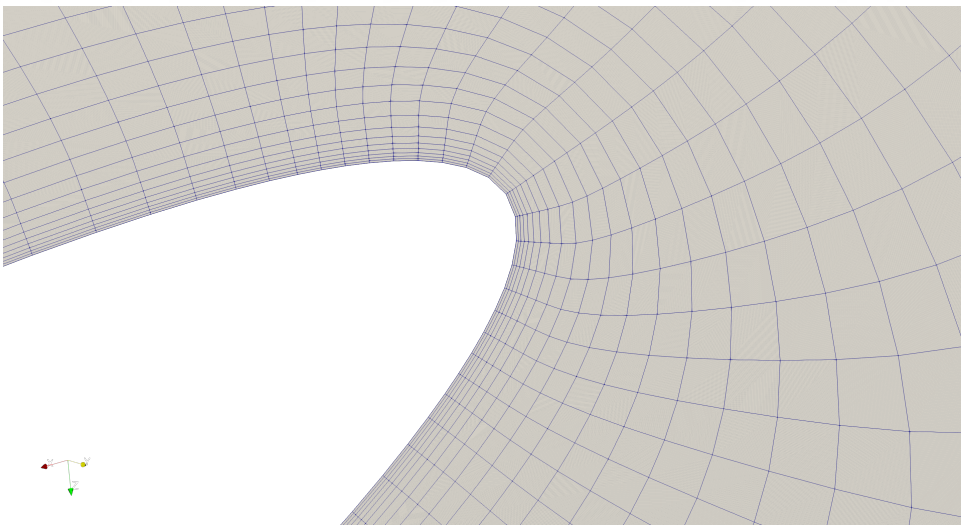

Figure 22: Close-up of the Impeller Leading Edge for Mesh#2

The 2D mesh used for the optimization study is directly taken from the mesh used for Case#2. The diffuser domain of the mesh used in Case#2 is split from other parts and turned from 3D to 2D using StarCCM+. With this, the cell counts

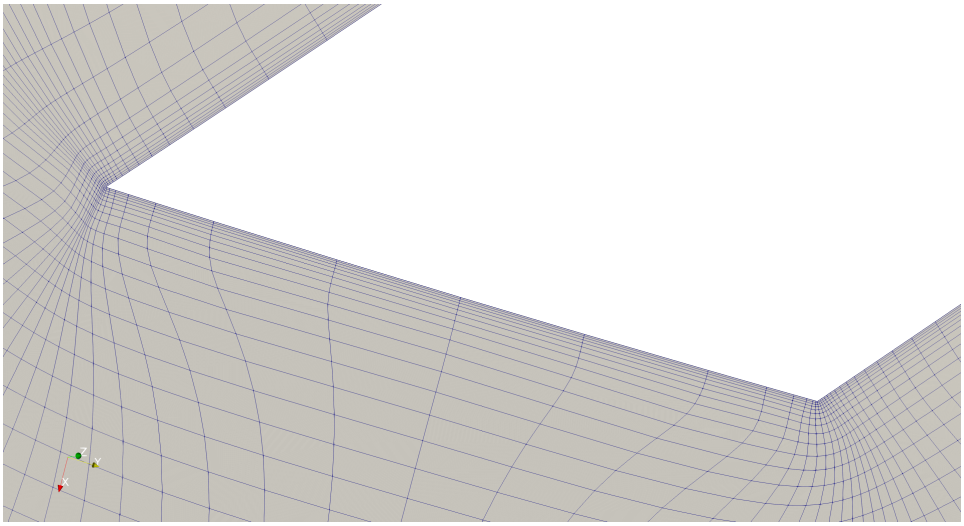

Figure 23: Close-up of the Impeller Trailing Edge for Mesh#2

for the meshes used in Case#1, Case#2 and optimization study are given in Table 5.

Table 5: Cell Counts for the Meshes Used in Each Study

Case#1	1.3e6
Case#2	1.6e6
Optimization Study	1.1e4

For Case#1, a single zone mesh is used. However, for Case#2, since there are both rotating and stationary blades in it, the mesh had to be split up. For Case#2, the mesh is split into three domains, converted to native SU2 format separately, and then combined as a multi-zone mesh in native SU2 format. The 2D mesh used for optimization study had to be converted into native SU2 format as well in order to be able to define necessary information needed for the optimization process onto the mesh. It is possible to use meshes in CGNS format if no domain splitting is required for the problem. However, in order to use multi-zone mesh or define information needed by optimization processes onto the mesh, the mesh has to be in native SU2 format.

6.2 Numerical Methodology

It was mentioned before that two geometries were used for the simulations. Both of these compressor geometries have shrouded impellers. As it can be seen in Figure 19, Case#1 is the one with vaneless diffuser and Case#2 is the one with vaned diffuser. Since Case#1 is vaneless, it is possible to model it as a single zone domain. In the case of Case#2, due to the presence of vane, the domain had to be split up in order to be able to define different rotational speeds for different parts of the geometry.

Case#2 is split into three separate domains, namely, inlet, impeller and diffuser domains. This splitting also came with its need for additional boundary condition assignment for the interfaces between domains. For the interfaces between domains in Case#2, non-reflecting mixing-plane interfaces [50] [51] are used. The name of the setting in SU2 for this type of boundary condition is "MARKER_MIXINGPLANE_INTERFACE", and it takes names of the interface surfaces as outflow and inflow pairs, following the natural growth of the machine.

RANS equations are selected for the problem. In SU2, selecting which set of equations will be solved is the first setting to be set, which has the name "SOLVER". Air is the working fluid, and perfect gas is selected for the state equation, which can be defined under the setting named "FLUID_MODEL" in SU2. In order to be able to simulate a rotating machinery as a steady problem, a moving reference frame has to be used. This change of reference frame is done in SU2 by addition of some source terms to original set of RANS equations. The moving reference frame setting is defined under the name "GRID_MOVEMENT". Constant Courant-Friedrich-Lewy (CFL) [52] number of 20 is used for the simulations. This is selected through trial and error for a relatively stable convergence behavior.

A set of different parameters are used for the comparison of the results obtained with SU2 and the reference data. These are given in Table 6 together with the constant required in calculations. The subscripts 1 and 5 in Table 6 represent

where that property is calculated, inlet and outlet faces, respectively.

Table 6: Parameters Used for the Performance Evaluations

Parameter Name	Definition
Polytropic Efficiency (Total to Total)	$\eta = \frac{R}{c_p} \frac{\log \frac{P_{t_5}}{P_{t_1}}}{\log \frac{T_{t_5}}{T_{t_1}}}$
Work Input Coefficient	$\mu_0 = \frac{\Delta h_{t_{1-5}}}{u_2^2}$
Pressure Rise Coefficient	$\mu_y = \eta \mu_0$
Volume Flow Coefficient	$\phi = \frac{\dot{m}}{\rho_{t_1} u_2 D_2^2}$
Gass Constant $\left[\frac{J}{kgK}\right]$	R=287.43
Heat Capacity $\left[\frac{J}{kgK}\right]$	$c_p = 1006$
Impeller Tip Rotational Speed $\left[\frac{m}{s}\right]$	$u_2 = \frac{D_2 \omega}{2}$
Impeller Tip Diameter $[m]$	D_2
Mass Flow Rate $\left[\frac{kg}{s}\right]$	$\dot{m}$
Total Density at Inlet Conditions $\left[\frac{kg}{m^3}\right]$	ρ_{t_1}
Rotational Speed $\left[\frac{rad}{s}\right]$	ω
Total Pressure $[Pa]$, Total Temperature $[K]$	P_t, T_t
Total Enthalpy Difference $\left[\frac{J}{kg}\right]$	Δh_t

SA and SST turbulence models are used and compared. Both turbulence models showed similar accuracy and convergence rates. However, even though it is very small, SST showed better accuracy in calculated properties compared to the reference data. The comparison of results obtained using SST and SA turbulence models to the reference data at a relatively challenging operating condition are given in Table 7. With these result, SST turbulence model is selected for the rest of the simulations.

Table 7: Percent Difference Between Performance Parameters of Results Obtained with Different Turbulence Models and Reference Data

SU2 with SST Turbulence Model				
$\dot{m}/\dot{m}_{Ref}$	ϕ/ϕ_{Ref}	η/η_{Ref}	$\mu_0/\mu_{0_{Ref}}$	$\mu_y/\mu_{y_{Ref}}$
3.0	2.5	-7.3	-6.5	-13.3

SU2 with SA Turbulence Model				
$\dot{m}/\dot{m}_{Ref}$	ϕ/ϕ_{Ref}	η/η_{Ref}	$\mu_0/\mu_{0_{Ref}}$	$\mu_y/\mu_{y_{Ref}}$
2.8	2.3	-10.9	-7.9	-18.0

For viscosity and conductivity models, *Sutherland* and *Constant Prandtl* models are selected. Rotational speed of the compressor is set through the setting named "ROTATION_RATE", and z-axis is chosen as the rotation axis. For turbomachinery simulations in SU2, the rotation axis has to be z-axis in order for turbomachinery specific calculations to be accurate.

Walls of the compressor are set as adiabatic, no-slip walls. This is done via the setting named "MARKER_HEATFLUX". This boundary condition requires the name of the surface and constant heat flux through that surface, which is given as zero for adiabatic condition.

A special boundary condition for turbomachinery cases is used for inlet, outlet and interfaces between split domains. This boundary condition is Giles boundary condition [50] [51] and is named as "MARKER_GILES" in SU2 settings. Total temperature and pressure values together with the flow direction with respect to surface normals are given at the inlet. Static pressure is given for the outlet. Mixing plane conditions, whether if its an inflow or outflow interface, are also set with this Giles boundary condition.

A single passage for both compressor geometries is simulated. This eases the meshing side and significantly lowers the cost the analysis for steady turbomachinery cases. In order to be able to simulate a single passage, periodic boundaries must be available. SU2 has periodic boundary conditions implemented in it. However, SU2 requires these periodic faces to be conformal, meaning that the meshes on these periodic faces has to match when they are put on top of each other. The periodic faces are defined using "MARKER_PERIODIC" in SU2 settings.

Green-Gauss is used for the numerical method for spatial gradients. FGMRES is selected for the linear solver together with LU_SGS for the preconditioner of the Krylov linear solver. An Upwind scheme, Roe, is selected for the flow convective numerical method. Even though a MUSCL switch was included in the settings, it was not successful in converging a solution due to non-physical temperature and density values at the cutback type trailing edge of the impeller blade, so only the

1^{st} order version of Roe scheme was used. Backward Euler scheme was selected for the time discretization for both the flow and turbulence. A 1^{st} order scalar Upwind scheme was used for the convective numerical scheme for turbulence.

Convergence of the simulations are monitored through mass flow rates at inlet, outlet, and interfaces if there are any. Performance parameters given in Table 6 are calculated mostly by the direct outputs of SU2. The ones that are not outputted by SU2 are calculated via Paraview using the flow field solution given by SU2.

6.3 Turbomachinery Specific SU2 Settings

In order to use turbomachinery specific boundary conditions "MARKER_GILES" and "MARKER_MIXINGPLANE_INTERFACE", the turbomachinery switch option in the SU2 settings has to be also used. The name of this setting is "MARKER_TURBOMACHINERY", and it takes the names of the surfaces from inlet to outlet for each zone with following the natural growth of the machine.

6.3.1 TURBOMACHINERY_KIND

In SU2, for turbomachinery simulations, there is a specific setting called "TURBOMACHINERY_KIND". This setting must be appointed for every zone in the domain and only the geometries that the available options cover can be simulated with SU2. These options are related with the orientation of inlet and outlet planes of each zone with respect to rotation axis. Depending on the orientation, the correct options must be used to be able to simulate the model. The available options and their explanations of each option are shown in Table 8. The way this option operated is figured out by trial and error since there were no explanations for it in neither SU2's own documentation nor various forums in the internet.

For Case#1, the domain is modeled as single-zone, meaning that no splitting was done. However, due to the bends at the inlet and outlet of the geometry, even though the actual geometry is a centrifugal compressor, the "CENTRIPETAL" option had to be used for "TURBOMACHINERY_KIND" setting. The flow path of Case#1 is shown in Figure 19. Because the inlet and outlet faces of the geometry

Table 8: Available "TURBOMACHINERY_KIND" Options in SU2 with Individual Explanations

Available TURBOMACHINERY_KIND Options	Inlet Orientation with respect to Rotation Axis	Outlet Orientation with respect to Rotation Axis
AXIAL	Surface Normal Parallel to Rotation Axis	
CENTRIFUGAL	Surface Normal Perpendicular to Rotation Axis Outward Facing	
CENTRIPETAL	Surface Normal Perpendicular to Rotation Axis Inward Facing	
CENTRIPETAL_AXIAL	Surface Normal Perpendicular to Rotation Axis Inward Facing	Surface Normal Parallel to Rotation Axis
AXIAL_CENTRIFUGAL	Surface Normal Parallel to Rotation Axis	Surface Normal Perpendicular to Rotation Axis Outward Facing

in Case#1 have surface normals perpendicular to rotation axis and are facing inward, "CENTRIPETAL" option explained in Table 8 had to be used in order to obtain correct results. Using another option would make the calculations incorrect and solution would diverge due to these incorrect calculations.

For Case#2, the domain is modeled as multi-zone. It is split into three individual domains. Each domain had to be assigned a "TURBOMACHINERY_KIND" setting. Therefore, it is important to split the geometry so that every domain can be assigned a correct option from Table 8. Because of this constraint, the return channel in Case#2 had to be omitted since it was not possible to model with available "TURBOMACHINERY_KIND" options. The flow path of Case#2 with split domains are shown in Figure 19. For domain "1", inlet domain, "CENTRIPETAL_AXIAL", for domain "2", impeller domain, "AXIAL_CENTRIFUGAL", and for domain "3", diffuser domain, "CENTRIFUGAL" options for "TURBOMACHINERY_KIND" are used. Interfaces between domains "1" and "2", and "2" and "3" are defined as mixing plane interfaces.

6.3.2 MARKER_SHROUD

"MARKER_SHROUD" is a very simple boundary condition that is very essential for turbomachinery cases. In SU2, rotational speeds are defined as zone specific. Meaning that, in order to define a rotation for a certain part of the geometry, that part has to be split as a domain from rest of the geometry. However, as in the walls can not be split as a different domain. Thus, an extra boundary condition for stationary walls inside the domain had to be defined to make it stationary while other parts in the same domain are defined a rotation. In order to do this, SU2 has a very simple boundary condition setting named "MARKER_SHROUD", which makes the surface stationary even if its in a rotating domain. This option can also be used without enabling the turbomachinery switch in SU2.

CHAPTER VII

CFD ANALYSIS RESULTS

7.1 SU2 vs Commercial Software for Two Operating Points in Case#1

For two perating points, flows fields are compared between SU2, ANSYS-CFX and Fidelity Flow. Case#1 is used for this comparison. Comparison planes are chosen from downstream of the impeller. These comparison stations are shown in Figure 24.

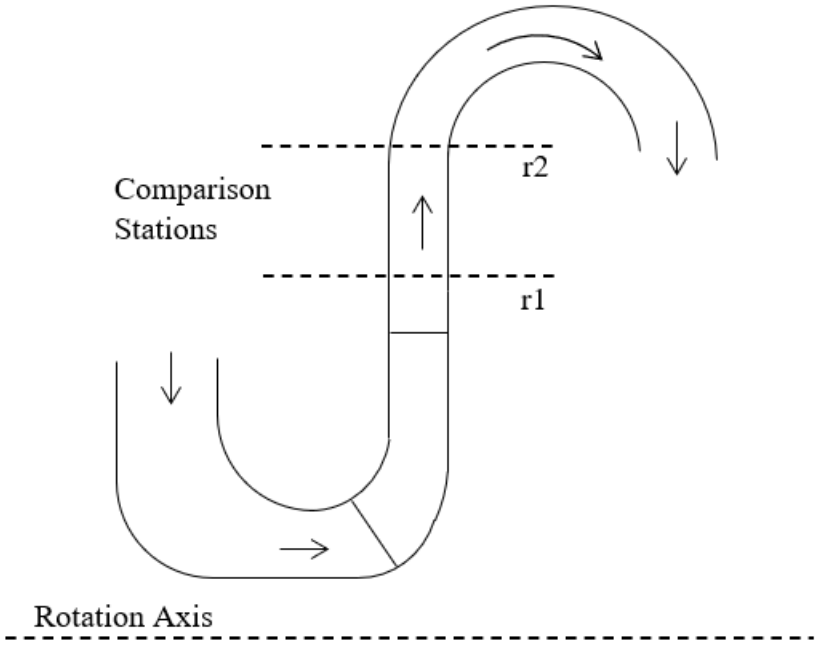

Figure 24: Flow Field Comparison Stations for Case#1

Convergence behaviors of SU2 and ANSYS-CFX are compared for the same operating point. The convergence of both software are monitored with mass flow rates at the inlet and the outlet. SU2 converged to a solution while ANSYS-CFX was showing oscillating behavior. SU2 converged after around 2000 iterations while ANSYS-CFX started oscillating around a certain value after 250 iterations and 250 iterations are run for the averaging, making it total 500 iterations to

calculate a converged solution. Considering ANSYS-CFX is a commercial tool, this is an expected result. To make the comparison between two solvers more consistent, both softwares used a 1^{st} order Upwind scheme. Convergence behaviors of SU2 and ANSYS-CFX are shown in Figures 25 and 26, respectively. Results obtained with Fidelity Flow are provided by MAN Energy Solutions Schweiz AG, and only the end results were available. Therefore, Fidelity Flow is not included in the convergence behavior comparison.

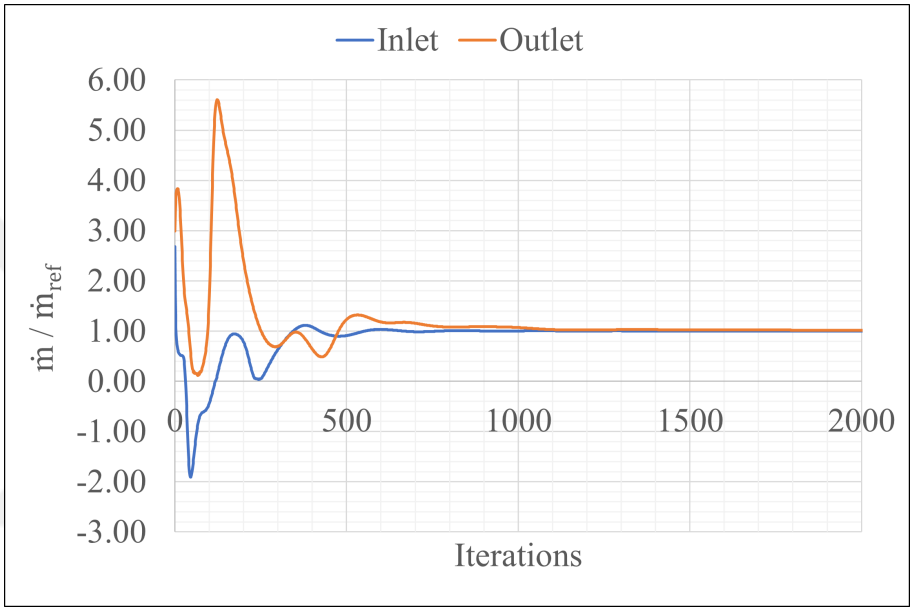

Figure 25: $\frac{\dot{m}}{\dot{m}_{ref}}$ at Inlet and Outlet for Case#1 at a Lower η using SU2

Mass flow rates at the inlet and the outlet faces and polytopic efficiencies calculated using SU2 and ANSYS-CFX are shown in Table 9, divided by a reference value for each parameter. The values for ANSYS-CFX in Table 9 are averaged

Table 9: SU2 vs ANSYS-CFX for an Operating Point

	$\frac{\dot{m}_{Inlet}}{\dot{m}_{Ref}}$	$\frac{\dot{m}_{Outlet}}{\dot{m}_{Ref}}$	$\frac{\eta}{\eta_{Ref}}$
SU2	1.002	1.005	0.966
ANSYS-CFX	0.996	0.995	0.99

values of last 250 iterations out of 500 total iterations. The last converged values are taken for SU2, no averaging was done since it didn't show impactful oscillatory behavior. The time cost is not compared here due to not being able to run both

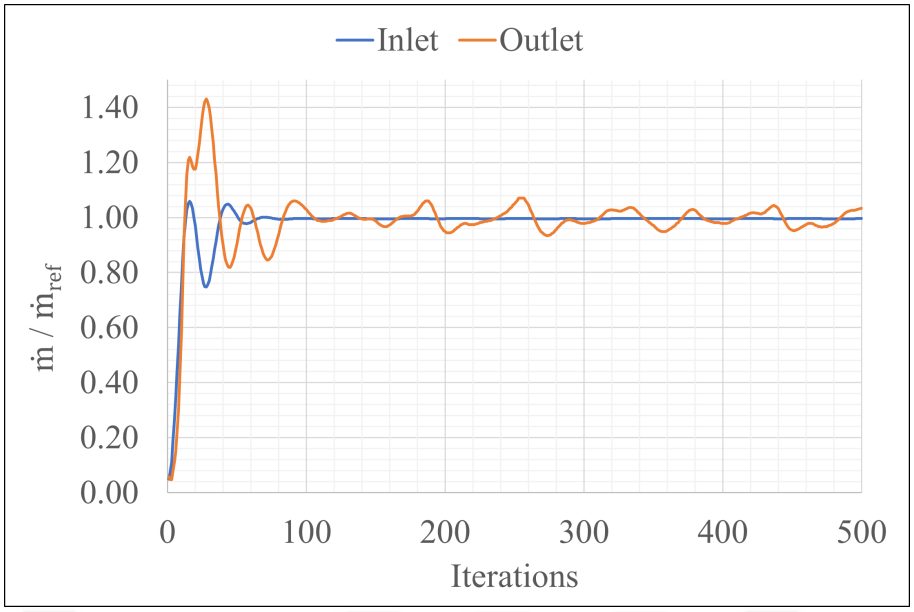

Figure 26: $\frac{\dot{m}}{\dot{m}_{ref}}$ at Inlet and Outlet for Case#1 at a Lower η using ANSYS-CFX

software in the same environment.

Both SU2 and ANSYS-CFX resulted simlar values as shown in Table 9. ANSYS-CFX gave a slightly better result in polytropic efficiency compared to SU2. With Fidelity Flow, a 2^{nd} Order Central spatial scheme with a Jameson type dissipation and an explicit q-stage Runge-Kutta local time stepping scheme was utilised. The differences due to order of spatial scheme are visible in the flow field comparisons. Flow fields are compared for $P_{tot}/P_{tot_{ref}}$ and $T_{tot}/T_{tot_{ref}}$ at the stations shown in 24. Flow field comparisons are given in Appendix A. SU2 and ANSYS-CFX showed similar flow fields for both lower and higher η operating points since both of these software utilised a 1^{st} order Upwind scheme. When SU2 and Fidelity Flow are compared, the difference in the order of spatial scheme is also apparent in the flow fields. SU2 shows a more diffusive behavior in terms of flow structures compared to Fidelity Flow.

7.2 Compressor Performance Prediction SU2 vs Fidelity Flow and Experimental Data

The comparisons are done between results obtained with SU2 using the methodology explained here, reference CFD data generated with commercial software

Fidelity Flow, and reference experimental data. All reference data, both numerical and experimental, are acquired from MAN Energy Solutions Schweiz AG

7.2.1 Results for Case#1

For Case#1, nine operating points are simulated with SU2. The comparison between reference values and SU2 are shown in Figures 27 and 28. Almost at all operating points SU2 and Fidelity Flow are in a very good agreement. In Figure 28, both SU2 and Fidelity Flow results show higher η and lower μ_0 values. This is mainly due to not including cavity flows in the CFD model to keep the model simpler. Including cavity flows in the CFD model would cause higher losses, which in return results with lower efficiency and higher work input coefficients as it is the case with experimental data. However, the agreement between both CFD results and experimental data for μ_0 is better compared to other parameters. This can be explained by the fact that all of these parameters being linked to each other. The over estimation at η is compansated by the under estimation at μ_y, and a smaller difference is seen at μ_0 between CFD results and experimental data.

In Figures 27 and 28, some portions of the reference results are not covered by SU2 due to the outlet boundary condition. There is no boundary condition that imposes mass flow rate at the outlet for compressible flow simulations in SU2. Also, even though mass flow rate boundary condition can be applied at the inlet with velocity, density, and flow direction in cartesian coordinates, for an inlet of an arbitrary shape it becomes very challenging. For inner stage compressors such as our case, being able to define flow direction at the inlet normal to the surface is very much needed.

Pressure contours at leading and trailing edges of two operating points with low and high polytropic efficiencies are shown in Figures 58, 59, 60 and 61 in Appendix A.

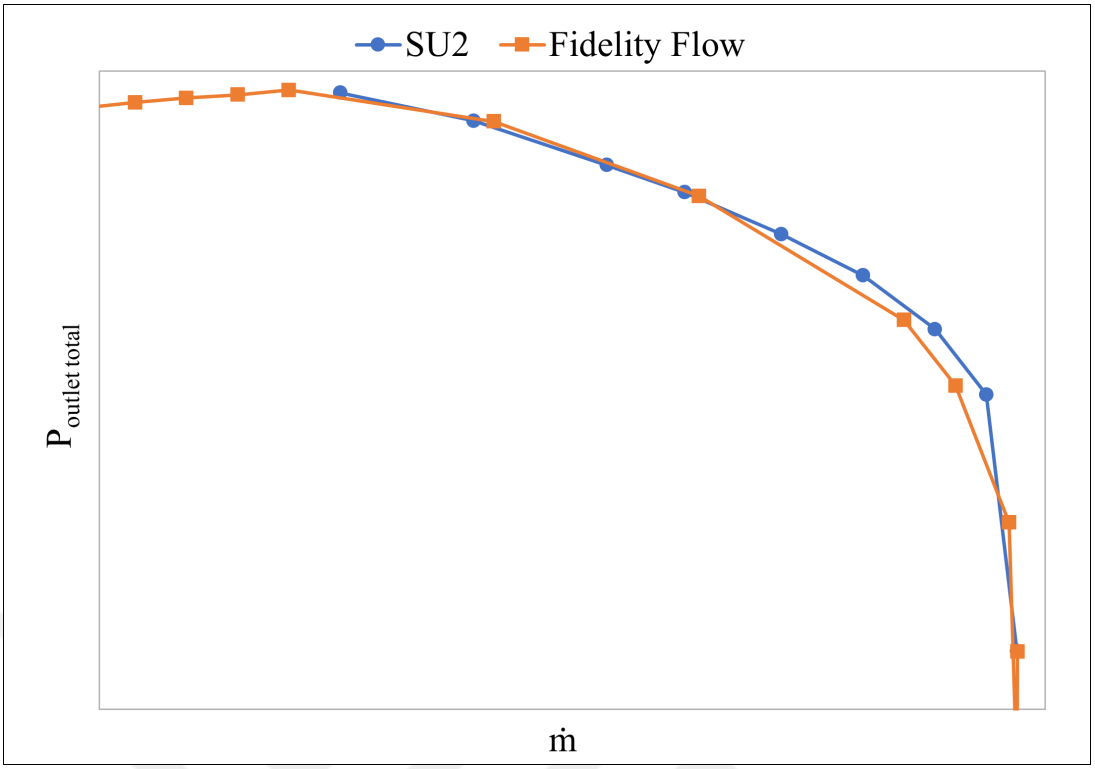

Figure 27: $P_{outlet_{total}}$ vs $\dot{m}$ for Case#1

7.2.2 Results for Case#2

For Case#2, twelve operating points are simulated with SU2. The comparison between SU2 and Fidelity Flow are shown in Figures 29 and 30. Even though the agreement between Fidelity Flow and SU2 results is not as good as Case#1, it still can be considered in agreement overall. In Figure 30, for μ_y and μ_0, at higher ϕ values, a separation between SU2 and Fidelity Flow results can be seen. Also, even though for η SU2 and Fidelity Flow results agree well, SU2 underestimates μ_0 and μ_y values when compared to Fidelity Flow. A similar explanation to Case#1 can be made here as well. Since all of these parameters, η, μ_0 and μ_y, are linked together, an overestimation or underestimation at one of these parameters is transferred to others. In Figure 30 it can be seen that the underestimation at μ_0 is transferred to μ_y.

As it was explained for Case#1 results, the same behavior is apparent for Case#2 as well. Some of the operating points are not covered by SU2 due to not

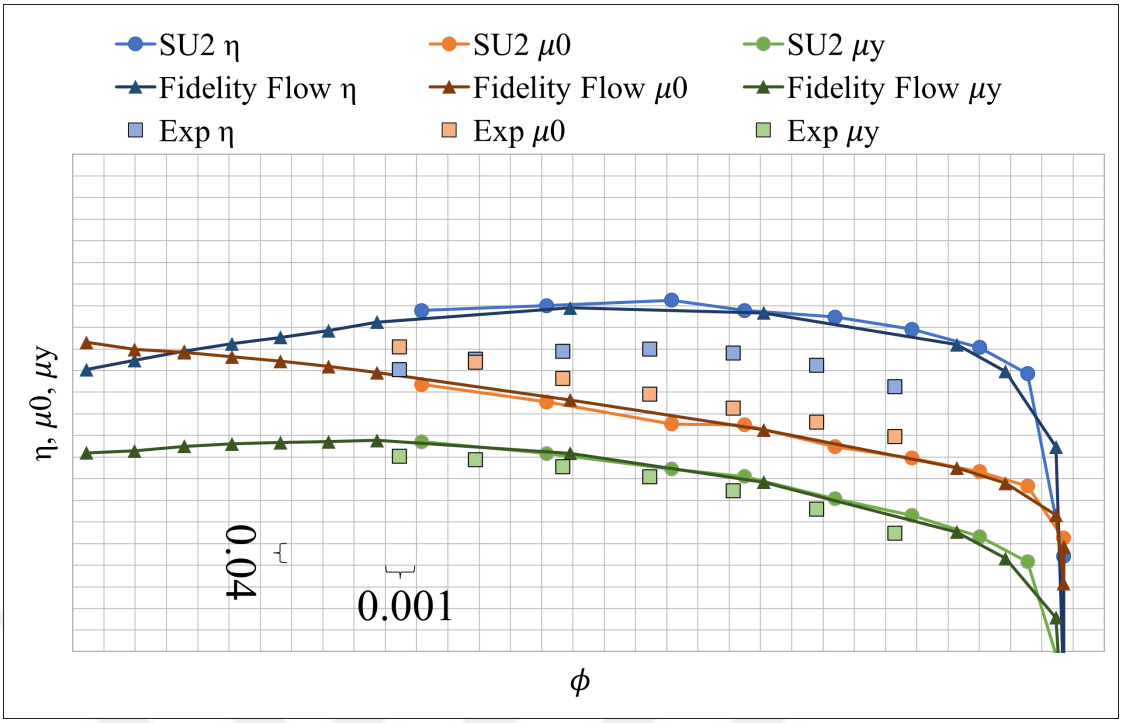

Figure 28: η, μ_y, and μ_0 vs ϕ for Case#1

having a mass flow rate boundary condition for the outlet.

Pressure contours at impeller and vane blades leading and trailing edges of two operating points with low and high polytropic efficiencies are shown in Appendix B.

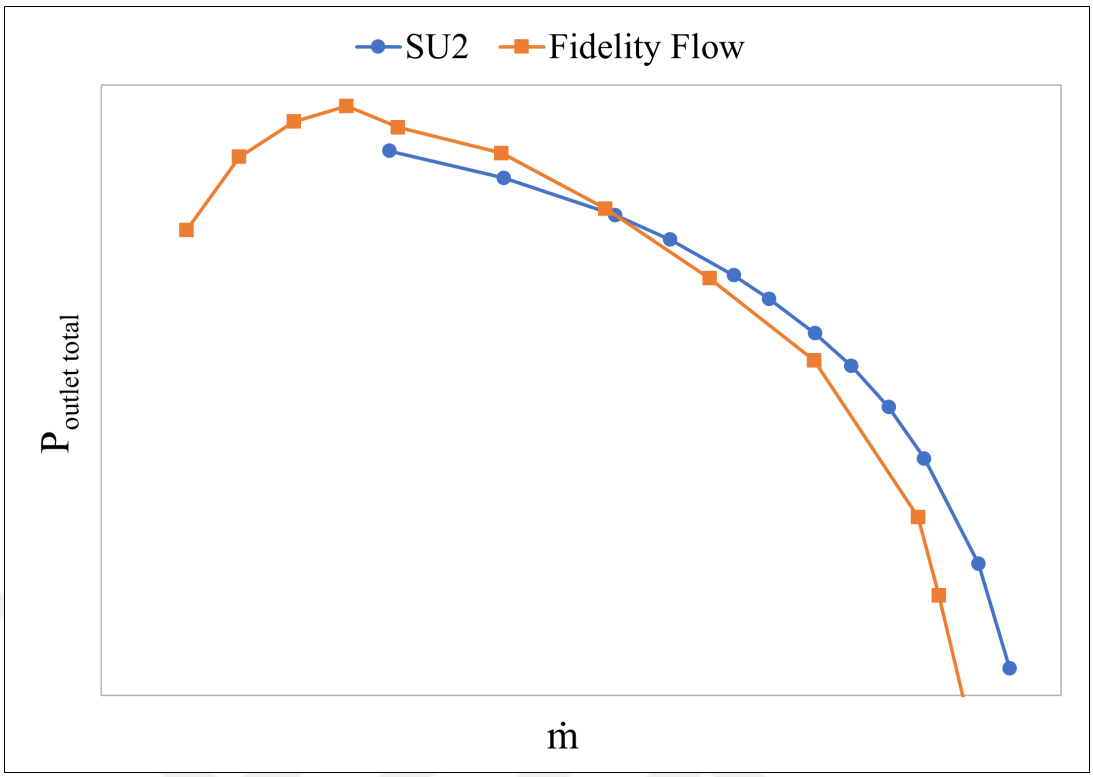

Figure 29: $P_{outlet_{total}}$ vs $\dot{m}$ for Case#2

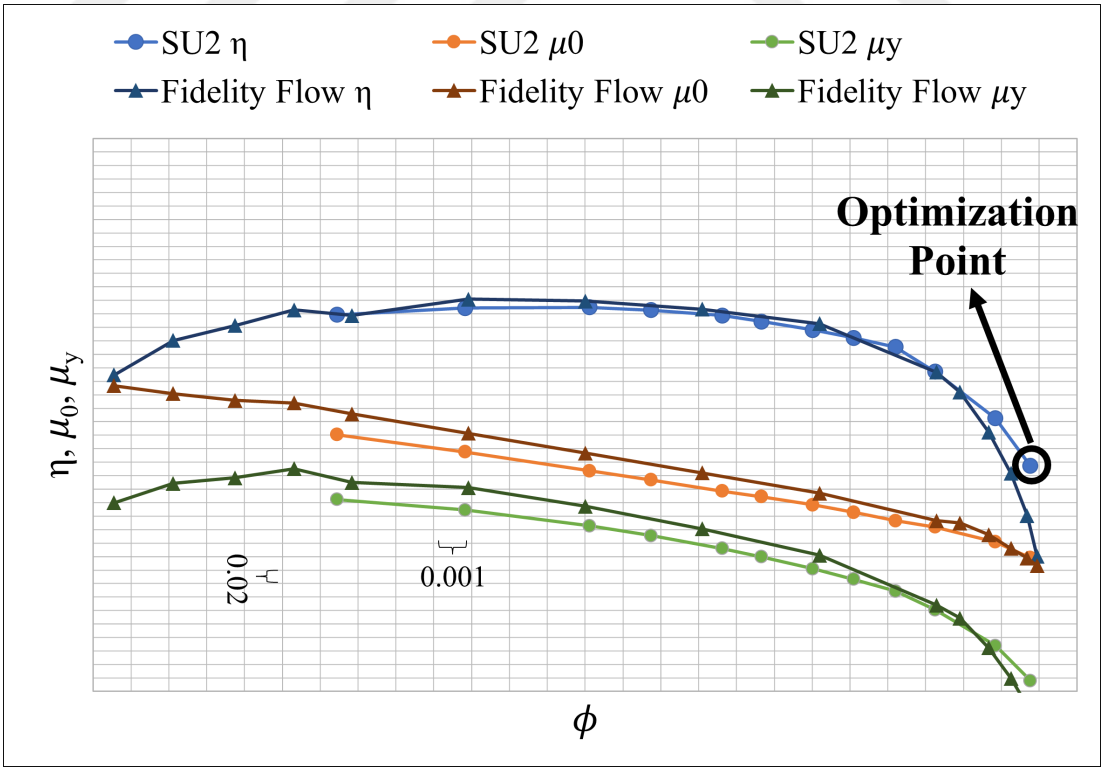

Figure 30: η, μ_y, and μ_0 vs ϕ for Case#2

CHAPTER VIII

DIFFUSER VANE SHAPE OPTIMIZATION

Design capabilities of SU2 are also tested. SU2 comes with shape optimization tools of its own implemented in it. In this regard, vane geometry from the vaned diffuser case is worked. The initial design is taken as baseline and 2D optimization of the profile of the vane is done. Performance improvements over the baseline design are showed.

8.1 Methodology

Adjoint methods are very common for shape optimization studies. Adjoint methods in computational fluid dynamics are first introduced by Jameson [53]. Adjoint equations are derived from the governing equations. Adjoint method changes depending on derivation of the adjoint equations before or after the discretization of the governing equations [54]. If adjoint equations are derived after the discretization of governing equations, it is called *Discrete Adjoint Method*. If adjoint equations are derived before the discretization of governing equations, it is called *Continuous Adjoint Method*. Discrete Adjoint is used for the optimization study.

SU2 has built in optimization tools out of the box. The capabilities of these tools are investigated with the vane of Case#2 shown in Figure 19. The original geometry is in 3D. However, diffuser vane is a prismatic blade. This means that the profile of the vane does not change in the spanwise direction. Also, the total pressure changes in the spanwise direction are around 1% when compared to the total pressure average of the whole diffuser inlet, except near the hub side. Near the hub side there is a region where relatively higher total pressure is seen, which increases the average total pressure around that spanwise location. It can be seen in the Figure 31. Even though near the hub side the total pressure difference from whole diffuser inlet average is higher compared to other spanwise locations,

for a more general approach, using the total pressure average from the whole diffuser inlet is more favorable since other spanwise locations have very similar total pressure averages. The flow field comparison of 2D result obtained by using averaged inlet conditions and mide-span slice of the 3D result is shown in Figure 32. As it can be seen from Figure 32, the flow fields are almost identical. Therefore, it can be said that a 2D approach for the problem is possible, and to simplify the optimization problem, the vane blade profile is optimized in 2D.

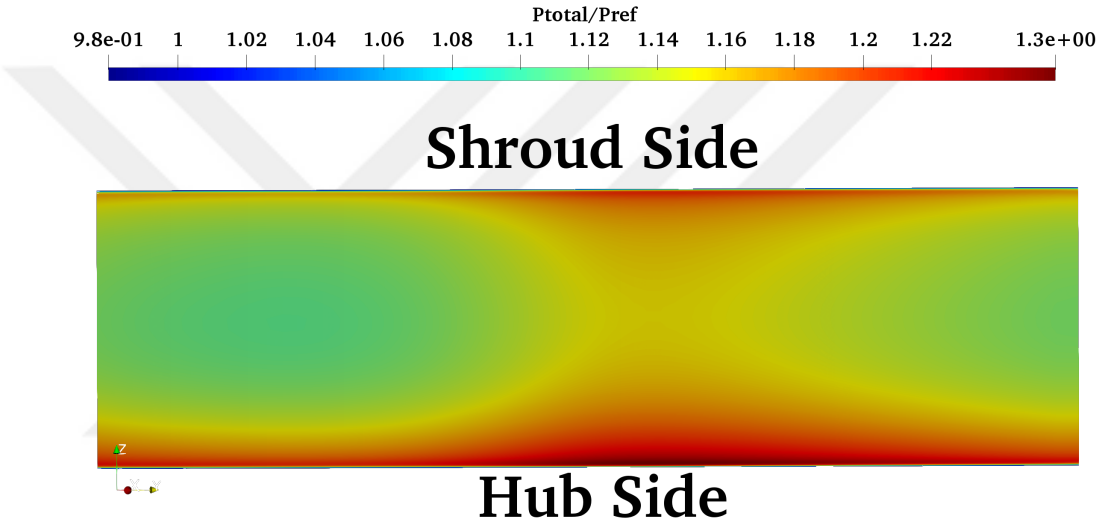

Figure 31: P_{tot}/P_{ref} at the Diffuser Inlet for Case#2

There are two types of design variable definition for 2D optimization in SU2. These are Hicks-Henne [55] and Free-form Deformation (FFD) [56][57]. When using Hicks-Henne, it is only possible to define variables for upper, lower or whole surface. However, with FFD it is possible to define design variables in interested parts of the surface. In order to achieve this, FFD requires user to enclose the parts that will be subjected to optimization in a box. It uses this box to define design variables, and shape deformation is done only in this box. Also, Hicks-Henne is only available for 2D geometries while FFD is available in both 2D and 3D. Therefore, due to its greater potential in possible further investigations, FFD

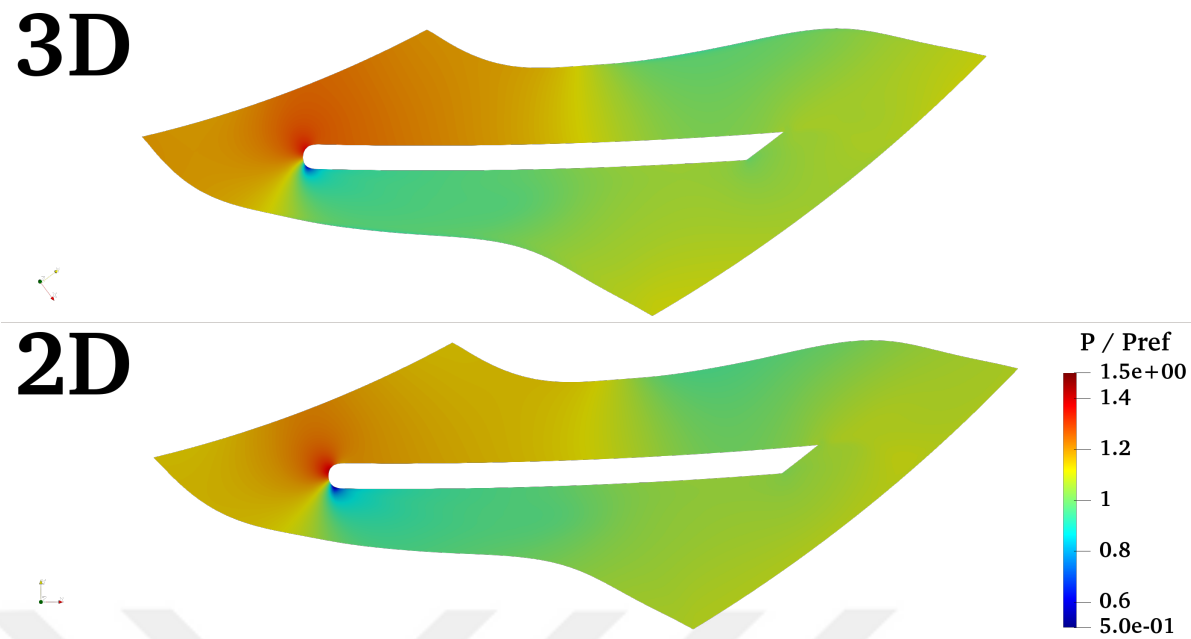

Figure 32: 2D vs 3D P_{tot}/P_{ref} at the Diffuser for Case#2

method is chosen for the definition of the design variables. The way FFD box has to be defined is shown in Figure 33. The numbers in Figure 33 represent in which order the points are needed for the definition of the FFD box in SU2. The sides of FFD box are split into several pieces by the user. The nodes inside this FFD box are the points where the design variables are evaluated For FFD,

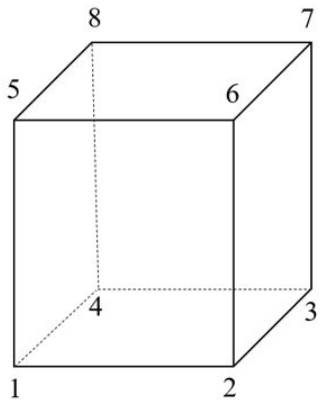

Figure 33: FFD Box Points Ordering

different types of design variable definitions are available in SU2. Through trial and error, "FFD_THICKNESS_2D" and "FFD_CAMBER_2D" are selected. With

"FFD_THICKNESS_2D" selected, shape deformation is done by changing the thickness of the surface objected to optimization, and with "FFD_CAMBER_2D", shape deformation is done by changing the camber of the surface objected to optimization at the nodes of the FFD box.

In terms of objective and constraint functions, drag and total pressure are used. Drag is given as a constraint function to limit the shape changes, so that sudden big changes to the geometry are prevented. For this, a positive drag, $DRAG > 0$, is used as the constraint for the shape optimization. Total pressure at the outlet is given as the objective function. The maximization of outlet total pressure is used as the objective. The main idea behind selecting objective and constraint functions is preventing losses. If the total pressure at the outlet can be increased without changing the blade profile too dramatically, the shape optimization would be considered successful.

Optimization is done for only one point, and this point is the operating point with the worst performance. This operating point is also shown in Figure 30. Since only one operating point is used for the optimization, major changes are avoided.

Two different FFD boxes are used for the shape deformations. First FFD box covered only the part with a strong flow separation at the suction side of the blade, whereas the other FFD box covered the whole blade. The latter approach was to see how would the performance change if SU2 is let free to optimize the whole blade for that operating point. These boxes are used individually for each test, they are not combined.

8.2 Optimization Results

The boundary conditions for the diffuser vane optimization study are taken from the operating point where the lowest η is seen for Case#2, also shown in Figure 30. Since the original geometry is in 3D, averaged values are used for the 2D optimization. The conditions taken from original geometry are total pressure and

temperature, and flow direction for the inlet, and static pressure for the outlet.

The initial location selected for the optimization is where a reverse flow region is seen at the suction side of the diffuser vane blade. Using the streamlines, reverse flow region at the suction is shown in Figure 34 with blue streamlines. The design variable option selected for this optimization is "FFD_CAMBER_2D".

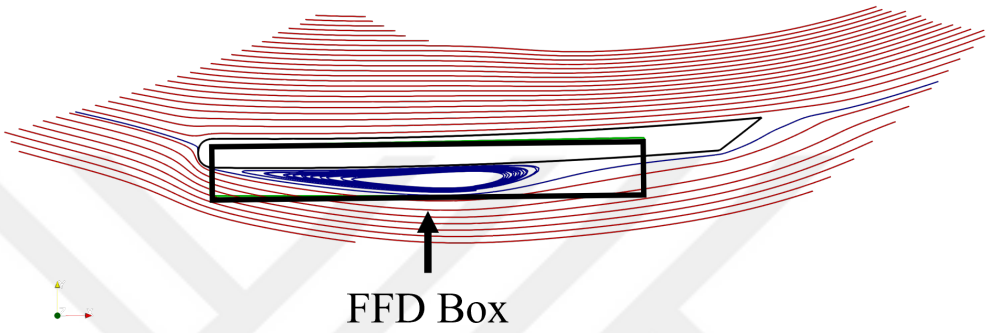

Figure 34: Streamlines around the Diffuser Vane with Reverse Flow Region (Blue), FFD Box and the Blade Surface

It took SU2 20 design iterations to reach the optimized solution. As a result of the optimization, the reverse flow region is reduced by 4.87%, while the total pressure loss between diffuser inlet and outlet is reduced by 0.55%. Considering that only a small portion of the geometry was subjected to optimization, this kind of improvement is to be expected. The change of drag and total pressure difference between diffuser inlet and outlet with each design iteration are shown in Figures 35 and 36, respectively. The close up of initial and optimized blade geometries are shown in Figure 37. The jump at Design Iteration 10 seen in Figures 35 and 36 are due to the shape deformation SU2 imposed at that design iteration. The close-up of the change in blade surface is shown in Figure 38. As it can be seen from Figure 38, SU2 changes the blade shape back near to where it was previously as design iterations continue, and the shape that was reached at Design Iteration 9 is very much similar to the Design Iteration 20, which is the final optimized

design.

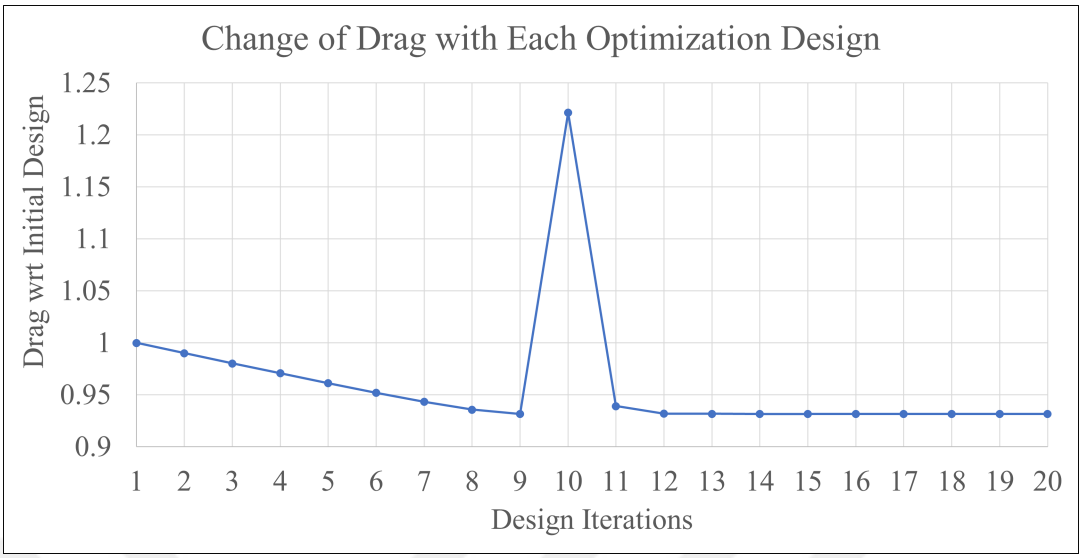

Figure 35: Change of Drag with Each Optimization Design

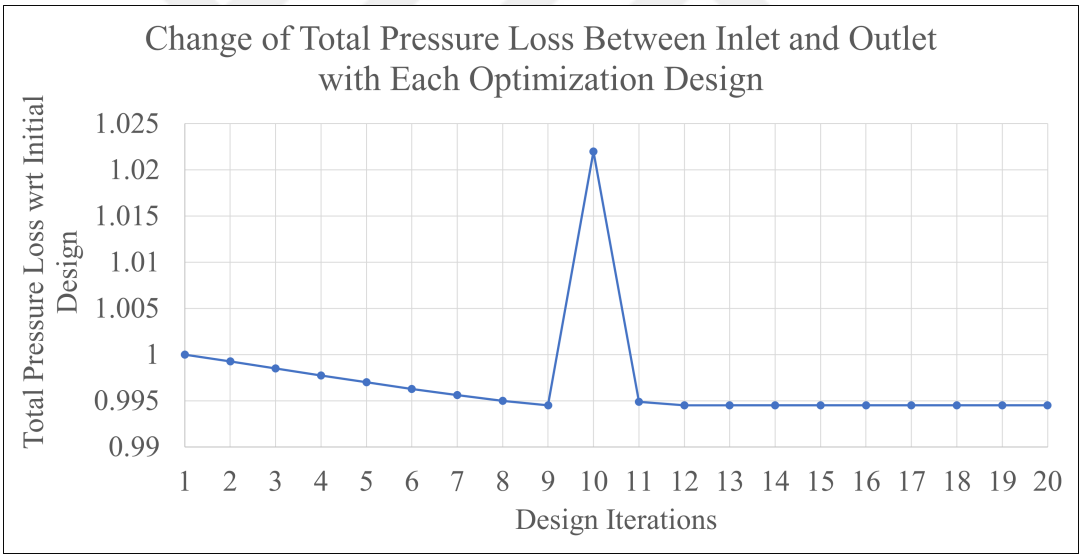

Figure 36: Change of Total Pressure Loss Between Diffuser Inlet and Outlet Each Optimization Design

The comparison of the reverse flow region between the initial and optimized geometries are shown in Figure 39 with the streamlines that roughly give the border of the separated region. The most difference between reverse flow regions are seen near the leading edge where the reverse flow region starts. By a small deformation, SU2 carried the start of the reverse flow region downstream. There

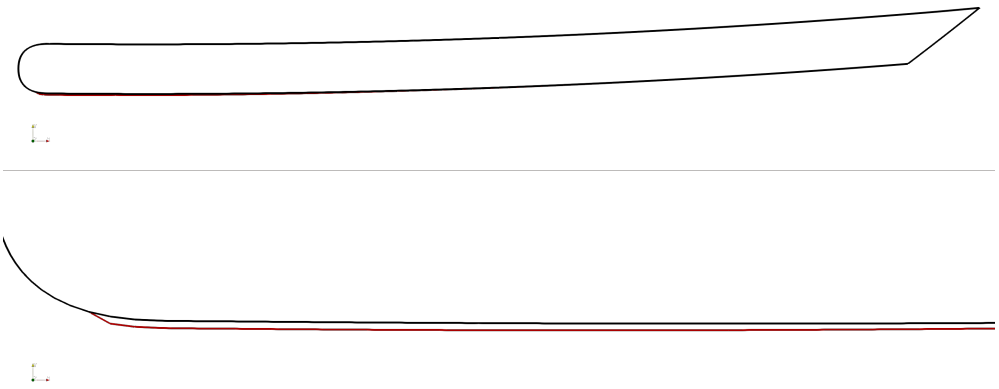

Figure 37: Initial (Black) and Optimized (Red) Blades Surfaces with a Close-up of the Most Deformed Area Shown Below

is no significant change between reverse flow regions for initial and optimized geometries after the thickest section of the initial reverse flow region.

SU2 improved the given objective parameter at the optimization point. However, since the optimization is done only using a single operating point, the performance at other operating points needs to be tested. For this, the operating point with the highest η shown in Figure 30 is selected. When the optimized geometry obtained here is used with boundary conditions obtained from this operating point, even though the outlet total pressure decrease was very small, total pressure loss was increased by 0.86%. This shows the need of a multi-point optimization for a design aimed to work at an interval of operating points in order to achieve a more general optimization.

8.3 Optimization Study with the Whole Blade Submerged in the FFD Box

Another optimization case where the whole of the diffuser vane blade is put in the FFD box and subjected to optimization while using the same boundary conditions is conducted as well. The design variable option selected for this optimization is "FFD_THICKNESS_2D". In this case, SU2 optimized the blade to have a better incidence angle for the operating point used as boundary condition and eliminated

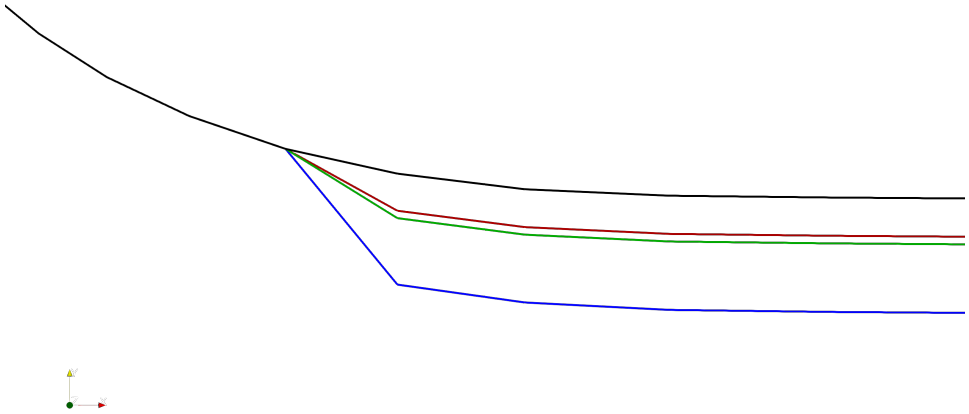

Figure 38: Initial (Black), Design Iterations 9 (Red), 10 (Blue) and 11 (Green) Blades Surface Close-ups of the Most Deformed Area

the reversed flow region shown in Figure 34 completely. The outlet total pressure is increased by 2.44% as the result of this optimization. However, SU2 was only able to do 3 design iterations before deforming the blade to the point where it can not acquire a direct solution on the deformed mesh. Therefore, it is hard to say that the optimization process for this case is reached the optimal blade shape even though the improvement in outlet total pressure is very significant. The comparison of profiles near leading edge and incidences of initial and optimized blade are shown in Figures 40 and 41, respectively.

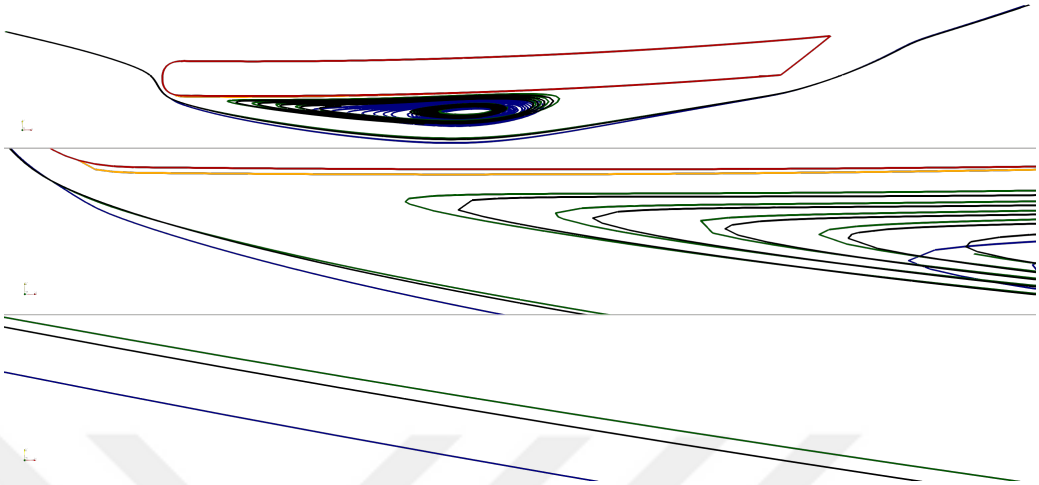

Figure 39: Reversed Flow Regions Border Streamlines for Initial (Black), Optimized (Green) and Design Iteration 10 (Blue) with Baseline (Red) and Optimized (Orange) Diffuser Vane Blades

Figure 40: Leading Edge Close-up of Initial (Green) and Optimized (Red) Diffuser Vane Blades for the Optimization with Whole Blade Submerged in the FFD Box

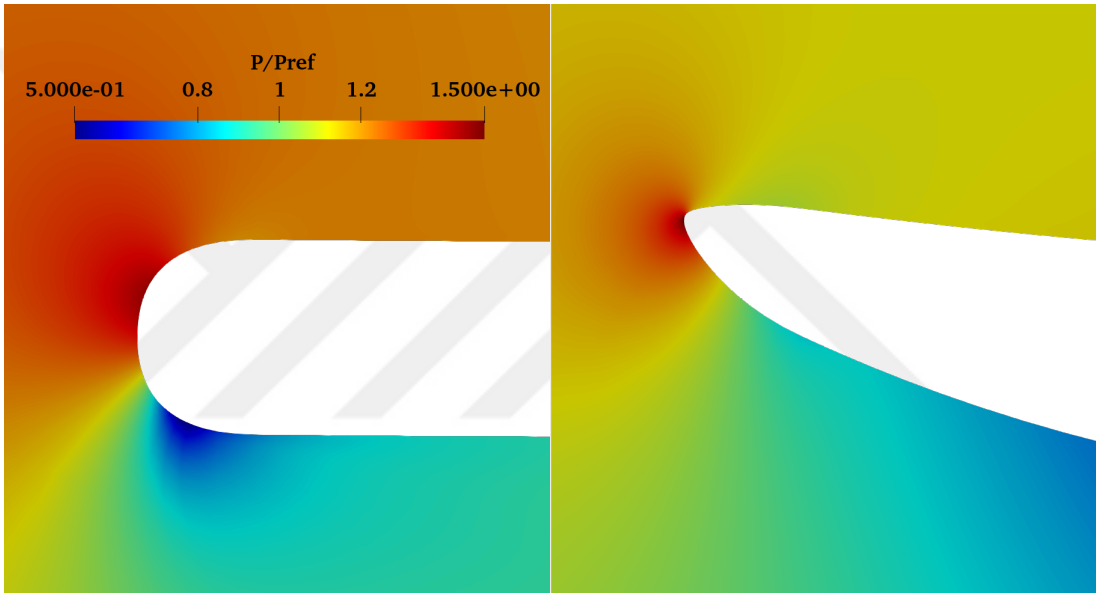

Figure 41: Incidence of Initial (Left) and Optimized (Right) Diffuser Vane Blades for the Optimization with Whole Blade Submerged in the FFD Box

CHAPTER IX

CONCLUSION

The usage of open-source CFD tools for turbomachinery applications is investigated through SU2 in this work. The examination is done via two 3D radial compressor geometries with vaneless and vaned diffusers.

A methodology is first developed for turbomachinery steady state simulations in SU2. The results obtained with the developed methodology using SU2 are compared to commercial software Fidelity FLow and ANSYS-CFX. In these comparisons, SU2 showed great potential.

Moreover, the optimization capabilities of SU2 are also examined for a turbomachinery application. For this, the vane of the vaned diffuser geometry is used. Since the geometry of the vane does not show any change in one direction, it is simplified to a 2D geometry for a less complex optimization study. Two different scenarios are followed for the optimization study, and outlet total pressure is selected as the aspect to be improved. The operating point with the worst performance is selected for the optimization study.

In the first optimization scenario, only a portion at the suction side of the blade is subjected to optimization. As a result of this optimization, some improvement is achieved, but due to the portion of the blade subjected to shape deformation being very limited, the decrease in total pressure loss was somewhat small. However, at a different operating point, optimized design performed worse compared to the baseline. In the end it is not possible to say that an optimized design is reached to work at all of the operating points.

In the second optimization scenario, whole blade is subjected to shape deformation. As a result, the increase in the outlet total pressure was way higher

compared to first optimization scenario and very significant. However, the optimization process was unable to continue without deforming the blade shape too much. Therefore, it is difficult to say that an optimized blade shape is reached. Also, due to using only one operating point for the optimization process, SU2 deformed the blade incidence angle to perform better at that operating point, which is not a desired outcome since the blade has to operate in an interval of operating points.

There are several downsides of SU2 that are discovered throughout this study.

- The most crucial one for the turbomachinery applications was the lack of mass flow outlet boundary condition. Due to this, it was not possible to simulate some operating points in the operating range of the compressors used.

- The calculation of abnormal temperature and density values at the trailing edge of the cut-back type impeller blade prevented the usage of higher order numerical schemes in the simulations. This issue was posted to the official GitHub page of SU2, although it did not find a solution[1].

- SU2 would calculate faulty mass flow rates at arbitrarily shaped surfaces/interfaces. However, this would not effect the actual solution, which suggests that the issue is related only to the output rather than the values used in the calculations.

- Most of the objective/constraint functions listed in the SU2's setting did not work out of the box. The only two objective/constraint functions working were drag and lift. In order to make total pressure functional as an objective function for the outlet as it is explained in this work, some minor changes in the code had to be made, which only included some name changes for the recognition of the objective/constraint functions.

[1] https://github.com/su2code/SU2/issues/1337

There are some issues that were experienced and was fixed in this study as well.

- An issue related to the parallelization of turbomachinery cases in SU2 was experienced. In its subroutine before the simulation, SU2 would calculate faulty numbers of spanwise points when it is run in parallel mode above some number of cores. This was an old issue that was reported before[2] as well but was still apparent during this work. To avoid this, a crude fix was implemented by hardcoding the number of points in spanwise direction for inlet and outlet. Later on, a fix that solved this issue is published[3] by SU2 developers that cleared away the need of hard coding number of points in spanwise directions and compiling the whole code again every time the mesh is changed.

- Using periodic faces with a 2D mesh would generate faulty results. This issue was first experienced during the trials for 2D optimization study for the diffuser vane blade. It was reported together with the help of a colleague[4] and was fixed later on[5].

SU2 is a very strong CFD and design suite that has a great potential to grow. There is a growing community of active users and developers, which contribute more and more to SU2 by finding and/or fixing the issues as it is shown with examples above. The great part of being an open-source project is that it will always keep growing as it gains more and more popularity. In regards to turbomachinery, even with its downsides explained here, SU2 is proved itself to be a worthy alternative for commercial tools.

[2]https://github.com/su2code/SU2/issues/990
[3]https://github.com/su2code/SU2/pull/1221
[4]https://github.com/su2code/SU2/issues/1562
[5]https://github.com/su2code/SU2/pull/1563

APPENDIX A

CONTOURS FOR CASE#1

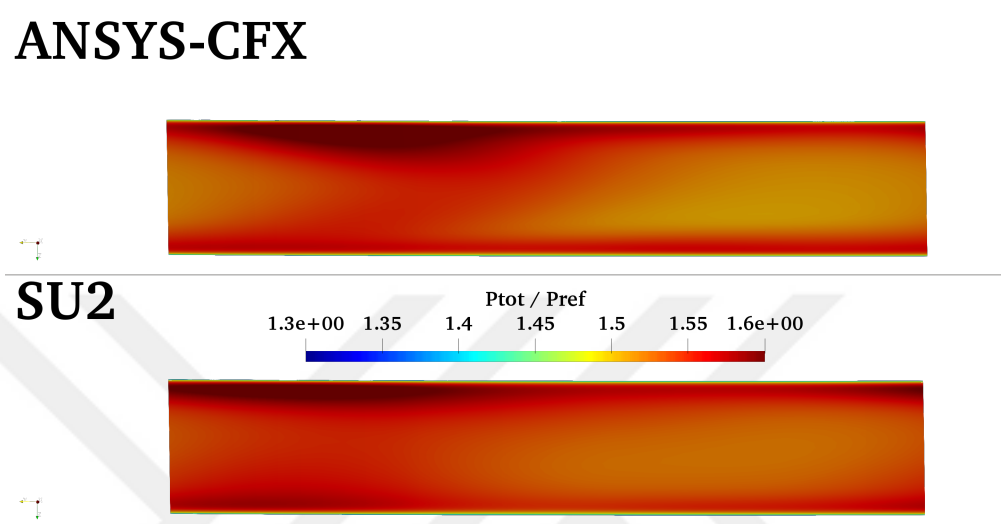

Figure 42: $\frac{P_{tot}}{P_{tot_{ref}}}$ at the Comparison Station r1 for Case#1 at a Lower η - SU2 vs ANSYS-CFX

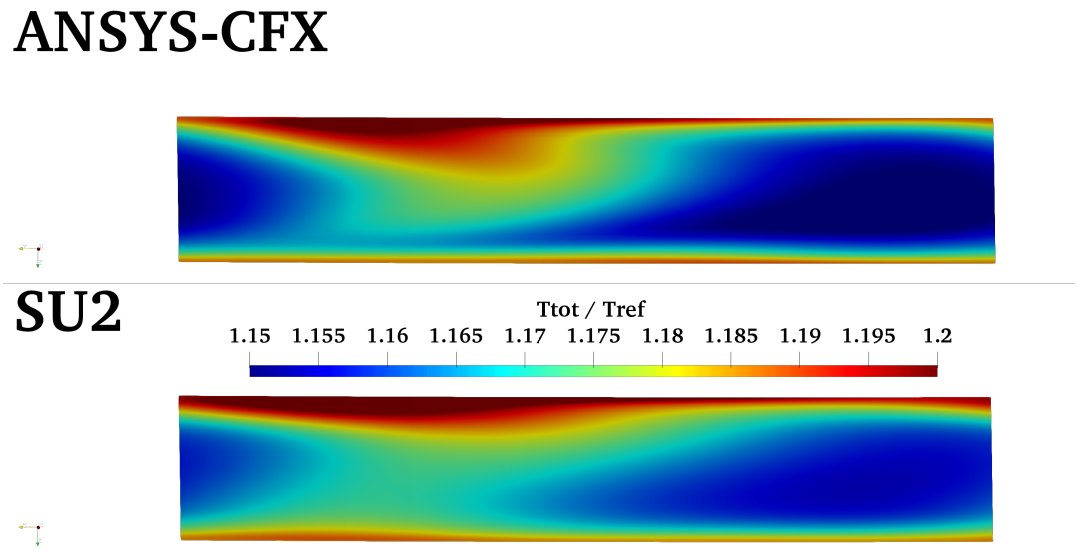

Figure 43: $\frac{T_{tot}}{T_{tot_{ref}}}$ at the Comparison Station r1 for Case#1 at a Lower η - SU2 vs ANSYS-CFX

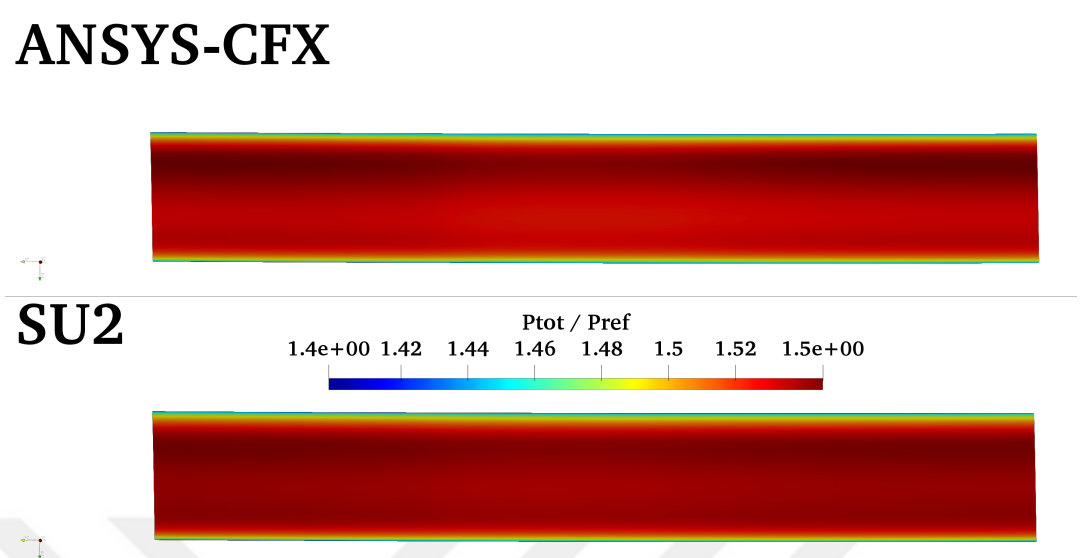

Figure 44: $\frac{P_{tot}}{P_{tot_{ref}}}$ at the Comparison Station r2 for Case#1 at a Lower η - SU2 vs ANSYS-CFX

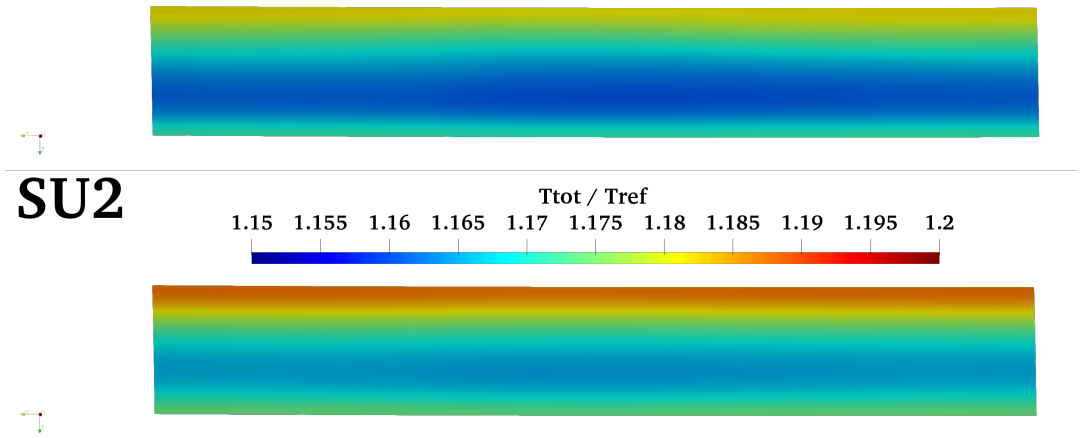

Figure 45: $\frac{T_{tot}}{T_{tot_{ref}}}$ at the Comparison Station r2 for Case#1 at a Lower η - SU2 vs ANSYS-CFX

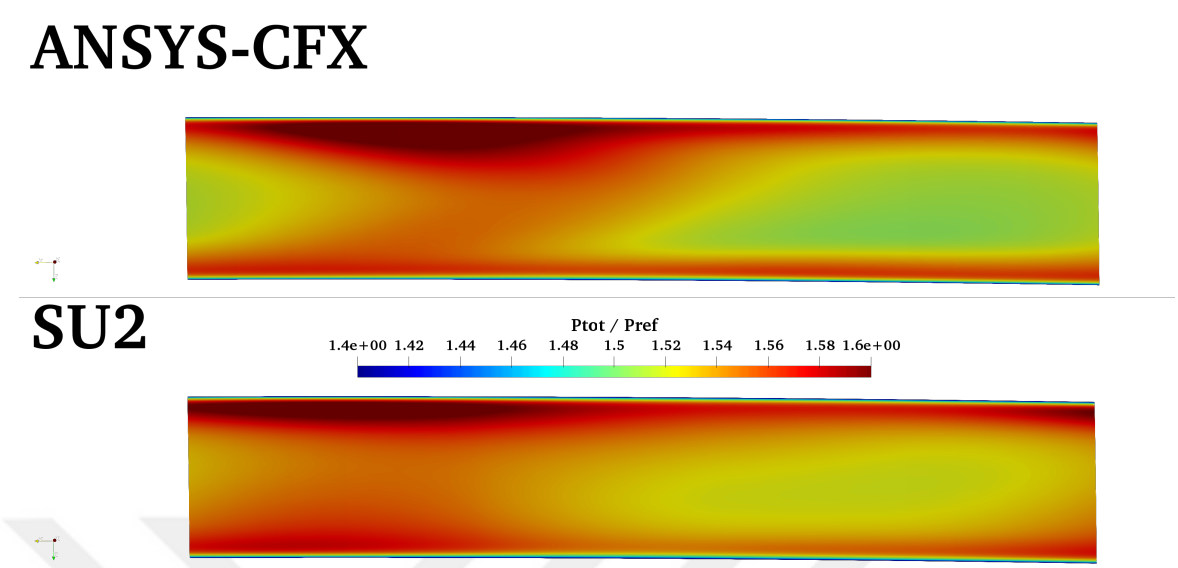

Figure 46: $\frac{P_{tot}}{P_{tot_{ref}}}$ at the Comparison Station r1 for Case#1 at a Higher η - SU2 vs ANSYS-CFX

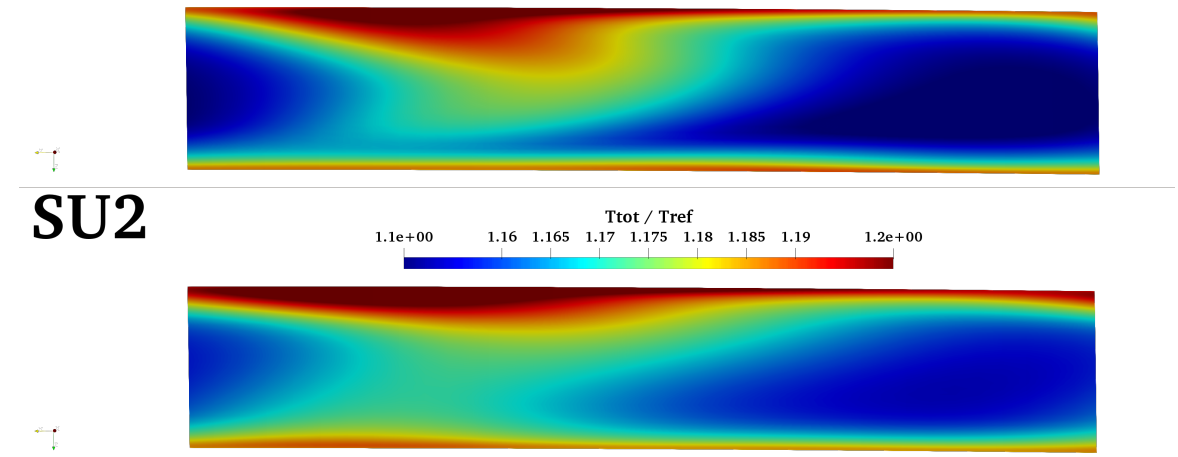

Figure 47: $\frac{T_{tot}}{T_{tot_{ref}}}$ at the Comparison Station r1 for Case#1 at a Higher η - SU2 vs ANSYS-CFX

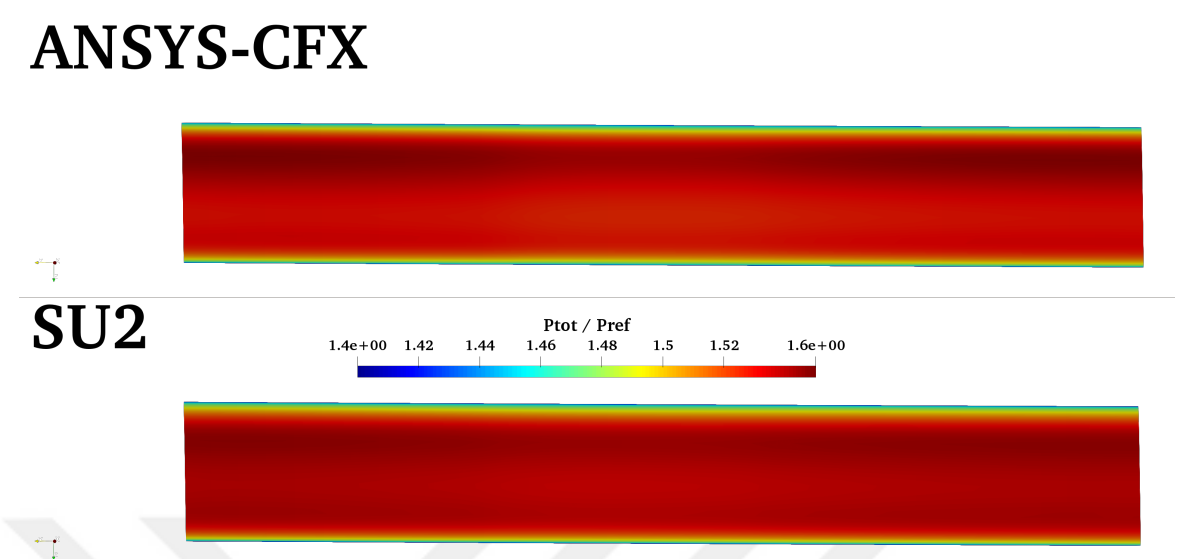

Figure 48: $\frac{P_{tot}}{P_{tot_{ref}}}$ at the Comparison Station r2 for Case#1 at a Higher η - SU2 vs ANSYS-CFX

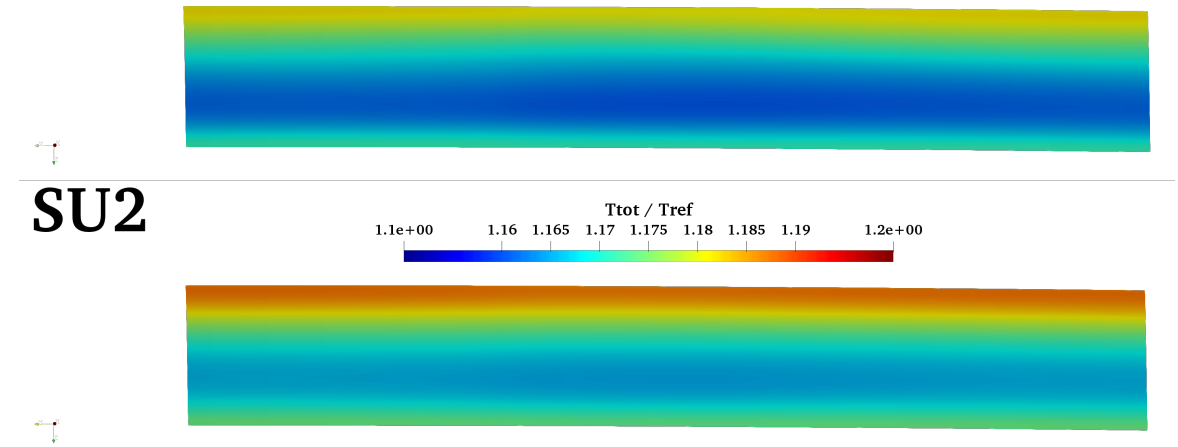

Figure 49: $\frac{T_{tot}}{T_{tot_{ref}}}$ at the Comparison Station r2 for Case#1 at a Higher η - SU2 vs ANSYS-CFX

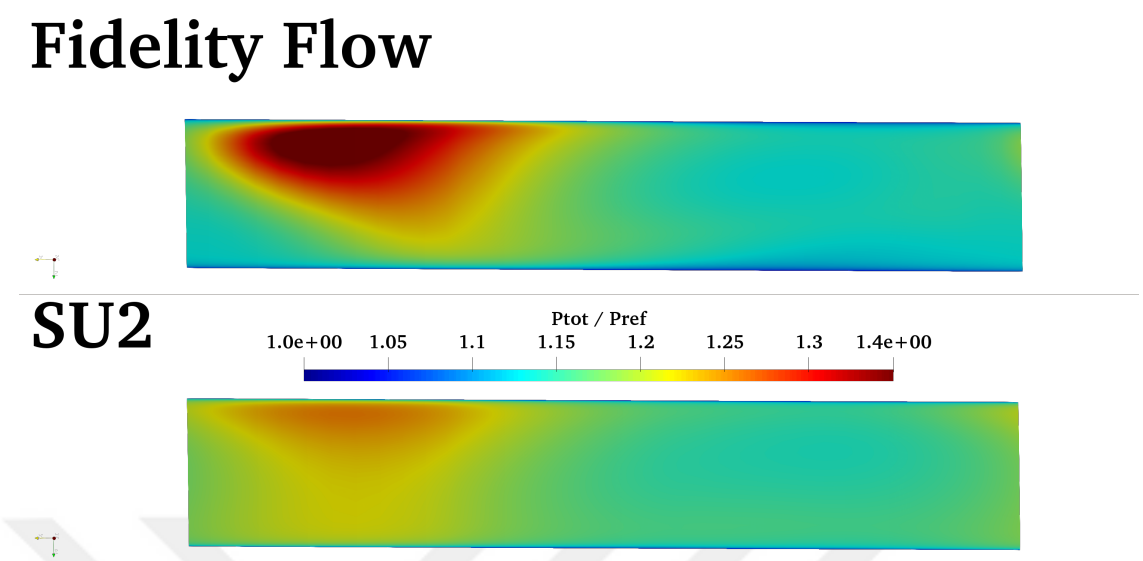

Figure 50: $\frac{P_{tot}}{P_{tot_{ref}}}$ at the Comparison Station r1 for Case#1 at a Lower η - SU2 vs Fidelity Flow

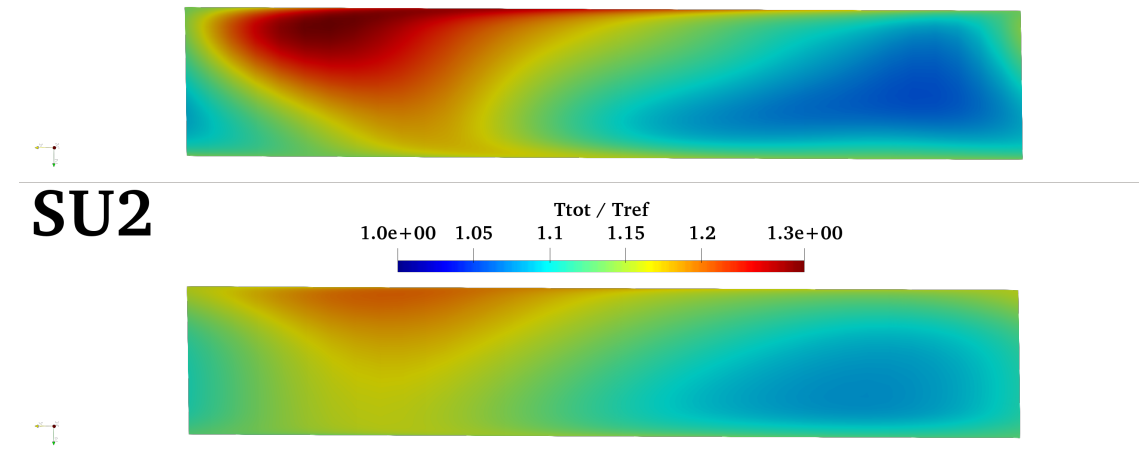

Figure 51: $\frac{T_{tot}}{T_{tot_{ref}}}$ at the Comparison Station r1 for Case#1 at a Lower η - SU2 vs Fidelity Flow

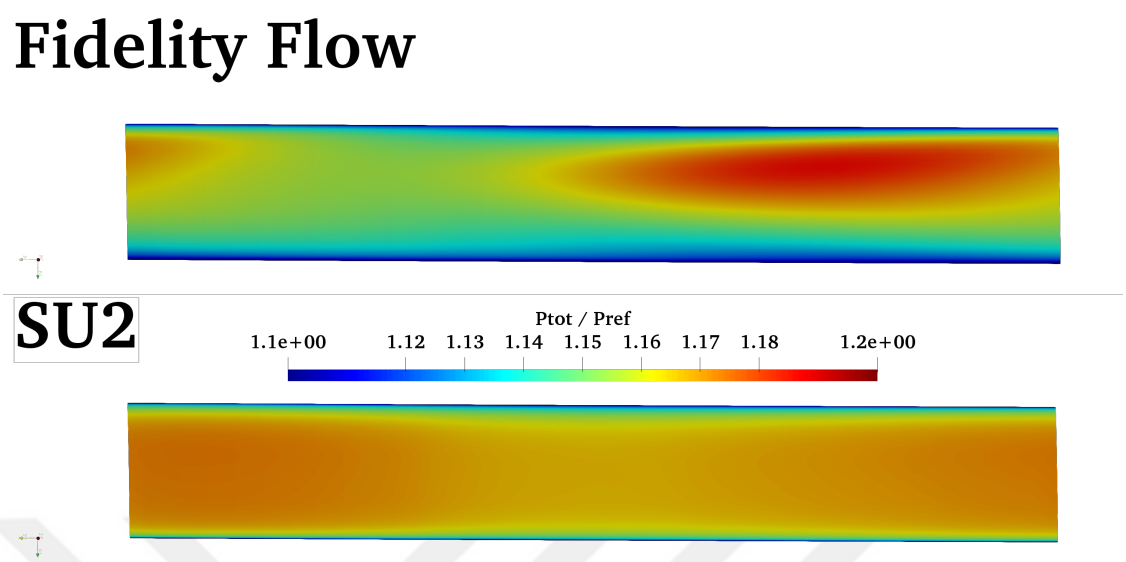

Figure 52: $\frac{P_{tot}}{P_{tot_{ref}}}$ at the Comparison Station r2 for Case#1 at a Lower η - SU2 vs Fidelity Flow

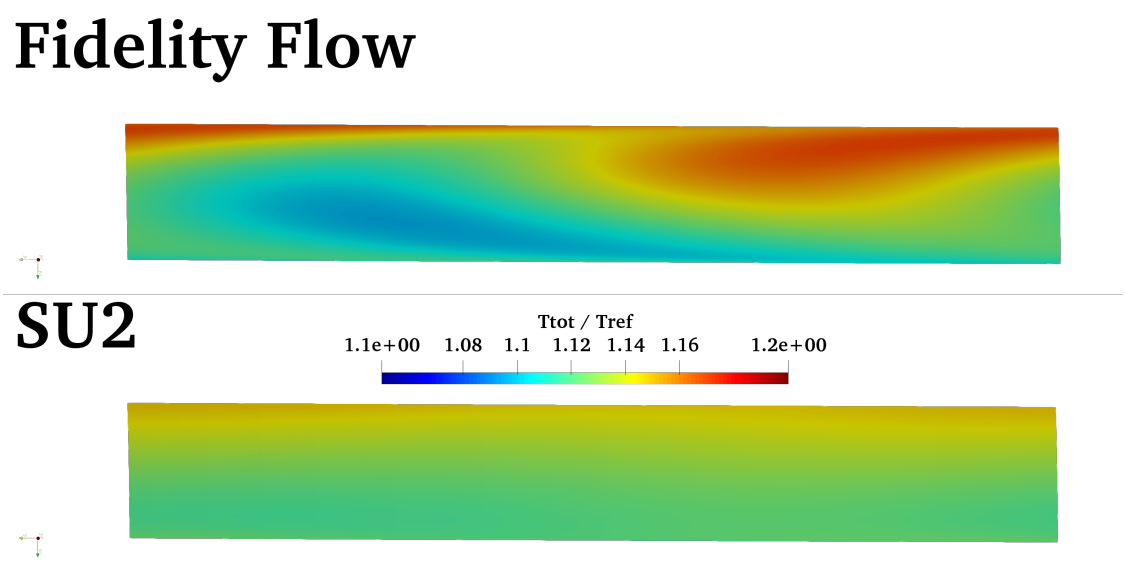

Figure 53: $\frac{T_{tot}}{T_{tot_{ref}}}$ at the Comparison Station r2 for Case#1 at a Lower η - SU2 vs Fidelity Flow

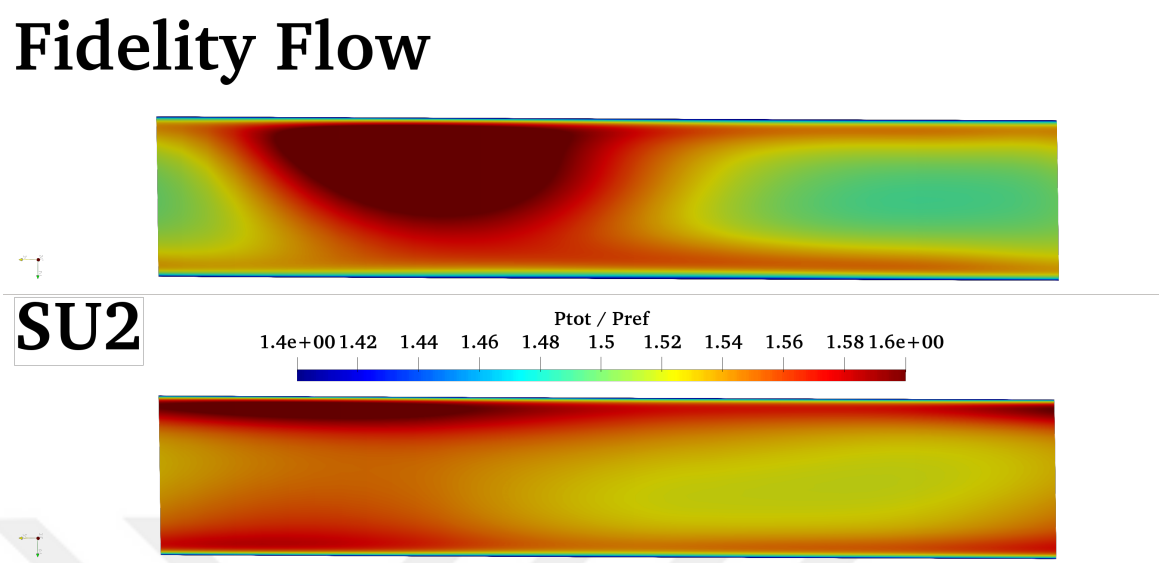

Figure 54: $\frac{P_{tot}}{P_{tot_{ref}}}$ at the Comparison Station r1 for Case#1 at a Higher η - SU2 vs Fidelity Flow

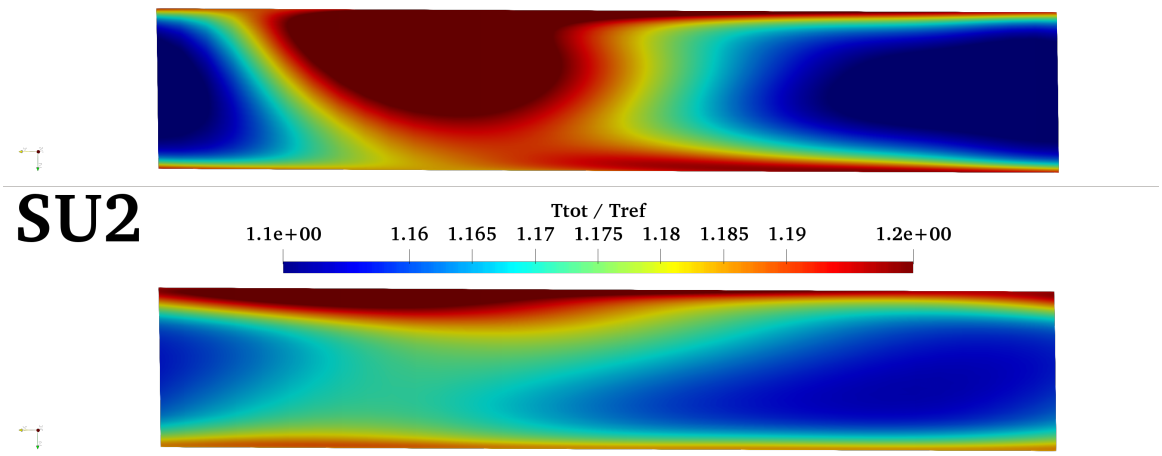

Figure 55: $\frac{T_{tot}}{T_{tot_{ref}}}$ at the Comparison Station r1 for Case#1 at a Higher η - SU2 vs Fidelity Flow

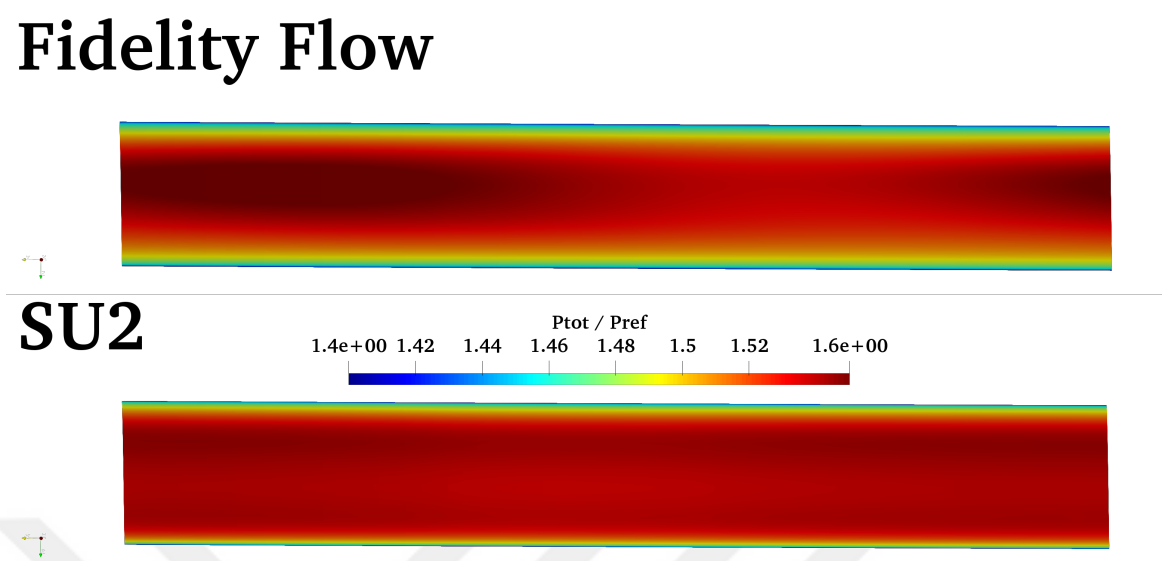

Figure 56: $\frac{P_{tot}}{P_{tot_{ref}}}$ at the Comparison Station r2 for Case#1 at a Higher η - SU2 vs Fidelity Flow

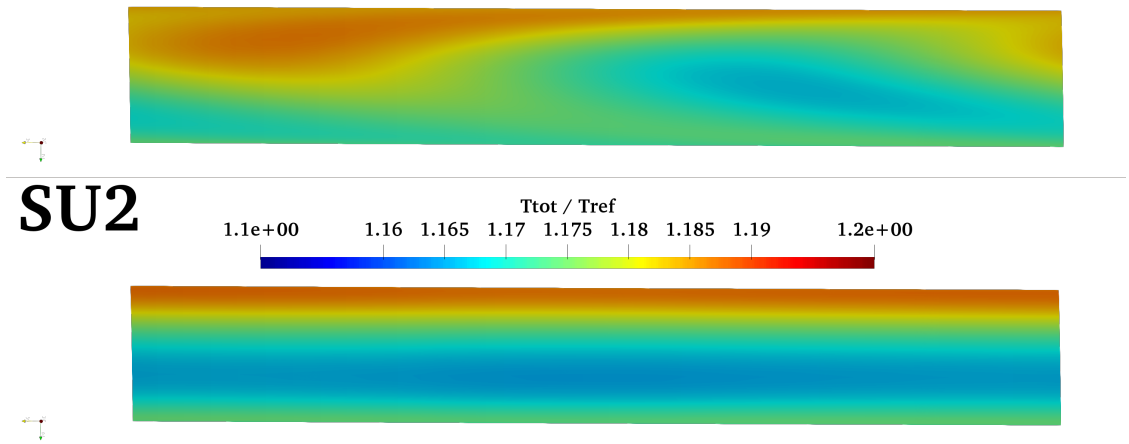

Figure 57: $\frac{T_{tot}}{T_{tot_{ref}}}$ at the Comparison Station r2 for Case#1 at a Higher η - SU2 vs Fidelity Flow

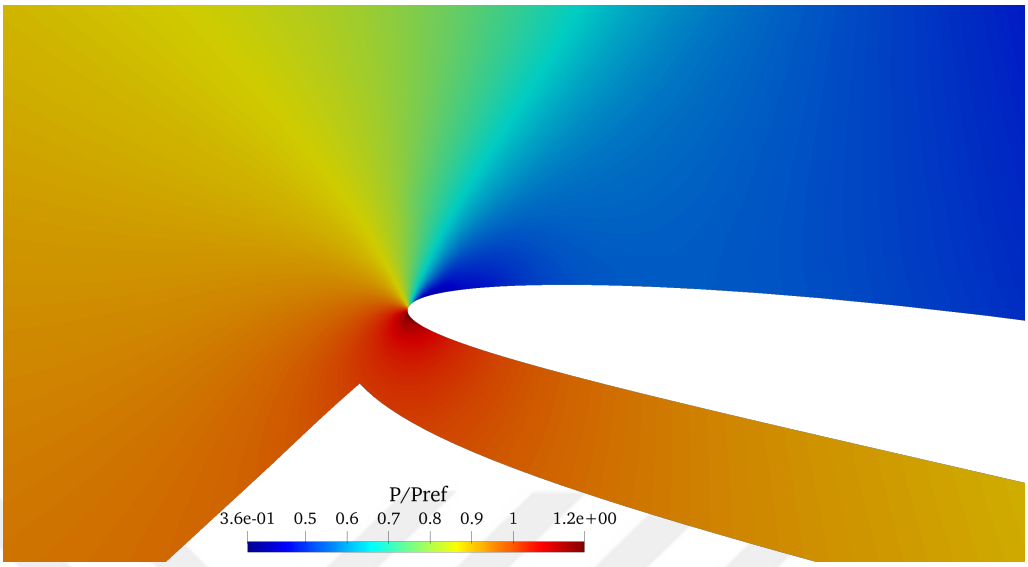

Figure 58: $\frac{P}{P_{ref}}$ Around Leading Edge for Case#1 at a Lower η

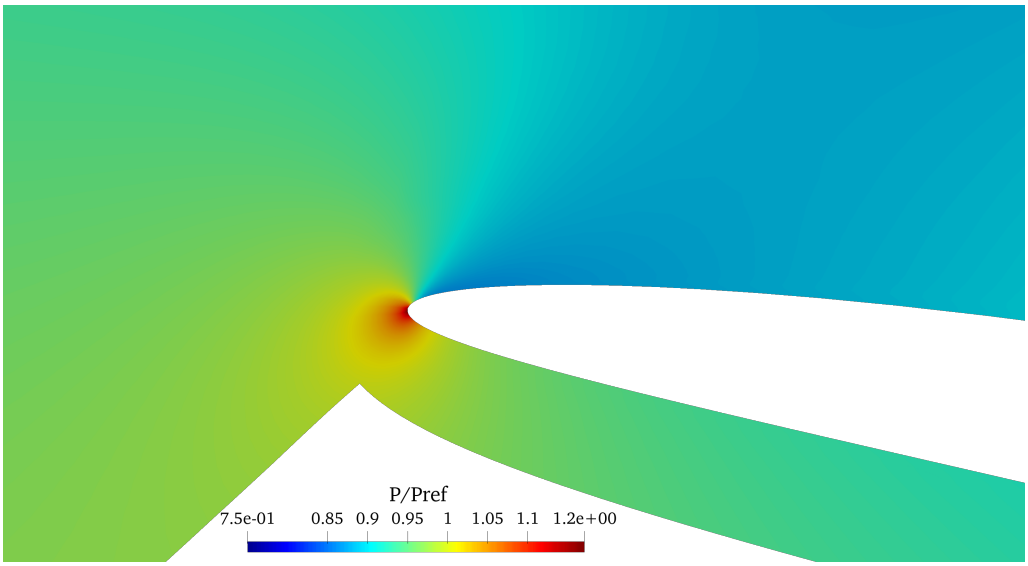

Figure 59: $\frac{P}{P_{ref}}$ Around Leading Edge for Case#1 at a Higher η

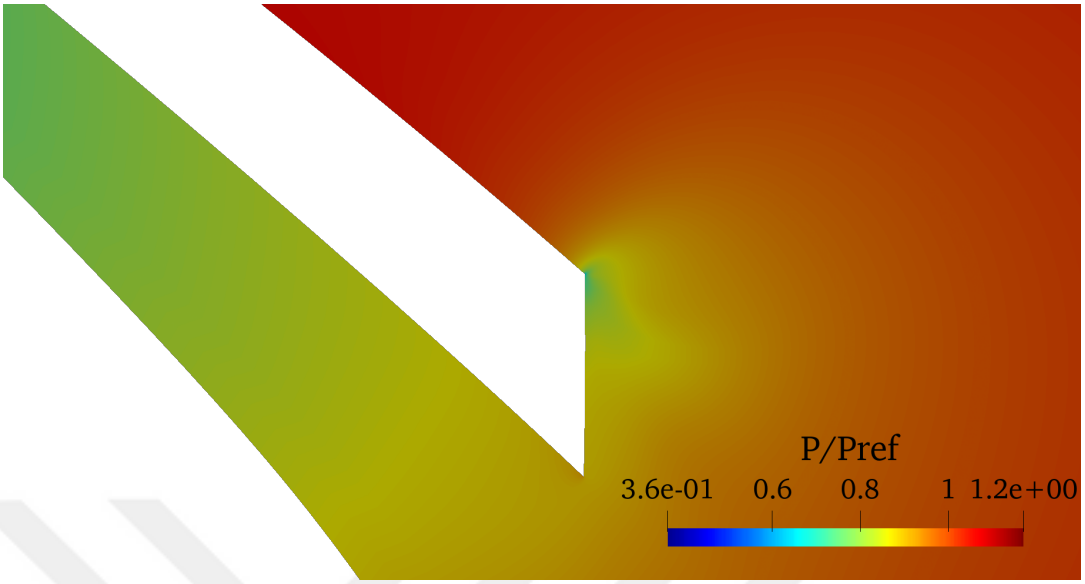

Figure 60: $\frac{P}{P_{ref}}$ Around Trailing Edge for Case#1 at a Lower η

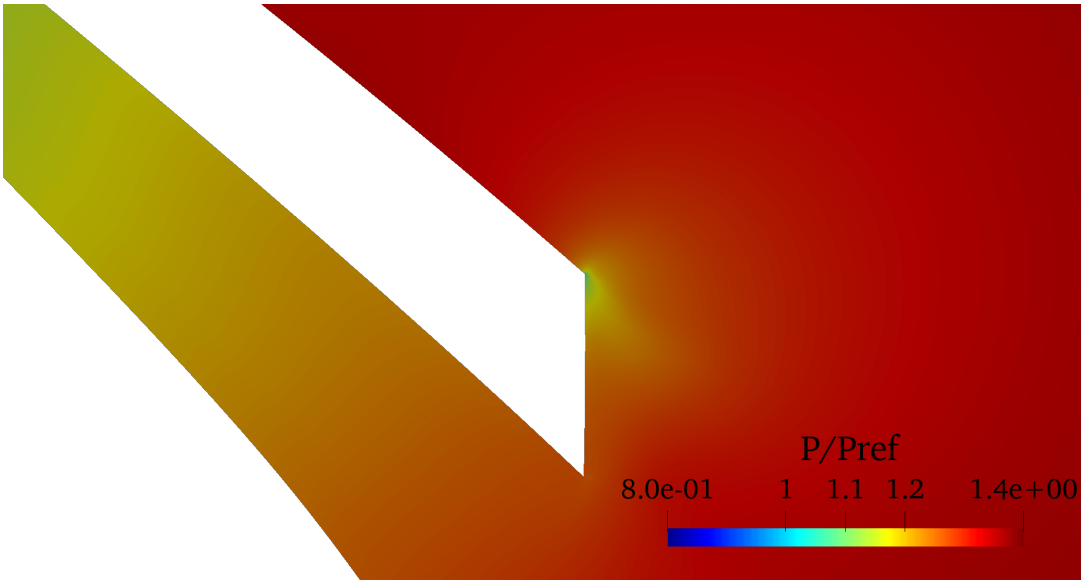

Figure 61: $\frac{P}{P_{ref}}$ Around Trailing Edge for Case#1 at a Higher η

APPENDIX B

CONTOURS FOR CASE#2

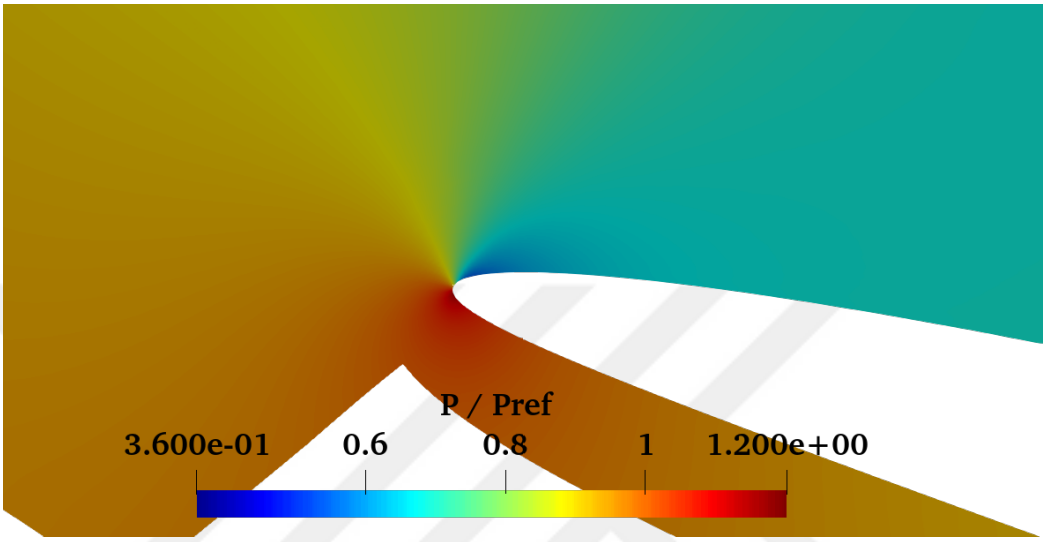

Figure 62: $\frac{P}{P_{ref}}$ Around Impeller Leading Edge for Case#2 at a Lower η

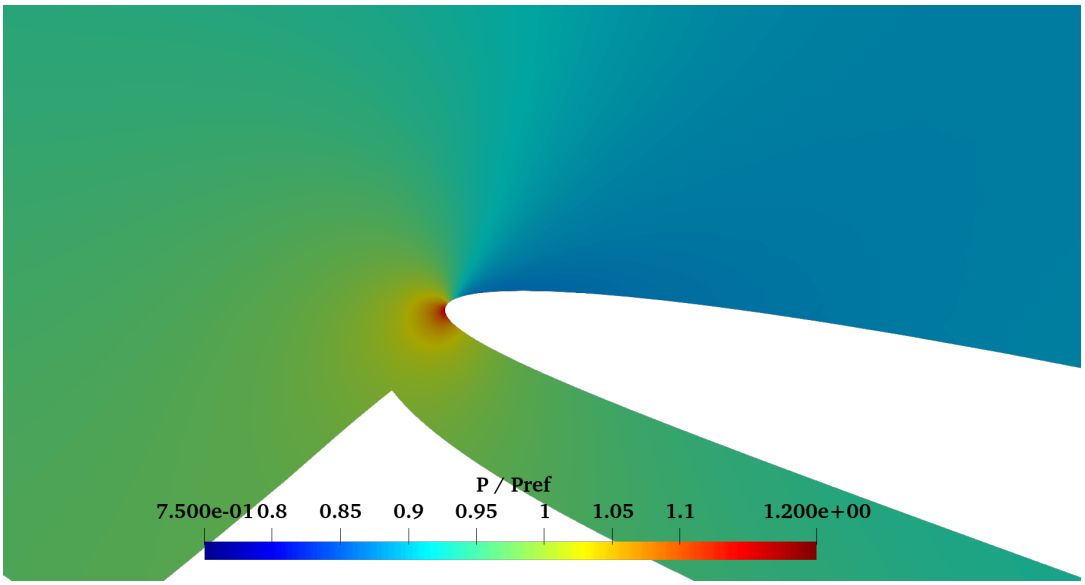

Figure 63: $\frac{P}{P_{ref}}$ Around Impeller Leading Edge for Case#2 at a Higher η

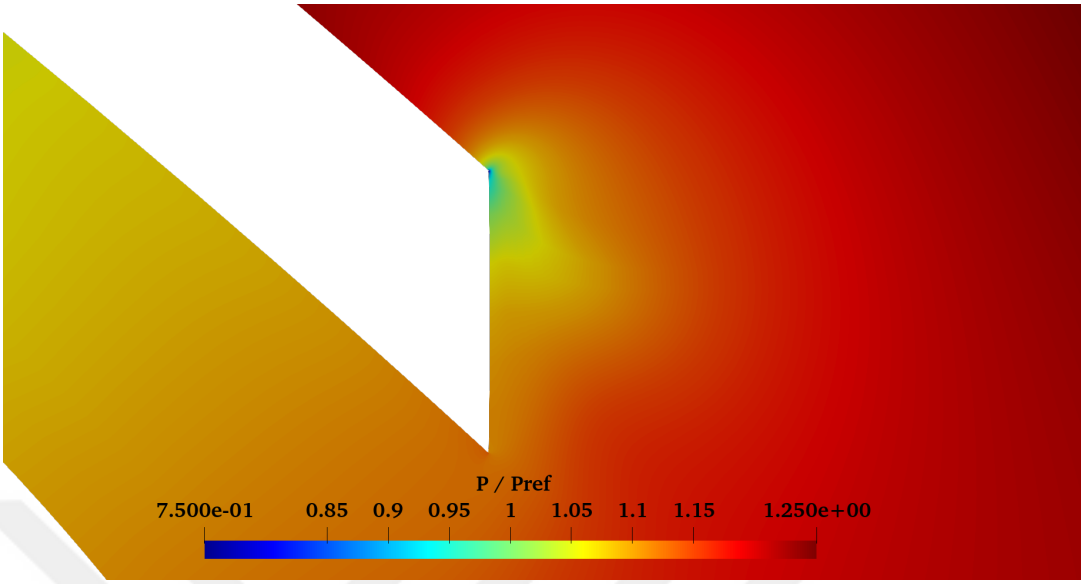

Figure 64: $\frac{P}{P_{ref}}$ Around Impeller Trailing Edge for Case#2 at a Lower η

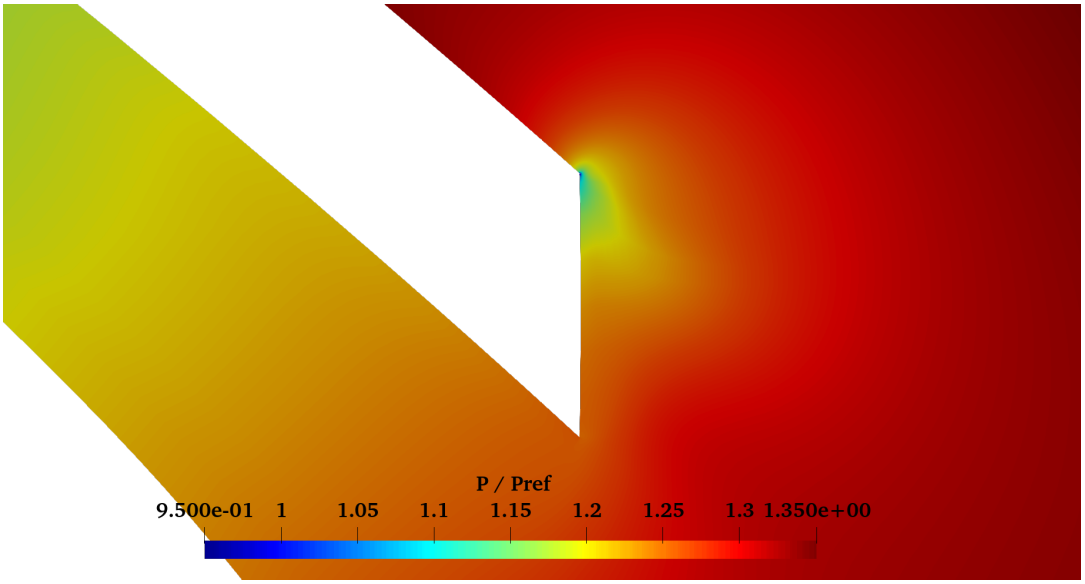

Figure 65: $\frac{P}{P_{ref}}$ Around Impeller Trailing Edge for Case#2 at a Higher η

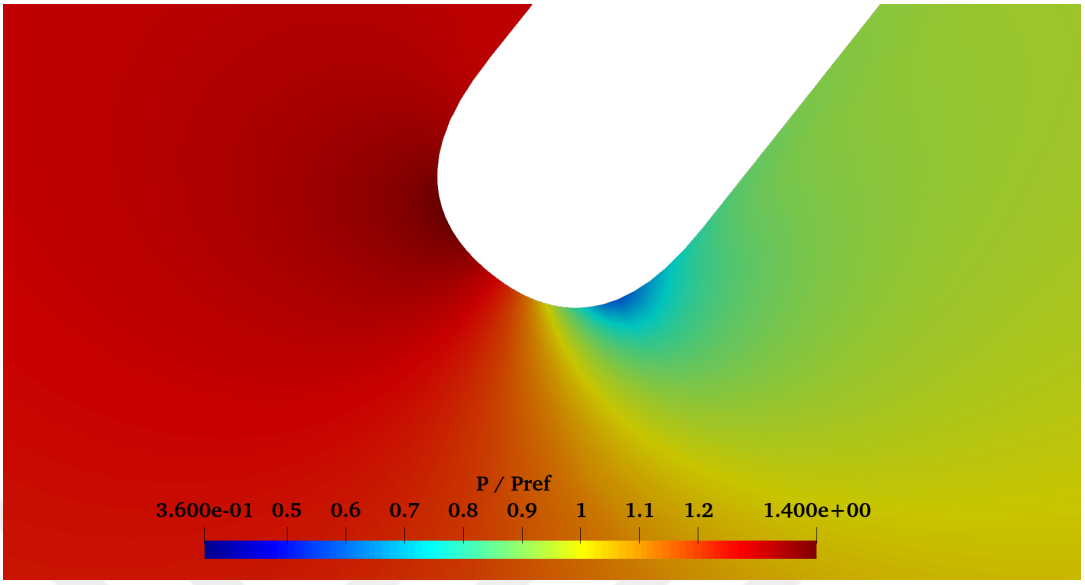

Figure 66: $\frac{P}{P_{ref}}$ Around Diffuser Vane Leading Edge for Case#2 at a Lower η

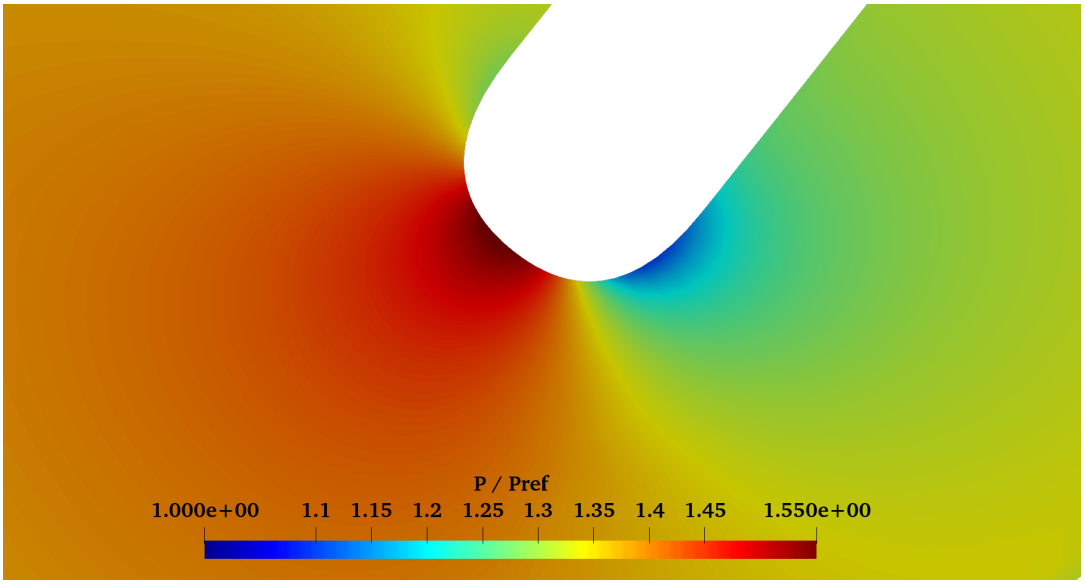

Figure 67: $\frac{P}{P_{ref}}$ Around Diffuser Vane Leading Edge for Case#2 at a Higher η

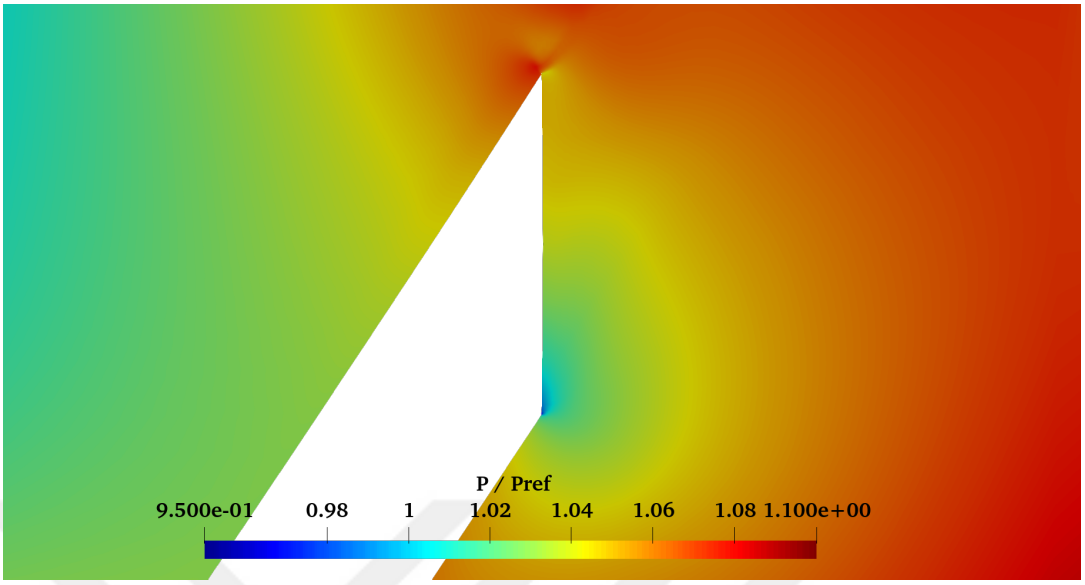

Figure 68: $\frac{P}{P_{ref}}$ Around Diffuser Vane Trailing Edge for Case#2 at a Lower η

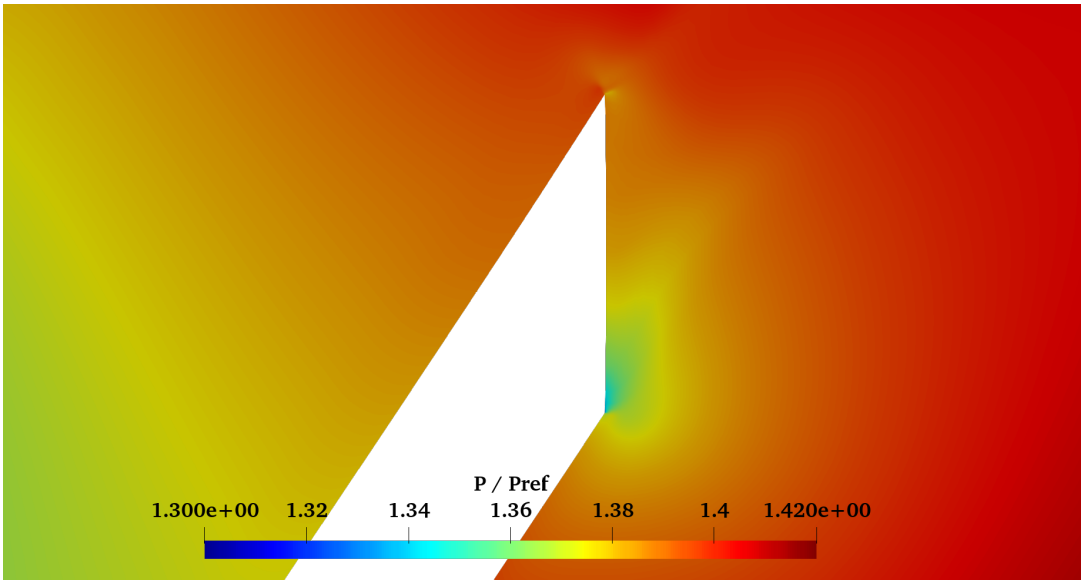

Figure 69: $\frac{P}{P_{ref}}$ Around Diffuser Vane Trailing Edge for Case#2 at a Higher η

REFERENCES

[1] H. K. Versteeg and W. Malalasekara, *An Introduction to Computational Fluid Dynamics*. Glasgow: Pearson Education Limited, 2 ed., 2007.

[2] F. Palacios, M. R. Colonno, A. C. Araneke, A. Campos, S. R. Copeland, T. D. Economon, A. K. Lonkar, T. W. Lukaczyk, T. W. R. Taylor, and J. J. Alonso, "Stanford university unstructured SU^2: An open-source integrated computational environment for multi-physics simulation and design.," *AIAA Aerospace Sciences Meeting including the New Horizons Forum and Aerospace Exposition*, vol. 51, 2013.

[3] I. C. de Castro, "Assessment of su2 for radial compressor performance prediction," Master's thesis, Delft University of Technology, 2019.

[4] V. F. Mollá, "3d-simulation of multi-stage turbomachinery by means of a non-reflecting mixing plane interface," Master's thesis, Delft University of Technology, 2017.

[5] H. J. P. M. Gaens, "Best practices for adjoint-based shape optimization of turbomachinery stages," Master's thesis, Delft University of Technology, 2020.

[6] P. G. de la Serna, "Adjoint-based 3d shape optimization for turbomachinery applications," Master's thesis, Delft University of Technology, 2019.

[7] E. C. Bunschoten, "Turbomachinery analysis and design using body-force modeling in su2," Master's thesis, Delft University of Technology, 2020.

[8] R. C. W. de Koning, "Development of a parametric 3d turbomachinery blade modeler," Master's thesis, Delft University of Technology, 2015.

[9] F. D'amico, "Turbulent round jet cfd analysis with su2 code: from validation to aircraft's exhaust," Master's thesis, Politecnico di Torino, 2019.

[10] B. Yerlikaya, "Adjoint based optimization of supersonic converging diverging nozzle," Master's thesis, Middle East Technical University, 2019.

[11] A. Ahmed, *Adjoint Based Aerodynamic Shape Optimization of Subsonic Submerged Intake*. PhD thesis, Middle East Technical University, 2021.

[12] B. Y. Yıldırım, "Aerodynamic shape optimization of a wing using 3d flow solutions with su2 and response surface methodology," Master's thesis, Middle East Technical University, 2021.

[13] O. Yirtici, K. Cengiz, S. Ozgen, and I. H. Tuncer, "Aerodynamic validation studies on the performance analysis of iced wind turbine blades," *Computers and Fluids*, vol. 192, 2019.

[14] J. E. Hoogervorst and A. Elham, "Wing aerostructural optimization using the individual discipline feasible architecture," *Aerospace Science and Technology*, vol. 65, pp. 90–99, 2017.

[15] R. Sanchez, R. Palacios, T. D. Economon, H. L. Kline, J. J. Alonso, and F. Palacios, "Towards a fluid-structure interaction solver for problems with large deformations within the open-source su2 suite," in *57th AIAA/ASCE/AHS/ASC Structures, Structural Dynamics, and Materials Conference*, January 2016.

[16] A. Kanoria and D. D. Chandar, "Integrating the stanford university unstructured code (su2) with overset grids," in *22nd AIAA Computational Fluid Dynamics Conference*, June 2015.

[17] M. Morelli, T. Bellosta, and A. Guardone, "Development and preliminary assessment of the open-source cfd toolkit su2 for rotorcraft flows," *Journal of Computational and Applied Mathematics*, vol. 389, 2021.

[18] T. Kim, S. Kim, J. Lim, and S. Jee, "Numerical investigation of compressibility effect on dynamic stall," *Aerospace Science and Technology*, vol. 105, 2020.

[19] M. Pini, S. Vitale, P. Colonna, G. Gori, A. Guardone, T. Economon, J. J. Alonso, and F. Palacios, "Su2: the open-source software for non-ideal compressible flows," *Journal of Physics: Conference Series*, vol. 821, 2017.

[20] G. Gori, M. Zocca, G. Cammi, A. Spinelli, and A. Guardone, "Experimental assessment of the open-source su2 cfd suite for orc applications," *Energy Procedia*, vol. 129, pp. 256–263, 2017.

[21] P. Molesini, G. Gori, and A. Guardone, "An analysis of fast-response pressure probes dynamics for orc power systems," *Energy Procedia*, vol. 129, pp. 264–271, 2017.

[22] D. Vimercati, G. Gori, A. Spinelli, and A. Guardone, "Non-ideal effects on the typical trailing edge shock pattern of orc turbine blades," *Energy Procedia*, vol. 129, pp. 1109–1116, 2017.

[23] A. Rubino, S. V. amd Piero Colonna, and M. Pini, "Fully-turbulent adjoint method for the unsteady shape optimization of multi-row turbomachinery," *Aerospace Science and Technology*, vol. 106, 2020.

[24] S. Vitale, M. Pini, and P. Colonna, "Multistage turbomachinery design using the discrete adjoint method within the open-source software su2," *Journal of Propulsion and Power*, vol. 36, no. 3, pp. 465–478, 2020.

[25] N. Anand, S. Vitale, M. Pini, and P. Colonna, "Assessment of ffd and cad-based shape parametrization methods for adjoint-based turbomachinery shape optimization," in *Global Power and Propulsion Montreal 2018*, May 2018.

[26] J. Anderson, *Fundamentals of Aerodynamics*. New York: McGraw-Hill Education, 6 ed., 2017.

[27] L. Davidson, "An introduction to turbulence models." http://www.tfd.chalmers.se/∼lada (accessed June 5,2022), Göteborg, 2018.

[28] K. Hami, "Turbulence modeling a review for different used methods," *International Journal of Heat and Technology*, vol. 39, pp. 227–234, 2021.

[29] P. R. Spalart and S. R. Allmaras, "A one-equation turbulence model for aerodynamic flows," *La Recherche Aérospatiale*, vol. 1, pp. 5–21, 1994.

[30] F. R. Menter, "Two-equation eddy-viscosity turbulence models for engineering applications," *AIAA Journal*, vol. 32, no. 8, pp. 1598–1605, 1994.

[31] L. Davidson, "Fluid mechanics, turbulent flow and turbulence modelling." http://www.tfd.chalmers.se/∼lada (accessed June 5,2022), Göteborg, 2014.

[32] D. C. Wilcox, "Reassessment of the scale-determining equation for advanced turbulence models," *AIAA Journal*, vol. 26, no. 11, pp. 1299–1310, 1988.

[33] F. R. Menter, "Influence of freestream values on $k-\omega$ turbulence model predictions," *AIAA Journal*, vol. 30, no. 6, pp. 1657–1659, 1991.

[34] F. R. Menter, M. Kuntz, and R. Langtry, "Ten years of industrial experience with sst turbulence model," *Turbulence, Heat and Mass Transfer*, vol. 4, 2003.

[35] A. Hellsten, "New advanced $k-\omega$ turbulence model for high-lift aerodynamics," *AIAA Journal*, vol. 43, no. 9, pp. 1857–1869, 2005.

[36] O. Kwon and F. E. Ames, "Advanced $k-\epsilon$ modelling of heat transfer," tech. rep., NASA, July 1995.

[37] T. D. Economon, F. Palacios, S. R. Copeland, T. W. Lukaczyk, and J. J. Alonso, "Su2: An open-source suite for multiphysics simulation and design," *AIAA Journal*, vol. 54, pp. 828–846, March 2016.

[38] A. Jameson, W. Schmidt, and E. Turkel, "Numerical solution of the euler equations by finite volume methods using runge-kutta time stepping schemes," in *14th Fluid and Plasma Dynamics Conference*, June 1981.

[39] P. L. Roe, "Approximate riemann solvers, parameter vectors, and difference schemes," *Journal of Computational Physics*, vol. 43, no. 2, 1981.

[40] M.-S. Liou and C. J. S. Jr., "A new flux splitting scheme," *Journal of Computational Physics*, vol. 107, no. 1, pp. 23–29, 1993.

[41] E. F. Toro, *The HLL and HLLC Riemann Solvers*, pp. 315–344. Berlin, Heidelberg: Springer Berlin Heidelberg, 3 ed., 2009.

[42] B. van Leer, "Muscl, a new approach to numerical gas dynamics," in *2nd European Conference on Computational Physics*, January 1976.

[43] V. Venkatakrishnan, "On the accuracy of limiters and convergence to steady state solutions," in *31st Aerospace Sciences Meeting*, January 1993.

[44] G. D. van Albada, B. van Leer, and W. W. Roberts, *A Comperative Study of Computational Methods in Cosmic Gas Dynamics*, pp. 95–103. Berlin, Heidelberg: Springer Berlin Heidelberg, 1997.

[45] T. Barth and D. Jespersen, "The design and application of upwind schemes on unstructured meshes," in *27th Aerospace Sciences Meeting*, January 1989.

[46] Y. Saad and M. H. Schultz, "Gmres: A generalized minimal residual algorithm for solving nonsymmetric linear systems," *SIAM Journal on Scientific and Statistical Computing*, vol. 7, no. 3, pp. 856–869, 1986.

[47] Y. Saad, "A flexible inner-outer preconditioned gmres algorithm," *SIAM Journal on Scientific and Statistical Computing*, vol. 14, no. 2, pp. 451–469, 1993.

[48] H. A. van der Vorst, "Bi-cgstab: A fast and smoothly converging variant of bi-cg for the solution of nonsymmetric linear systems," *SIAM Journal on Scientific and Statistical Computing*, vol. 13, no. 2, pp. 631–644, 1992.

[49] S. Yoon and A. Jameson, "Lower-upper symmetric-gauss-seidel method for the euler and navier-stokes equations," *AIAA Journal*, vol. 26, no. 9, pp. 1025–1026, 1988.

[50] M. B. Giles, "Non-reflecting boundary conditions for euler equation calculations," *AIAA Journal*, vol. 28, no. 12, 1990.

[51] M. B. Giles, P. Moinier, and J. Coupland, "Three-dimensional nonreflecting boundary conditions for swirling flow in turbomachinery," *Journal of Propulsion and Power*, vol. 23, no. 5, 2007.

[52] R. Courant, K. Friedrichs, and H. Lewy, "On the partial difference equations of mathematical physics," *IBM Journal of Research and Development*, vol. 11, no. 2, pp. 215–234, 1967.

[53] M. B. Giles and N. A. Pierce, "An introduction to the adjoint approach to design," *Flow, Turbulence and Combustion*, vol. 65, pp. 393–415, 2000.

[54] G. D. Ntanakas and M. Meyer, "Towards unsteady adjoint analysis for turbomachinery applications," in *European Conference on Computational Fluid Dynamics (ECFD VI)*, 2014.

[55] R. M. Hicks and P. A. Henne, "Wing design by numerical optimization," *Journal of Aircraft*, vol. 15, no. 7, 1978.

[56] A. Koshakji, A. Quarteroni, and G. Rozza, "Free form deformation techniques applied to 3d shape optimization problems," tech. rep., Mathematics Institute of Computational Science and Engineering - École Polytechnique Fédérale de Lausanne, December 2013.

[57] T. Sederberg and S. Parry, "Free-form deformation of solid geometric models," in *ACM Siggraph Computer Graphics*, vol. 20, pp. 151–160, August 1986.

VITA

MUSTAFA KÜRŞAT UZUNER

Ankara/Türkiye

SUMMARY

I am an Aerodynamics Engineer and working at Turkish Aerospace Industries Inc. (TAI) at the moment, mostly working on CFD analysis of various aircraft components. I have completed my Mechanical Engineering MSc degree at Özyeğin University, specializing in CFD applications on centrifugal turbomachinery. During my BSc degree at İstanbul Technical University, I have been involved in projects and internships with a couple aerospace companies in Turkey, namely TEI and TAI. I have done my masters on the open-source simulation tool SU2. Also, I have experience in StarCCM+, ANSYS CFX and Icem-CFD for simulations and meshing. I have worked with Python, C, Fortran, MATLAB etc. during my education and have been using these tools still in work from time to time. I aim to work on CFD applications of anything that moves through air or moves air through itself. I like aerodynamics.

EDUCATION

Özyeğin University - İstanbul/Türkiye 2019-2023

Mechanical Engineering, MSc

GPA: 3.96/4

İstanbul Technical University - İstanbul/Türkiye 2014-2019

Aeronautical Engineering, BSc

GPA: 3.76/4

PROJECTS

Preliminary Investigation of SU2 for Compressible Flows September 2020 - June 2021

MAN-Energy Solutions and Özyeğin University Özyeğin University

Adjoint Project

The investigation aims at evaluating SU2 as a possible 3D CFD tool for large scale computational campaigns in multi parameter, high fidelity modeling optimization studies for centrifugal compressor component (impellers, diffusers and return channels) development.

Droplet Accretion with Euler Equations June 2019

Aeronautical Engineering Graduation Project İstanbul Technical University

Supercooled water particles movement in a parallel channel with a fully developed airflow inside is simulated using Euler equations. The places where these particles would collide mostly are determined. Alternating direction implicit (ADI) method is applied with upwind scheme. The airflow inside the channel is calculated once and assumed to be same and kept unchanged during calculations. Fortran is used for calculations.

EXPERIENCE

Turkish Aerospace Industries Inc. April 2021 - Present

Position: Aerodynamics Engineer *Ankara/Türkiye*

- Geometry cleaning and repairing using Simens NX and StarCCM+ for CFD analysis preparation.
- Experimental results verification and comparison with CFD for different intake designs.
- Wind tunnel CFD modelling for preliminary requirements of necessary equipment.
- Benchmarking using open source CFD software SU2.
- Development of CFD methodologies for various cases such as determination of dynamic derivatives of an aircraft.
- Development of MATLAB and Python applications for post-processing and pre-processing of any CFD analysis.

Özyeğin University October 2019 - April 2021

Position: Teaching Assistant *İstanbul/Türkiye*

- Teaching assistant of ME111 Computer Aided Technical Drawing course and Physics Labs.

- Proctoring duties of various Math courses.

Turkish Aerospace Industries Inc. December 2018 - May 2019

Position: Internship Trainee *İstanbul/Türkiye*

- CATIA, Nastran-Patran and MATLAB applications are exercised under Intern Engineer Programme (SMP).

Turkish Aerospace Industries Inc. July 2017 - October 2017

Position: Internship Trainee *İstanbul/Türkiye*

- Necessary requirements of propulsion system of a VLA type aircraft are studied. Regarding this requirements, adequate candidate engines are selected. Most suitable engine is chosen via comparison. Propulsion system architecture of the selected engine is formed.

- Candidate propellers are determined, and comparisons of candidates are done. Propeller that can supply the best performance is chosen among the candidates.

TUSAS Engine Industries Inc. July 2017 - August 2017

Position: Intern *Eskişehir/Türkiye*

- Researches about turbochargers are done. The tip clearance and rotor dynamics of a turbocharger are studied in regards of their effect on the performance.

Ak Ziraat Aletleri July 2016 - August 2016

Position: Intern *İzmir/Türkiye*

- Welding, cold working, leveling.

- Observations and studies have been done regarding to forming machine parts, welding, and assembly process.